Koninklijk Nederlands
Meteorologisch Instituut
Ministerie van Infrastructuur en Waterstaat

Utrecht University

Master thesis

Validation of Aeolus satellite wind observations with aircraft-derived wind data and the ECMWF NWP model for an enhanced understanding of atmospheric dynamics

Author

S. Albertema, BEng

to obtain the degree of

Master of Science (MSc)

Utrecht, 2019

Student number:	6308791
Faculty, department:	Faculty of Science, Dept. of Physics
Institute:	Institute for Marine and Atmospheric research Utrecht (IMAU)
Supervisors:	dr.ir. G.J. Marseille (KNMI) dr. A.J. van Delden (IMAU)
Second corrector:	dr. W.J. van de Berg (IMAU)
Version Nr.:	2019v02

"Sol Iustitiae Illustra Nos"
— Utrecht University [Est. 1636]

Abstract

Launched on August 22^{th} of 2018 —the Atmospheric Dynamics Mission - Aeolus of the European Space Agency (ESA) carries a direct detection Doppler Wind Lidar to measure wind profiles in the atmosphere from space. The primary product of this Earth observation satellite is the measurement of profiles of the horizontally projected line-of-sight (HLOS) wind component, resulting into a single wind component measurement rather than the complete wind vector. The main motivation of the Aeolus mission is to reduce the deficiency in the current global coverage of wind observations, as part of the current Global Observing System (GOS) of the World Meteorological Organization (WMO) [World Meteorological Organization (WMO), 2013]. Aeolus is a next step in the aim for a homogeneous spatial and temporal global network of wind observations. In this study, HLOS wind observations of Aeolus have been validated with independent and high-resolution aircraft-derived Mode-S EHS wind observations, together with the Numerical Weather Prediction (NWP) model of the European Centre for Medium-Range Weather Forecasts (ECMWF). Validation is a challenge for a unique instrument —never flown before —which is still in its commissioning phase, meaning that observed winds have not yet been well-calibrated, hence not yet suitable for operational use in NWP. Nevertheless, the main validation results are very promising demonstrating a high agreement between Aeolus, Mode-S EHS and ECMWF with correlation values exceeding 0.9. The known systematic, and slowly drifting over time, bias in the order of 2 ms^{-1} is observed and confirmed from standard statistics as well as from the more advanced triple collocation technique.

Index terms— Atmospheric Dynamics Mission, Aeolus, Earth observation satellite, Doppler Wind Lidar, Mode-S EHS, validation

Figure 1: **Wind God Aeolus brings Odysseus a misfortune**. According to the works of the Greek poet Homer (∼800 - 750 B.C.), Aeolus was appointed to be the *Keeper of the Winds*, *casu quo* controller of the wind and ruler of the floating island *Aeolia* —nowadays known as the *Aeolian Islands* in the Tyrrhenian Sea. Homer described in his work *the Odyssey* (∼800 B.C.) that Aeolus gave Odysseus a tightly closed bag including the winds to sail home from the Trojan War on the West Wind back Ithaca. The companions of Odysseus opened the bag nevertheless too early and the wind —which turned out to be a headwind —escaped the bag. A misfortune for Odysseus and his companions since they float back with their ship to the Aeolia island. *Source: iStockphoto.*

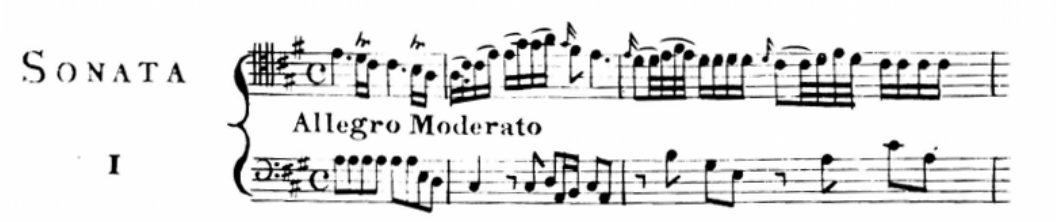

Prologue & Acknowledgment

August 22^{nd} of 2018, performing my summer job responsibilities while my mind is reflecting in the background on the successful accomplishment of finishing the previous academic year at the university. In addition, thinking about interesting topics for my upcoming challenge in the next academic year: writing my graduation thesis.

"Steven, 10 minutes break for you!", yells my colleague. While taking that well deserved break after grabbing a cup of coffee, it was time to observe the atmosphere and the clouds. A frequent activity for me. The contrast in terms of composition and the dynamic variability fascinates me unconditionally. It is like watching a *Rembrandt* varying on the spot. While still thinking about a graduation topic and scanning the news of the day in the mean time, this thought process came to an immediate end when reading the header *"ESA launches satellite to enhance weather predictions"* (..) in collaboration with the Royal Netherlands Meteorological Institute (KNMI). This was the launch for me to contact the KNMI concerning a graduation topic about this novel Earth observation satellite mission of ESA —The *Atmospheric Dynamics Mission - Aeolus*.

- **KNMI:** First of all, I am dr.ir. Gert-Jan Marseille extraordinary grateful for the invitation to visit the KNMI —after sending him an e-mail concerning my interest —to discuss the possible graduation topic related to the Aeolus. This discussion was together with dr.ir. Ad Stoffelen and dr.Jos de Kloe, both involved in the same satellite mission. The collaboration between mr. Marseille and me during the graduation research phase of about eight months was professional and at the same time convenient and pleasant. The same applies to mr. Stoffelen and mr. de Kloe, with each their own expertise. This spectrum of expertise gave rise to put my question —depending on the type of my question —to either mr. Marseille, mr. Stoffelen or mr. de Kloe. I am very grateful for their contribution in terms of constructive comments and discussions.

  Furthermore, I am very grateful to mr. Marseille, mr. Stoffelen and mr. de Kloe for involving[1] me in the aforementioned satellite mission and the corresponding calibration and validation team of ESA and its partners. It was an honour to gather experience working in such a team of scientists and engineers. Working with big satellite data comes together with frustrations in terms of e.g. file formatting, memory issues, computational timing and interpretation. Especially working with raw data due to the 'lack' of a profound understanding of what is

[1] E.g. inviting me to ESA telecommunication conferences discussing latest news and results, presenting some of my validation results during the *Calibration and Validation Workshop - March 2019* at ESRIN in Rome (Italy) and involving me in what is discussed, or discussing my research results with other researchers during e.g. the *ESA Living Planet Symposium - May 2019* in Milan (Italy).

happening in the data set —which therefore requires *a priori* proper validation and calibration studies. Despite these frustrations, it was a great scientific research experience to work with these novel meteorological representative satellite data.

My acknowledgement also go to dr. Olaf Tuinder, dr. Tim Vlemmix and Mirjam den Hoed (MSc) for their constructive feedback, tips and daily support. Since mrs. den Hoed and mr. Vlemmix guide intern and graduation students, next to their daily scientific research activities, they understood my issues and uncertainties concerning my graduation phase very well.

- **University:** My acknowledgements are going to dr. Aarnout van Delden and dr. Willem Jan van de Berg for being my supervisor and second supervisor respectively from the point of view of Utrecht University and the Institute for Marine and Atmospheric research Utrecht (IMAU). I highly appreciate their contribution in terms of constructive feedback and discussions.
- **Family:** From the point of view of the family, I want to stress my acknowledgement to my parents and sister as well for supporting me unconditionally during my studies. Some of the weekends I returned home to my parents. When home, they received a private lecture about my graduation phase. Thank you for listening to these never ending stories. This is just the result of when something is fascinating and interesting —ESA its novel Earth observation satellite *Aeolus*.

"Stand in absolute awe of the (geo)physics of the nature and embrace its beauty".

Steven Albertema, July 2019.

Contents

1 Introduction

Together with physical quantities as air temperature, atmospheric pressure and humidity —wind is one the basic quantities describing the physical state of the atmosphere. Differential heating between equatorial regions and the poles results in expansion and contraction of air mass and gives rise to pressure gradients in the atmosphere. Wind is the result of these pressure gradients due to the advection of air mass from high to low pressure systems and basically redistributes thermal energy. The process of thermal energy redistribution —combined with the rotation of the Earth —generates large scale atmospheric dynamics which influences weather systems and the climate.

Numerical Weather Predictions (NWP) includes the assimilation of atmospheric wind observations, but the quality of these forecast predictions is critically dependent on the quality and quantity of these wind observations [see e.g. Marseille and Stoffelen, 2003]. The quality of NWP is essential for scientists and meteorologists to understand large scale atmospheric dynamics and therefore weather systems and the climate. Wind observations are one of the most fundamental —and also lacking —meteorological quantities in the current Global Observing System (GOS). The World Meteorological Organization (WMO) depicted the deficiency in a homogeneous spatial and temporal global coverage of wind observations in the current GOS, especially above the oceans, southern hemisphere and near the equatorial regions [World Meteorological Organization (WMO), 2013]. Wind profile measurements with the novel Doppler lidar technique from space —performed by the recently in August 2018 launched Earth observation satellite *Aeolus* of the European Space Agency (ESA) —will complement for the deficiency of wind observations in the current GOS by providing a more homogeneous spatial and temporal coverage of wind observations on a global scale.

Observing systems in the current GOS includes meteorological and oceanographic data buoys, radiosondes, weather radars and observation satellites. Also aircraft contribute to the GOS since they are able to broadcast valuable meteorological representative information such as outside air temperature, wind speed, wind direction, and atmospheric pressure. These aircraft observational data —together with NWP data from the European Centre for Medium-Range Weather Forecasts (ECMWF) —will be used in this research thesis to validate the wind observations as measured by Aeolus.

1.1 Research motivation

The motivation to perform this research is to validate the quality of the raw measured wind observations as measured by the novel Aeolus satellite of ESA. The aircraft-derived wind observations —hereafter referred to as *Mode-S EHS*[2] aircraft-derived wind observations —are used as the primary reference due to its high temporal and spatial resolution which in turn results into a higher statistical significance.

Additional meteorological information from the ECMWF Integrated Forecast System (IFS) are *a priori* required for the Aeolus product processors to correct the wind observations for temperature and pressure effects. This provided the opportunity to retrieve the wind velocity components from the ECMWF IFS model as well as an additional independent

[2]More information will be provided in Sec. [4]

reference data set.

The validation research is performed in collaboration with the Royal Dutch Meteorological Institute (KNMI).

1.2 Research questions

The main research question is trivial:

What is the quality of the wind observations as measured by ESA its novel Earth observation satellite Aeolus when compared with Mode-S EHS aircraft-derived wind observations?

Albeit during the research phase new insight arise which in turn results into new sub-research questions —the main sub-questions to elaborate on the main research question are:

- How does the current observing network of meteorological representative observations look like in terms of wind observations?
- Why are wind observations required *casu quo* what is the scientific motivation and purpose of the introduction of Aeolus?
- What is the spatial and temporal resolution of the wind observations of Aeolus?
- How is the wind measured by the satellite? Is direct use for e.g. validation research possible?
- What is the spatial and temporal resolution of the Mode-S EHS aircraft-derived wind observations?

1.3 Thesis structure

This graduation thesis will elaborate on the theoretical background of the Aeolus mission in detail and on Mode-S EHS, to a lesser extent [Sec. 2 - 4]. A comprehensive theoretical background is provided at first since a profound literature study was *a priori* required in order to understand the necessary concept of the mission, the wind retrieval principle and the raw data. After a profound literature study, the thesis will elaborate extensively on the performed validation research [Sec. 5 - 9]. The research thesis is divided into the following sections:

Sec. [2] - **The Atmospheric Dynamics Mission - Aeolus** elaborates on the scientific motivation and purpose in more detail and the need of enhanced wind observations in the current observing system of meteorological representative observations.

Sec. [3] - **Aeolus satellite-derived meteorological data** focuses on the orbit geometry of the satellite and the wind retrieval principles. Aeolus is the first satellite using an ultra-violet laser to measure the wind from space. The measurement principle of Aeolus is complex and requires *a priori* a profound literature study in order to understand the data set. It also discusses the delivered products of Aeolus and which of these are used for this

validation research.

Sec. [4] - **Mode-S EHS aircraft-derived meteorological data** briefly describes the spatially and temporally high-resolution aircraft-derived Mode-S EHS wind observations. This data set is used as the primary reference for Aeolus during the validation research.

Sec. [5] - **Preprocessing and collocating the data** discusses how the data sets of Aeolus, Mode-S EHS and ECMWF IFS are being preprocessed. Preprocessing the data sets is necessary in order to *collocate* the data sets, i.e. merge the three independent data sets to approximately the same *geolocation* —date, time and space. After preprocessing the data sets, the data can be collocated.

Sec. [6] - **Validation results** discusses the validation results after collocation of the three independent data sets. This section also outlines model optimization steps to increase the accuracy of the collocation algorithms.

Sec. [7] - **Discussion** will shortly discuss on discrepancies and some notes regarding the performed validation methodology and the corresponding results.

Sec. [8] - **Conclusion** concludes the validation research by providing the main validation results and by reflecting on the main research question.

Sec. [9] - **Epilogue** provides context concerning to the performed research and the corresponding results.

2 The Atmospheric Dynamics Mission - Aeolus

The scientific background and motivation of Aeolus will be discussed initially [Sec. 2.1], before elaborating on the deficiencies in the current global observing system of meteorological representative data [Sec. 2.2]. To complement to the latter, the need of wind measurements will be discussed in detail [Sec. 2.3].

2.1 Scientific background and motivation

Established in 1995 —the *Living Planet Programme* of the European Space Agency (ESA) outlines Earth observation missions and comprises two main missions [European Space Agency (ESA), 2006]:

- *Earth Explorer missions*, which have a scientific research focus on an improvement of the understanding of the Earth system —the atmosphere, biosphere, cryosphere, hydrosphere, geosphere, and their interactions.
- *Earth Watch missions*, which is operational service driven by facilitating Earth observation data for operational meteorological purposes under control of the European Organisation for the Exploitation of Meteorological Satellites (EUMETSAT).

2.1.1 Scientific objectives

Launched on August the 22^{th} of 2018 —Aeolus is the fifth Earth Explorer mission of the *Living Planet Programme* of ESA. The primary scientific objective is to acquire profiles of the horizontal wind component from the troposphere and lower stratosphere on a global scale, which gives rises to an enhanced understanding of atmospheric dynamics and an improvement in weather forecasting when being assimilated in a NWP model [Stoffelen et al., 2005]. Additionally, the main objective is to complement for the major deficiency in the spatial and temporal global coverage of wind observations in the current GOS, especially in regions above the oceans, southern hemisphere and in the equatorial regions [World Meteorological Organization (WMO), 2013].

2.1.2 Scientific benefits

Next to an enhanced understanding of atmospheric dynamics and an improvement in weather forecasting —scientific benefits from the aforementioned objectives of Aeolus are e.g. better parametrisation of atmospheric processes in numerical models for atmospheric flow modelling, an increase in the accuracy of initial conditions for numerical models, or other climate related research such as an enhanced understanding of tropical winds which influences the occurrence of e.g. *El Niño-Southern Oscillation*[3].

[3] A large scale ocean-atmosphere interaction climate cycle in the East-central Equatorial Pacific Ocean in which fluctuations in sea surface temperatures and atmospheric temperatures results into so-called periodic *warm phases* (i.e. El Niño phase) and *cold phases* (i.e. La Niña phase) of sea surface temperatures. More information, see e.g. `https://oceanservice.noaa.gov/facts/ninonina.html`.

2.2 Deficiencies in current GOS

Meteorological, oceanographic and other geophysical observations are essential to understand the Earth system —the atmosphere, biosphere, cryosphere, hydrosphere, geosphere, and their interactions which influences e.g. weather systems and the climate. The WMO coordinates the GOS containing these geophysical observations and facilitates the establishment, maintenance and continuation of this global observation network.

The current GOS of the WMO receives wind observations from several *in situ* or remote-sensing observing systems such as ocean data buys, radiosondes attached to weather balloons, weather radars, wind profilers, Doppler radars or with e.g. the *Atmospheric Motion Vectors*[4] observation technique [Fig. 2a]. Aircraft observations also contribute to the GOS since they broadcast valuable meteorological representative data [Fig. 2b]. According to e.g. Graham et al. [2006], these kind of data are currently the most important data source for wind observations over for example the Atlantic Ocean.

[4] Atmospheric Motion Vectors is an observation technique in which consecutive satellite images from e.g. clouds or aerosols are taken in order to determine their atmospheric motions and ultimately derive the wind direction and speed.

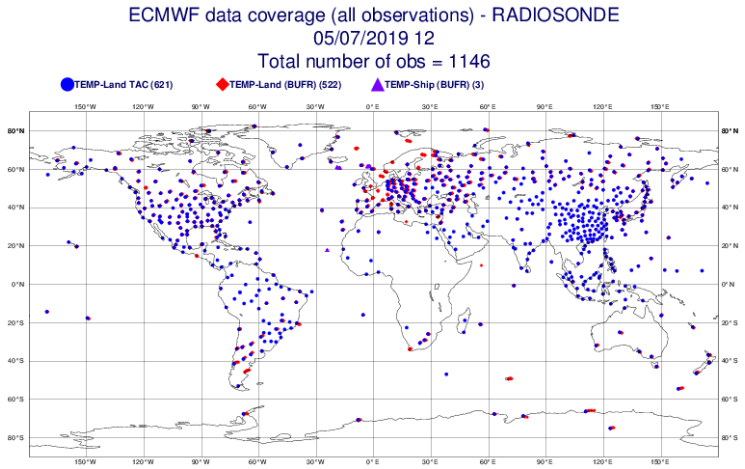

(a)

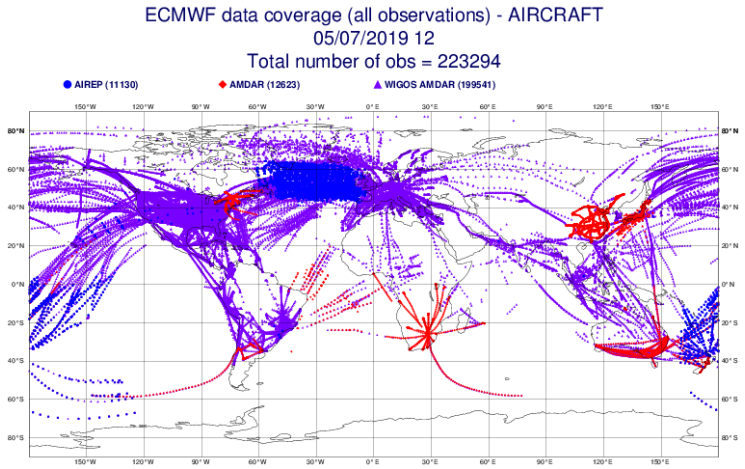

(b)

Figure 2: Geographical coverage of wind observations in the GOS of the WMO retrieved by (a) radiosondes and (b) aircraft. *Source:* ECMWF.

The WMO outlined a major deficiency in a homogeneous spatial and temporal global coverage of wind observations in the current GOS, especially above oceanic regions, in the tropics and regions at the southern hemisphere [see e.g. World Meteorological Organization (WMO), 2013]. This results in serious difficulties in the study of the coupled climate system and in enhancing the quantity and quality of NWP models, since climate modeling is closely related to these numerical models [Stoffelen et al., 2005]. Hence, sophistication of spatial and temporal global wind observation coverage and its assimilation in NWP models is required.

Although sophistication of data assimilation methods in NWP is ongoing, large uncertainties in the wind field in the oceanic regions, the tropics and southern hemisphere remain [see e.g. Courtier et al., 2006]. Several reanalysis studies of uncertainties in the initial

conditions in the wind speed above these regions have been performed by e.g. Langland and Maue [2012]. These reanalysis studies show large NWP uncertainties —expressed as the *root mean squared error* (RMSE)[5] —in the wind field in the aforementioned regions [Fig. 3].

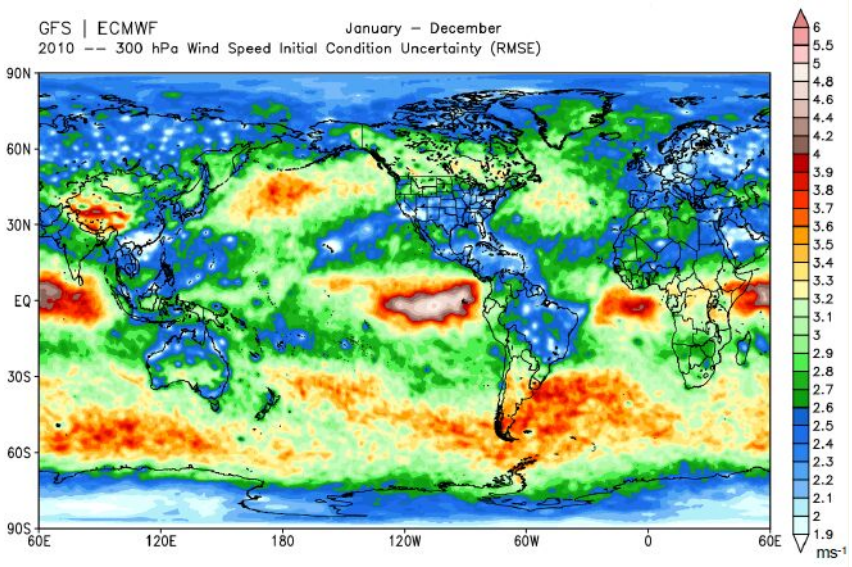

Figure 3: Geographical illustration showing large deviations —expressed as the RMSE —for winds at 300 hPa as simulated by the US Global Forecast System (GFS) and ECMWF. *Source:* Langland and Maue [2012].

Many simulation experiments have been conducted by Marseille et al. [2006] to determine the added value of simulated Aeolus wind observations. These simulation experiments are used to assimilate a prospective observing system such as Aeolus wind observations —on top of simulated wind observations of the current GOS —in a pseudo true atmospheric state to simulate its impact [Marseille et al., 2006]. These experiments demonstrated positive impacts of Aeolus wind observations in the operational ECMWF system, especially above regions which lack of direct wind measurements —oceans, tropics and southern hemisphere [Fig. 4]. Moreover, these experiments demonstrated that the impact increases with altitude as well. This result demonstrates the need of wind observations along a profile in the vertical —i.e. wind profile measurements —rather than observations at a single level.

[5]RMSE is a nomenclature of a frequently used statistical metric in data analysis. It describes the deviation of a certain data set with respect to a predefined reference data set.

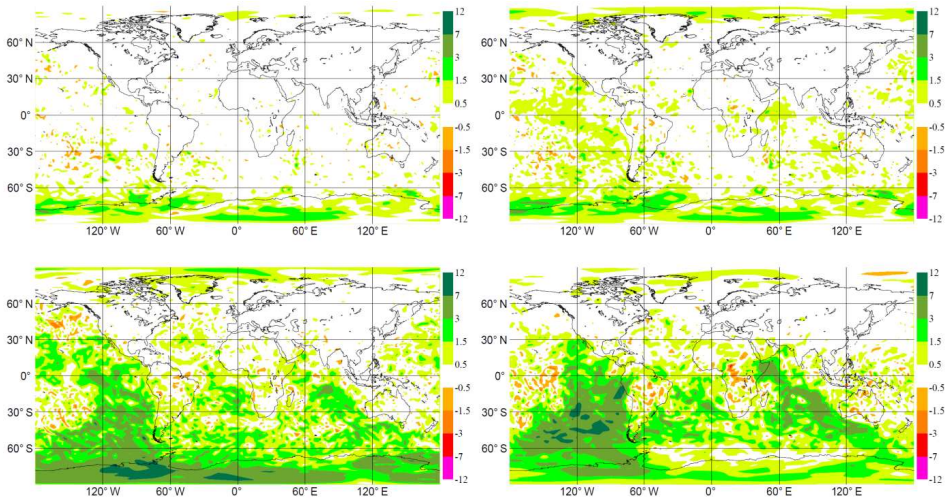

Figure 4: Mean global impact of simulated Aeolus wind observations at (upper left) 1000 hPa, (upper right) 850 hPa, (lower left) 500 hPa, and (lower right) 200 hPa. Impact is expressed as the RMSE [ms^{-1}] between simulation experiments with and without the assimilation of simulated Aeolus wind observations. Red areas denote a negative impact, green areas a positive impact, while white areas are neutral and therefore negligible. *Source:* Marseille et al. [2006].

2.3 The need of wind measurements

Several impact studies with simulated Aeolus wind observations are performed by Marseille et al. [2006] and demonstrated the need of direct wind measurements when being assimilated in a NWP. When direct wind measurements are not possible, indirect methods are required. Although large-scale wind field information can be obtained indirectly with the *geostrophic adjustment theory* [Sec. 2.3.1], this theory is limited to a certain extent. Direct wind measurements are also essential to study the initialization and evolution of large-scale dynamic atmospheric structures, which will be discussed with the concept of *potential vorticity* [Sec. 2.3.2].

2.3.1 Geostrophic adjustment theory

Homogeneous spatial and temporal wind observations above e.g. oceanic regions are sparse while —according to Stoffelen et al. [2005] —upper-wind analysis is mainly dependent on spaceborne observations such as satellite observations. Large-scale wind field information is indirectly obtained when these spaceborne observations are combined with accurate information about the surface pressure and applying the *geostrophic adjustment theory* [Stoffelen et al., 2005]. To elaborate on this geophysical fluid dynamics theory and to justify that wind field information can be obtained by this theory, the physical background of this theory will be discussed.

Assume an arbitrary wind velocity vector:

$$\mathbf{u} := u\mathbf{i} + v\mathbf{j} + w\mathbf{k} \tag{1}$$

with u, v and w being the state-variables for the zonal, meridional and vertical wind velocity

component respectively, and **i**, **j** and **k** the unit vectors in the x, y and z direction respectively. The *momentum equation*[6] can then be written as [see e.g. Holton, 2012]:

$$\frac{D\mathbf{u}}{Dt} = -2\boldsymbol{\Omega} \times \mathbf{u} - \frac{1}{\rho}\nabla p + \mathbf{g} + \mathbf{F}_{fric} \tag{2}$$

where the term on the left-hand side of the momentum equations [Eq. 2] is referred to as the *total time derivative* —or also known as the *material derivative*[7] —and represents the rate of change of the velocity vector while the fluid motion is in a *Lagrangian reference frame*[8]:

$$\frac{D}{Dt} := \frac{\partial}{\partial t} + u\frac{\partial}{\partial x}\mathbf{i} + v\frac{\partial}{\partial y}\mathbf{j} + w\frac{\partial}{\partial z}\mathbf{k} \equiv \frac{\partial}{\partial t} + \mathbf{u} \cdot \nabla \tag{3}$$

where

$$\nabla \equiv \frac{\partial}{\partial x}\mathbf{i} + \frac{\partial}{\partial y}\mathbf{j} + \frac{\partial}{\partial z}\mathbf{k} \tag{4}$$

is defined as the *nabla vector operator*, and $\nabla \cdot \mathbf{u}$ as the divergence of the fluid. The first term of the total time derivative of [Eq. 3] is the *local time derivative* of the velocity vector, while the remaining terms are together the *advection* of the fluid velocity.

The first term on the right-hand side of the momentum equation is the *Coriolis*[9] term where Ω is the rotation of the Earth ($\sim$7.292E^{-5} s^{-1}). Without formal derivations [see e.g. Cushman-Roisin and Beckers, 2011], this term commonly reduces to:

$$f = 2\Omega \sin\phi \tag{5}$$

and is designated as the *Coriolis parameter*[10] with ϕ being the latitude of the fluid. The second term on the right hand side of the momentum equation is the *pressure gradient*. Taking into account the gravity of the Earth is encountered in the third term, while the last term represents any additional forces such as friction[11].

[6] When the Coriolis-term (first term on the right hand side of Eq. 2 is neglected and the friction term (last term on the right hand side of Eq. 2) only represents molecular friction, the momentum equations are reduced to the famous fluid dynamics *Navier-Stokes equations*, named after the French physicist Claude-Louis Navier (1785 - 1836) and the Irish mathematician and physicist George Stokes (1819 - 1903). In geophysical fluid dynamics, geophysical flows obey in general the generalizations of the Navier-Stokes equations.

[7] The total time derivative —or material derivative —is also sometimes referred to as the *Lagrangian derivative*, named after the Italian mathematician and astronomer Joseph-Louis Lagrange (1736 - 1813). The Lagrangian derivative assumes that a control volume —consisting of infinitesimal mass of fluid particles —moves in the Lagrangian frame of reference in which a control volume moves with the local fluid velocity.

[8] See previous footnote.

[9] Named after Gaspard Gustave de Coriolis (1792 - 1843) —a french engineer fascinated by problems related to equations of motions in a rotating framework of reference.

[10] The Coriolis parameter f is approximated by a Taylor expansion: $f = f_0 + \beta y + \textit{higher-order-terms}$, where $f_0 = 2\Omega \sin\phi$, while the βy-term describes how f varies in the meridional direction from a certain initial latitude ϕ_0. When the Taylor approximation is truncated after the first term, the Coriolis parameter is approximated by $f \approx f_0$ and referred to as the *f-plane* approximation. Alternatively, the *beta-plane approximation* is a first-order Taylor approximation of f, that is: $f \approx f_0 + \beta y$. For formal derivations see e.g. Cushman-Roisin and Beckers [2011].

[11] The friction term is usually expressed as $\mathbf{F}_{fric} = -\nu\nabla^2\mathbf{u}$, where ν is the *Eddy viscosity* with ∇^2 being the two-dimensional *Laplace operator*, i.e. the first derivative of the nabla vector operator ∇. In the study of turbulence in fluids, the Eddy viscosity characterizes the transport and dissipation of energy , i.e. *energy cascade*, in the smaller scale flow such as in the planetary boundary layer.

The ratio between the advection to the Coriolis force in the momentum equation is designated as the *Rossby number*[12] R_O, and the ratio between the local time derivative of the velocity to the Coriolis force is designated as the *temporal Rossby number*, R_{O_T}. Assuming a geophysical fluid to be a homogeneous flow in which the background rotation —i.e. the rotation of the Earth —is dominant such that $R_O, R_{O_T} \ll 1$[13] and ignoring frictional effects, the lowest-order equations governing such a fluid in the horizontal x, y-plane are the following simplified expressions of the equations of motions:

$$-fv = -\frac{1}{\rho}\frac{\partial p}{\partial x} \tag{6a}$$

$$+fu = -\frac{1}{\rho}\frac{\partial p}{\partial y} \tag{6b}$$

This synoptic[14] geophysical flow —in which there is a balance between the scaled horizontal velocity by the Coriolis parameter f on the left hand side of Eq. 6 and the horizontal pressure gradient on the right hand side of the equation —is called *geostrophic* and the balance is referred to as the *geostrophic balance*. The process in which this balance in a fluid is restored is termed as the *geostrophic adjustment*.

Now the geostrophic adjustment theory is discussed, it becomes apparent how large-scale wind field information above e.g. oceanic regions can be determined indirectly when accurate pressure information is known. However, the geostrophic adjustment theory can in practise not be utilized when there is a lack of accurate pressure information. Furthermore, the latter provides only indirectly wind field information and therefore not directly. This gives a physical argument why direct wind observations near these regions are crucial due to the lack of applicability of the geostrophic adjustment theory.

Because the Coriolis parameter [Eq. 5] varies with the sinus of the latitude, the wind will be deflected to a greater extent at higher latitudes than in the tropics. Conversely, this statement is not valid when approaching the tropics where the Coriolis parameter f vanishes as $\sin(\phi)$ converges to zero. As a result, the geostrophic adjustment theory does not hold in the tropics and direct wind measurements are required in order to determine the flow and weather development in this region [see e.g. Stoffelen et al., 2005]. This provides a second argument of the urge of direct wind observations and hence the introduction of Aeolus.

A third argument is based on the relationship between the geostrophic adjustment theory and the *Rossby radius of deformation*. This deformation radius is defined as:

$$R := \frac{\sqrt{gH}}{2\Omega \sin\phi} \tag{7}$$

where H is the depth of the atmospheric vertical structure —i.e. vertical length scale —the denominator represents the expression for the Coriolis parameter f, and g the gravitational acceleration of the Earth. The Rossby radius of deformation R is an import horizontal length

[12] In honor of the famous Swedish meteorologist Carl-Gustav Arvid Rossby (1898 - 1957) which contributed with most of the fundamental principles within the field of geophysical fluid dynamics.

[13] When $R_O, R_{O_T} \ll 1$, the total time derivative D/Dt $\ll 1$, implying a steady flow.

[14] I.e. a large scale atmospheric flow with a length scale in the order of $\geq$ 1000 km at which atmospheric dynamics is dominated by mass field information rather than wind field information.

scale at which the wind and mass field obey approximately a geostrophic balance [Eq. 6] such that the theory of geostrophic adjustment can be applied. According to Stoffelen et al. [2005], it is only for atmospheric motion systems with a horizontal length scale $L \gg R$ and *shallow*[15] vertical structures ($H \ll L$) for which the mass field information can be derived based on the geostrophic adjustment theory —denoted by the grey shaded area of Fig. 5. Conversely for horizontal length scales smaller than R with *deep* vertical structures ($H \gg L$), the wind and mass field are not directly coupled —depicted by the open white area of Fig. 5. As a result, the geostrophic adjustment theory does not hold anymore and direct wind observations are required. This provides a third argument why direct wind measurements are crucial for these smaller scale features.

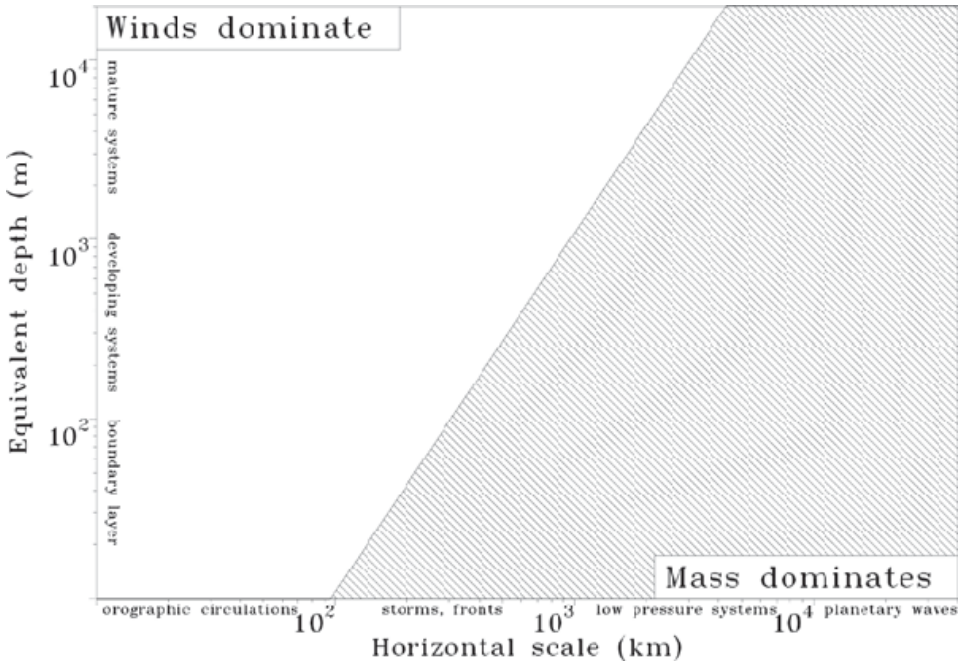

Figure 5: The straight diagonal line represents the Rossby radius of deformation R for a latitude of $\phi = 45°$ as a function of the horizontal length scale and the depth of the atmospheric vertical structure H. The open white area denotes the range at which atmospheric dynamics is dominated by wind field information for small horizontal scale features ($L \ll R$) with deep vertical structures ($H \gg L$). The grey shaded area denotes the range at which mass field is important and dominating the large scale atmospheric dynamics ($L \gg R$) with shallow vertical structures ($H \ll L$). *Source:* Stoffelen et al. [2005].

2.3.2 The concept of potential vorticity

The second concept which sheds some light on the need of wind measurements is the concept of *Ertel's potential vorticity*[16] (PV) which will be elaborated in this section.

[15]Shallow vertical structures implies that the vertical scale (H in Eq. 7) $\ll$ horizontal length scale L. A counterpart is a *deep* vertical structure such as deep convection clouds like *cumulonimbus* clouds.

[16]Named after Hans Ertel (1904 - 1971), a German natural scientist and a pioneer in the disciplines of geophysics, meteorology and hydrodynamics.

In dynamical meteorology PV is an important geophysical quantity in the study of the initialization and evolution of dynamic atmospheric structures on a synoptic scale in a rotating system, such as the atmosphere of the Earth. The theory of PV originates in the *Bjerknes circulation theorem* (1898)[17] —generalized from the *Helmholtz's vorticity theorem* (1859)[18] and an extension of *Kelvin's circulation theorem* (1869)[19]. Bjerknes postulated this theorem since the Helmholtz's vorticity equation and Kelvin's circulation theorem assumed a fluid with a constant density —i.e. a *barotropic* fluid —and hence resulted in a limited applicability in geophysical fluid dynamics since not all fluid systems are barotropic. Therefore Bjerknes circulation theorem is based on an inviscid and a *baroclinic* fluid in which the density is not constant.

Ertel's PV on an isentropic[20] surface is defined as [see e.g. Holton, 2012]:

$$PV := \Pi = (\zeta_\theta + f)\left(-g\frac{\partial\theta}{\partial p}\right) = constant, \tag{8}$$

with $[10^{-6}\ \mathrm{m^2\ s^{-1}K\ kg^{-1}}]$ as the Potential Vorticity Unit (PVU)[21]. The ζ_θ-term is the two-dimensional vertical[22] component of the *relative vorticity*:

$$\zeta_\theta := curl_{\mathbf{k}}\mathbf{V} \equiv (\nabla \times \mathbf{V}) \cdot \mathbf{k} = \left(\frac{\partial v}{\partial x} - \frac{\partial u}{\partial y}\right)_\theta, \tag{9}$$

and is defined on an isentropic surface, denoted by the subscript 'θ'. The f-term is designated as the *planetary vorticity* and becomes the Coriolis parameter [Eq. 5] when the vertical component of the planetary vorticity is taken. The relative vorticity and planetary vorticity together results in the *absolute vorticity* ζ_{abs}:

$$\zeta_{abs} := \zeta_\theta + f, \tag{10}$$

in which the term $-\partial p/g\partial\theta$ is identified as the *isentropic density* σ of the fluid element (unit: $[\mathrm{kg\ m^{-2}\ K^{-1}}]$) with $\partial\theta/\partial p$ being the *static stability* with θ as the *potential temperature*. The isentropic density σ represents the influence of mass field as wind velocity and potential temperature on the PV quantity [Eq. 8] on certain isentropic levels.

[17] Vilhelm Friman Koren Bjerknes (1862 - 1951), a Norwegian meteorologist, physicist and professor of mathematical physics at the University of Stockholm and one of the pioneers in modern science of weather forecasting.

[18] Hermann Ludwig Ferdinand von Helmholtz (1821 - 1894), a German mathematician, physicist and physician who established several aerodynamic basic principles. The *Helmholtz's vorticity theorem* describes the three-dimensional motion of an inviscid and incompressible flow in the vicinity of a material line element of vorticity, referred to as a *vortex filament*.

[19] William Thomson, 1^{st} Baron Kelvin (1824 - 1907), was a Scots-Irish engineer, mathematical physicist and pioneer in different disciplines —in particular electromagnetism and thermodynamics. The *Kelvin's circulation theorem* postulates that the time rate of change of circulation around a closed curve consisting of the same fluid elements is zero.

[20] An *isentropic surface* is a surface with constant potential temperature θ everywhere along that surface, i.e. an *isosurface* of constant θ.

[21] In dynamical meteorology —the PVU is used to express the boundary between the troposphere and stratosphere, designated as the *dynamical tropopause*, which is usually set at 2PVU [see e.g. van Delden, 2017].

[22] The two-dimensional vertical component of the relative vorticity ζ_θ is taken since geophysical flows typically have a low *aspect ratio*, i.e. the vertical scale $\ll$ horizontal scale.

Since Π in Eq. 8 is set equal to a constant, it implies that the quantity is materially conserved along the fluid trajectory under adiabatic conditions[23]. I.e., if either the absolute vorticity of the fluid column or the static stability changes, the counterpart must adjust to compensate. Hence the PV theory implies that the rotation rate of an arbitrary fluid column changes when the column is expanded or contracted vertically [Fig. 6]. As PV is a conserved quantity, PV is advected like a materially conserved chemical tracer. As a result, significant atmospheric structures on a synoptic scale can be identified and traced spatially and temporally —a very powerful virtue of the PV theory to study the initialization and evolution of such weather systems.

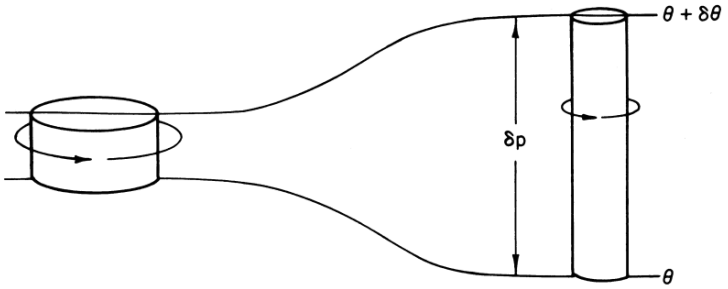

Figure 6: Illustration of the potential vorticity theory. An arbitrary fluid column follows the trajectory of the fluid motion adiabatically while conserving potential vorticity. *Source:* Holton [2012].

As there is a robust link between the PV distribution and mass field information such as wind velocity and potential temperature, the *invertibility principle of potential vorticity* allows one to obtain mass field information when the atmosphere is in a balanced state [see e.g. van Delden, 2017]. With use of the invertibility principle it is possible to quantify PV *anomalies* at upper and lower atmospheric levels. PV anomalies influence the initial state of NWP models and are important to detect precursor atmospheric features such as the development of extra-tropical cyclones in which the generation of vorticity takes place. These features are referred to as *cyclogenesis* and their numerical predictability is sensitive to subtle differences in PV anomalies, as it influences the initialization of NWP. Conversely, direct wind measurements as measured by Aeolus will contribute to global wind field information and therefore contribute in identifying PV anomalies in the atmosphere.

Despite that extra-tropical cyclones are predicted several days in advance due to the high accuracy of current numerical models and the four-dimensional atmospheric data assimilation technique (referred to as *4D-Var*), there are still atmospheric features not being predicted accurately due to e.g. deficiencies in data assimilation [Wernli et al., 2002]. Hence to better observe rapidly developing PV anomalies, wind field information becomes even more important than mass information. This provides an argument —based on the potential vorticity theory —why direct wind measurements of Aeolus are essential.

[23]Materially conserved implies that $d\theta/dt \equiv 0$, i.e. no mixing nor friction nor diabatic effects.

3 Aeolus satellite-derived meteorological data

Initially a short overview about the orbit geometry of the satellite of Aeolus will be introduced [Sec. 3.1], before elaborating on its wind retrieval principle [Sec. 3.2].

3.1 Orbit geometry

Aeolus was taken into orbit at August 22^{th} of 2018 at 21:30 UTC from ESA Europe's spaceport *Centre Spatial Guyanais* in Kourou (French Guiana). The launch was performed by Arianespace —the leading satellite launch customer of ESA —with a VEGA rocket. Aeolus is an *Earth Explorer* demonstration mission —i.e. a science and research related mission —and has a nominal lifetime of about three years. The lifetime of the mission mainly depends on the quality and performance of the on-board laser instruments and the amount of propellant to keep the satellite in obit and prevent *orbit drifting*.[24]

The satellite orbits in a *near-polar orbit* with an inclination of 96.97°, ∼16 orbits a day with an *Earth-repeat cycle*[25] of ∼7 days (111 orbital revolutions), and a local equator crossing time of 06:00 *ante meridiem* for the descending orbit and 06:00 *post meridiem* for the ascending orbit. Earth observation satellites such as Aeolus are frequently set in a near-polar orbit due to its global mapping coverage possibilities as the Earth rotates underneath the satellite. The satellite orbits in a *low-Earth-orbit* with an orbit altitude of ∼320 km and is set in a *dawn-dusk* orbit. This orbit type is characterized as a *Sun-synchronous orbit*, i.e. a near-polar orbit where the nodal *precession rate*[26] matches the mean orbital rate of the Earth around the Sun. The orbit is set in a Sun-synchronous orbit such that the laser points most of the time[27] towards the night side of the Earth to reduce noise from the light of the Sun and therefore increase the signal-to-noise ratio (SNR). Specifications are summarized in Tab. 1.

orbital parameter	**specification**
Nominal life-time	3 years
Inclination	96.97°
Orbit type	near-polar dawn-dusk
Orbit altitude	320 km
Orbits a day	16
Earth-repeat cycle	7 days, 111 orbits
Local equator crossing time	06:00 a.m. (descending node), 06:00 p.m. (ascending node)

Table 1: Aeolus orbital features. Note that all specifications are approximates and hence not fixed. More information can be found in the *System Requirements Document* (`AE-RS-ESA-SY-001`) of ESA.

[24] To maintain a stable orbit over a long period of time, corrections in the orbit geometry from the ground are required to prevent orbit drifting due to atmospheric losses and gravity drag. The latter requires on-board propellant.

[25] Earth-repeat cycle implies that the ground track of the satellite repeats after j days and k orbital revolutions.

[26] In the field of astronomy, the *precession rate* (or *precession*) of an astronomical body refers to a steady and slow change of its rotational or orbital parameters in time.

[27] Due to seasonal dependency.

3.2 Wind retrieval principle

The observation satellite is built by *Airbus Defence and Space* and is the first satellite mission which provides wind profile observations on a global scale. It is the first satellite using the Doppler wind lidar[28] measurement technique from space with the Atmospheric Laser Doppler Instrument (ALADIN) as measurement instrument. ALADIN uses the principle of light scattering and the direct-detection concept of the *Doppler effect*[29] to measure the wind.

3.2.1 Dual-channel receiver and detection measurement concept

While the satellite orbits the Earth in a near-polar dawn-dusk orbit —the lidar of ALADIN emits a series of short ultra-violet (UV) pulses 35° off-nadir along its line-of-sight (LOS) and perpendicular to the ground track velocity. The UV pulses have a wavelength of about 355 nm with a pulse rate of 50 Hz, and beams along the LOS of the emitted laser into the atmosphere.

The receiver optics of ALADIN consist of two different spectrometers. The instrument uses two sequential *Fabry-Pérot*[30] interferometers and a *Fizeau*[31] interferometer. The Fabry-Pérot interferometer is used to measure the Doppler shifted frequency of the broad spectrum resulting from *Rayleigh-Brillouin*[32] scattering of molecules in the atmosphere. The Doppler shifted frequency of the narrow-bandwidth Mie[33] spectrum due to Mie scattering of particles and aerosols is measured by the Fizeau interferometer. The LOS wind is derived from a Doppler shifted frequency in the backscattered signal. The Doppler shift is proportional to the average velocity component of the backscattered signal. The average motion is considered to be the wind [Tan et al., 2007]. An accumulating charged-coupled device (ACCD) is used for the detection of both backscattered signals which allows for data retrieval in 24 *range-bins* —resulting into a wind profile discretized into 24 layers with adjustable vertical resolution. The dual-channel receiver and detecting concept gives rise to wind observations measured in two independent channels —the Rayleigh channel and Mie channel.

The *double-edge* Fabry-Pérot technique [see e.g. Chanin et al., 1989; Garnier and Chanin, 1992] is used for the determination of the Doppler shifted frequency from the Rayleigh-Brillouin backscattering spectrum in the Rayleigh channel and involves two bandpass filters (filter A and B) which are symmetrical around the emitted UV laser frequency [Fig. 7]. A measure of the Doppler shifted frequency between the emitted and backscattered signal

[28] Lidar is an acronym for *Light Detection and Ranging of Laser Imaging Detection and Ranging* which is a remote-sensing method used to measures the distance between the point of the emitted laser signal and the point of the backscattered laser signal due to an object. Lidar instruments are being used extensively for e.g. atmospheric research and meteorology but not yet from space. This makes the observation satellite of Aeolus unique.

[29] Named after the Austrian mathematician and physicist Christian Johann Doppler (1803 - 1853) who invented the Doppler effect.

[30] The Fabry-Pérot interferometer is invented and named after the French physicists Maurice Paul Auguste Charles Fabry (1867 - 1945) and Jean Baptiste Gaspard Gustave Alfred Pérot (1863 - 1925) in 1897.

[31] Named after Armand Hippolyte Louis Fizeau (1819 - 1896), a French physicist and known for e.g. the measurement of the speed of light, referred to as the *Fizeau experiment*.

[32] In honor of John William Strutt, 3^{th} Baron Rayleigh (1842 - 1919), a British scientist in theoretical and experimental physics, and the French physicist Léon Nicolas Brillouin (1889 - 1969) which made contributions in the fields of e.g. quantum mechanics and solid state physics.

[33] Named after the German physicist Gustav Adolf Feodor Wilhelm Ludwig Mie (1868 - 1957).

is described by the contrast between the backscattered signal I_A and I_B in filter A and B respectively. A Doppler shift to the right from the centroid position results in $I_A > I_B$ —while $I_A + I_B$ varies slightly —resulting into an increase in the response signal in the Rayleigh channel and hence a measure for the LOS wind measurement.

The measurement principle in the Mie channel for the narrow-bandwidth Mie backscattering spectrum as measured by the Fizeau interferometer relies on the *fringe-imaging* technique [McKay, 2002]. The measure of the Doppler shifted frequency is described by the quasi-linear relationship between the centroid position of the fringe and its position after the Doppler frequency shift [Fig. 7].

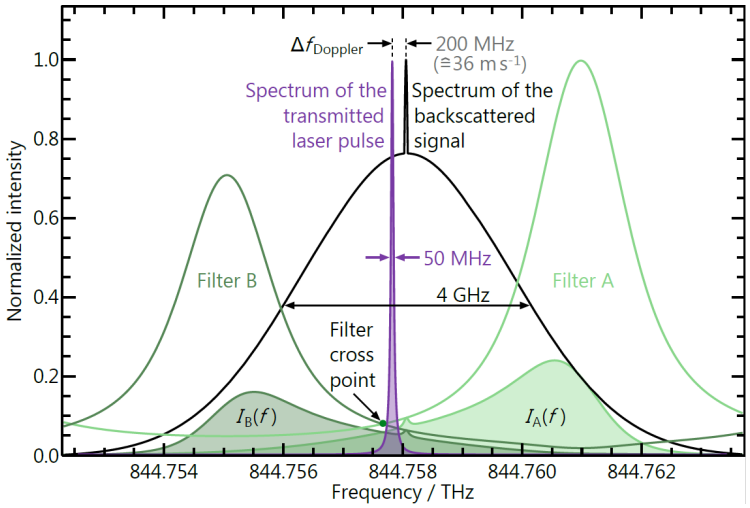

Figure 7: Spectral distribution of the transmitted UV laser by ALADIN along the LOS (purple) and the spectrum of the backscattered signal by the atmosphere (black). The spectral distribution can be decomposed into the narrow-bandwidth Mie scattering spectrum and the wide-bandwidth Rayleigh-Brillouin backscattering spectrum. A Doppler shifted frequency in the order of e.g. $\Delta f_{Doppler} \approx 200$ MHz results into a LOS wind velocity in the order of ~ 36 ms^{-1}. *Source:* Lux et al. [2018].

3.2.2 Scattering intensity

The intensity of Mie and Rayleigh-Brillouin scattering follows the theory of the *Lambert-Beer law*[34] for absorption. This theory describes the extinction of a signal out of an arbitrary parallel beam by scattering. The mathematical formalism is described as:

$$\frac{dI_\lambda}{I_\lambda} = -\sigma_{scatt,\lambda} \cdot c \cdot ds \tag{11}$$

which states that when a parallel beam of light traverses a certain volume, the fractional loss of the radiation I_λ is the product of the scattering cross-section $\sigma_{scatt,\lambda}$, the concentration of the scatterer c and the path length ds.

[34] A physical law postulated by the works of the German mathematician, physicist and chemist August Beer (1825 - 1863) and the German-Swiss scientist Johann Heinrich Lambert (1728 - 1777).

The intensity of Mie and Rayleigh-Brillouin scattering determines the wind-retrieval algorithms and hence the accuracy of the measurements. The intensity of scattering in both channels are in line with the Lambert-Beer law [Eq. 11] since Mie scattering depends on the presence and *optical depth*[35] of aerosols and the concentration of clouds [Marseille and Stoffelen, 2003]. Nevertheless, the lidar cannot penetrate optically thick clouds. For the Rayleigh channel, the concentration of molecules in the atmosphere determines the intensity of the Rayleigh-Brillouin backscattering.

3.2.3 Horizontal measurement resolution

Within Aeolus nomenclature, a distinction is made between a *measurement* and an *observation*. Together with a mean ground track velocity of the satellite of $\mathbf{V}_{sat} \approx 7.35$ km s^{-1} and a laser pulse rate of about 50 Hz —after approximately each 147 m along the orbit track there is a laser pulse P. The accumulation of P pulses typically varies between 20 and 50 and determines the horizontal resolution of the retrieved LOS wind. When $P = 20$, the along-track distance is about 2.94 km and these accumulated pulses are denoted as a *measurement* N. Averaging N measurements forms one single *observation* in which $1 \leq N \leq N_{max}$, where $N_{max} \sim 30$[36]. The amount of accumulated measurements determines the *integration length* L_{int} of the observation, which is basically the sampling length of the observations. The integration length varies between 2.94 km for $N = 1$ to about 88.2 km when $N = N_{max} \approx 30$.

Prior the accumulation process, measurements are classified into different types, e.g. *clear* and *cloudy*. Typically it expected that $L_{int} \sim 88.2$ km, but smaller integration lengths can be observed due to the classification —especially for the Mie channel when the air is not *all cloudy* along the full integration length of 88.2 km [Fig. 8].

[35] In cloud physics, the optical depth is a measure of the absorption or scattering of radiation by an optically active medium such as particles or clouds. For example, high altitude *cirrus clouds* are very cold clouds which contain a low moisture density and tiny ice crystals, resulting into a cloud with a relative low optical depth.

[36] At this moment $N_{max} \sim 30$, however the L2B processors are flexible and N_{max} can be adjusted such that $N_{max} > 30$ is possible. Time of writing: 07/07/2019.

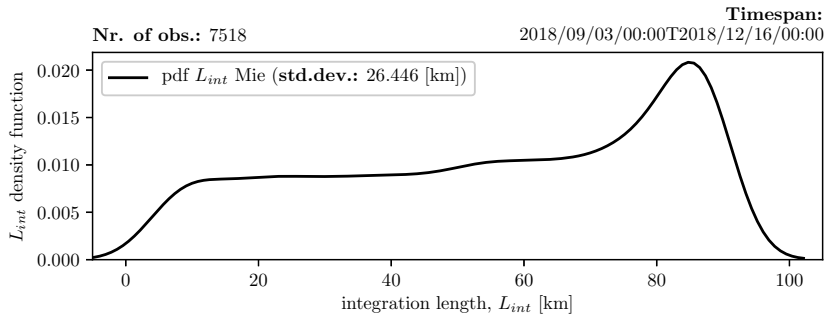

(a)

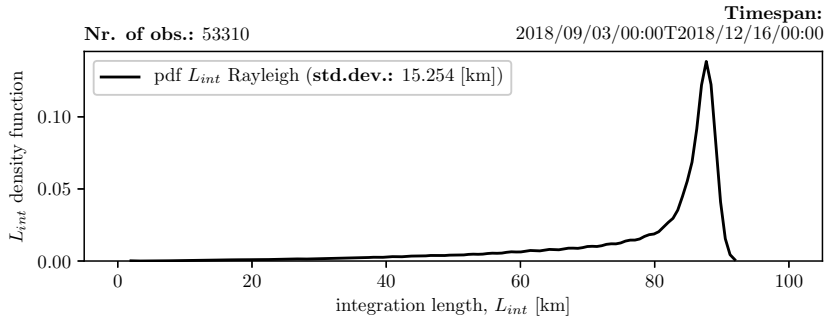

(b)

Figure 8: A probability density function (PDF) plot of the integration length L_{int} for (a) the Mie channel and (b) the Rayleigh channel. As the Mie channel accounts for Mie scattering of particles and aerosols, the *cloudiness* along track determines L_{int} significantly —indicated by a large variance in L_{int} in the density plot. The Rayleigh channel accounts for Rayleigh-Brillouin scattering of molecules in typically clear air such that greater values for L_{int} are observed.

3.2.4 Vertical measurement resolution

Wind observations are measured w.r.t. the geoid —as described by the Earth Gravitational Model 1996 (EGM96) —and sorted within vertical *range-bins* [Fig. 9]. These range-bins vary in height between 0.25 - 2.0 km and each wind profile has in total 24 range-bins per channel. The vertical resolution of each range-bin is flexible and can be adjusted with an integer of 0.25 km. The sampling resolution per profile can be altered eight times per orbit which allows for different sampling scenarios for different global regions [Marseille et al., 2013]. Studies performed by Marseille et al. [2013] demonstrated e.g. to be beneficial to alter the sampling resolution along track by positioning Mie range-bins up to 11 km near the Poles[37] while positioning up to 18 km is advantageous when crossing tropical regions to sample e.g. *cirrus* clouds.

[37]During polar winter, extending the vertical sampling up to an altitude of even 15 - 25 km becomes advantageous in order to sample high altitude *Polar stratospheric clouds* —which play an important role in the Antarctic ozone destruction.

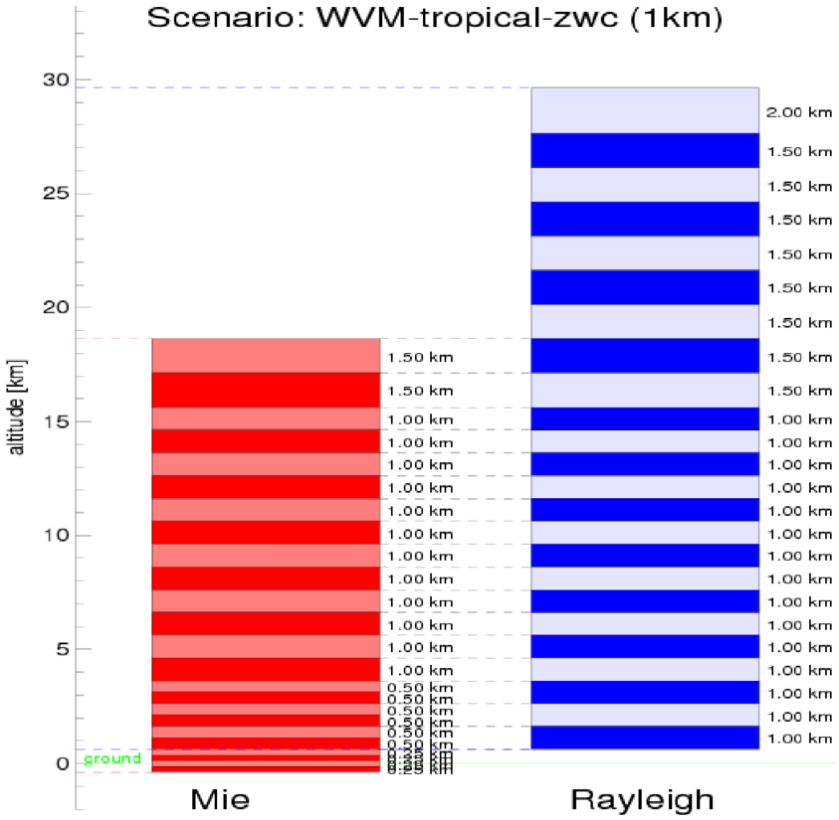

Figure 9: Different and independent vertical resolution sampling scenario for (left) the Mie channel, and (right) the Rayleigh channel —as used in the *Vertical and Horizontal Aeolus Measurement Positioning* study [Marseille et al., 2013]. Sampling scenario studies performed by Marseille et al. [2013] demonstrated a range-bin of at least 1 km for the Rayleigh channel is required in order to meet the mission requirements. Decreasing the range-bin width below this value results into a decrease in the SNR, and hence observational wind errors. *Source:* Marseille et al. [2013].

3.2.5 HLOS wind derivation and geometry

Lorenc et al. [1992] demonstrated that the ECMWF model is capable of assimilating single wind components and improve the quality of weather forecasting. Impact studies performed by Horanyi et al. [2013, 2006] demonstrated that the single LOS wind component can represent approximate 75% of the full wind vector in the extra-tropics and tropics —particularly for the medium-range forecast. The ECMWF model is able to derive the true wind vector based on single LOS wind observation for 75% [Horanyi et al., 2013, 2006]. Moreover, [Horanyi et al., 2006] demonstrated the impact of zonal wind observations to be larger than the meridional wind observations. In addition, monthly means of daily means in wind direction is zonally [Fig. 10] —Aeolus will mostly measure the wind in the atmosphere along the zonal direction.

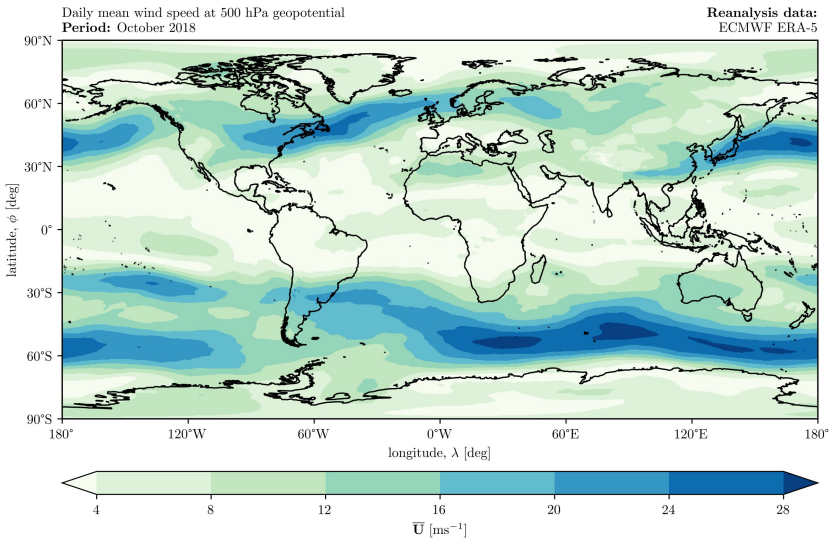

Figure 10: Geographical illustration of monthly mean of daily means in wind direction for the month of October 2018 at 500 hPa geopotential utilized ERA5 reanalysis data —demonstrating the mean wind to be zonally on a global scale. Clearly noticeable are the mid-latitude *Rossby waves* with the locations of *jet streams* —blue regions.

The LOS wind is derived from a Doppler shifted frequency in the backscattered signal. The Doppler shift is proportional to the average velocity component of the backscattered signal. The average motion is considered to be the wind [Tan et al., 2007]:

$$\Delta f_{Doppler} = -\frac{2\mathbf{V}_{LOS}}{\lambda_{sat}} \tag{12}$$

for which the measured Doppler shifted frequency of the backscattered signal is denoted by $\Delta f_{Doppler}$, while λ_{sat} represents the *a priori* known wavelength of the laser emitted by ALADIN, and the wind velocity measured along the line-of-sight of the instrument is denoted by $\mathbf{V}_{LOS}$. As the horizontal length scale of horizontal atmospheric motions is on average $\gg$ the vertical length scale of the vertical atmospheric motion, the vertical component of the full LOS wind vector is neglected [European Space Agency (ESA), 2016] —resulting into the two-dimensional horizontal line-of-sight (HLOS) wind vector. The HLOS wind observation can be retrieved by projecting the measured LOS wind observation onto the horizontal plane by dividing the LOS wind observation with the sinus of the *local incidence angle* θ [Fig. 11]:

$$\mathbf{V}_{HLOS,i} = \frac{\mathbf{V}_{LOS,i}}{sin\theta} \tag{13}$$

where i represents the range-bin index. However, the local incidence angle θ is not reported by the instrument and depends on the geoid curvature of the Earth —as described by the EGM96. Nevertheless, the *local elevation angle* β is reported by the instrument and used to determine the local incidence angle geometrically.

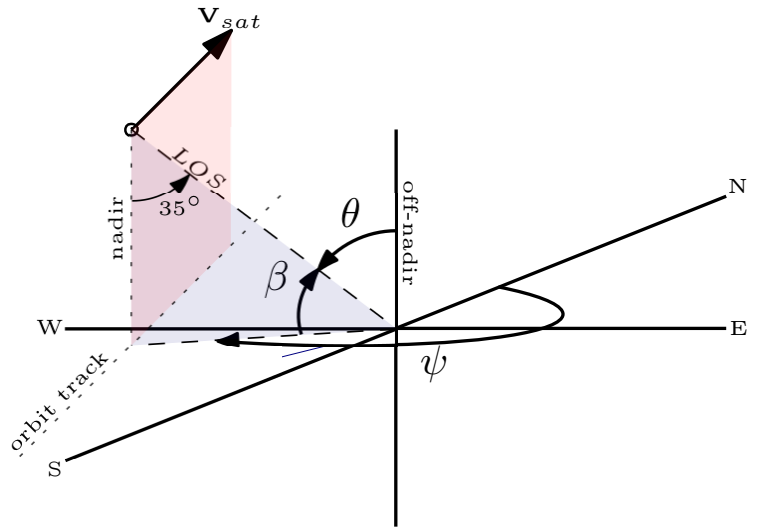

Figure 11: Geometry for the (horizontal) line-of-sight wind observation during the ascending orbit phase. Note that $\beta \neq 180°$ - $90°$ - $35°$ since β depends on the local elevation —i.e. the local orography as described by the EGM96.

The HLOS wind vector [Eq. 13] can be —when corrected for the the *azimuth angle* ψ, which is the angle clockwise from north of the target-to-satellite pointing direction —decomposed into the zonal and meridional u, v-wind components respectively:

$$\mathbf{V}_{HLOS} = \mathbf{u}' - \mathbf{v}' = -\mathbf{u}\sin\psi - \mathbf{v}\cos\psi. \tag{14}$$

Conversely, the *a priori* known u, v-wind components e.g. from a NWP model can be utilized to construct V_{HLOS} for e.g. data assimilation purposes. A graphical illustration of Eq. 14 is shown in Fig. 12.

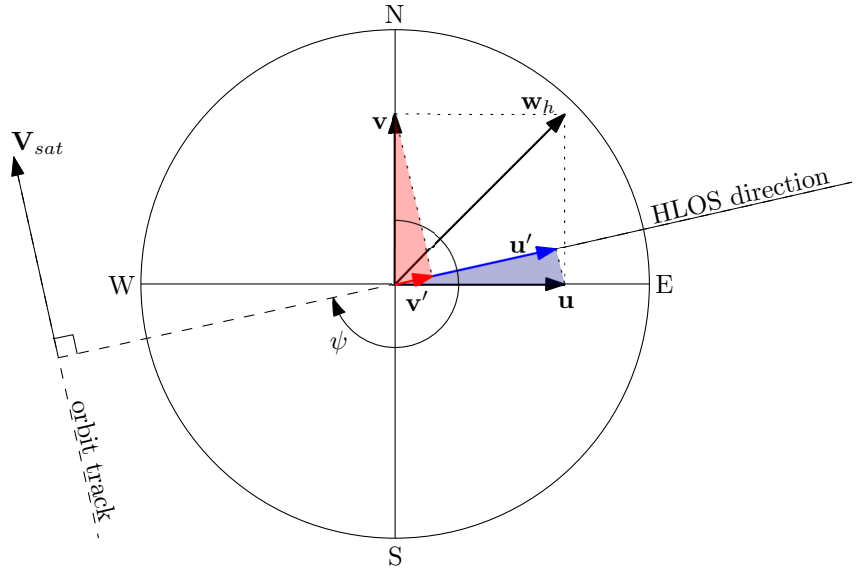

Figure 12: Top-down geometry view of figure 11. Vector projection of the wind components **u** and **v** onto the vector component of the LOS.

The sign convention of Eq. 14 states that the HLOS wind is defined to be positive when the advection of the measured atmospheric wind is away from the ALADIN instrument [Fig. 13] —i.e. a reduced frequency of Doppler shift. Conversely, when the advection of the measured wind is towards the instrument the HLOS wind is defined as negative. Hence a positive or negative HLOS wind does not imply an eastward or westward wind respectively.

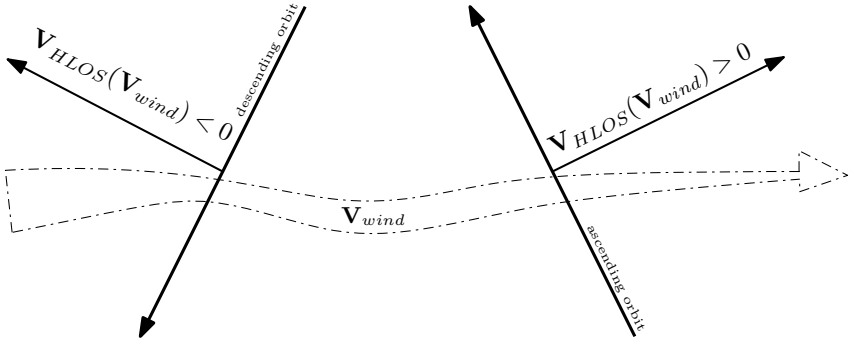

Figure 13: Geometrical sign convention for the HLOS wind definition [Eq. 14]. Assume an eastward advection of the atmospheric wind —during the ascending orbit phase the instrument will measure a positive HLOS wind since the measured wind is being advected away from the instrument. Conversely, during the descending orbit phase a negative HLOS wind will be measured by the instrument since the measured wind is being advected toward the instrument while the atmospheric wind is still eastward.

As the horizontal length scale of horizontal atmospheric motions is on average $\gg$ the vertical length scale of the vertical atmospheric motion, the vertical component of the full LOS wind vector is neglected [European Space Agency (ESA), 2016]. It is also worthwhile to discuss when the vertical component is not negligible. E.g.:

- when $3 \leq L_{int} \leq 7$ km, i.e. when the horizontal length scale of the Aeolus wind observation is not $\gg$ the vertical length of the range-bin. However, the probability density function plot of L_{int} [Fig. 8] demonstrated no significant probability for the case in which $3 \leq L_{int} \leq 7$ km.

- weather systems with a high *Convective Available Potential Energy*[38] index —resulting into convective situations with strong *updrafts* and *downdraft*, or above high convective clouds such as *cumulonimbus* clouds. However, the laser of Aeolus is not able to penetrate optically thick clouds.

- in the presence of baroclinic waves in the atmosphere —e.g. *gravity waves* —in which air parcels undergo buoyancy oscillations about its equilibrium level with a certain amplitude equal to its initial displacement and a *Brunt-Väisälä frequency*[39].

- during the occurrence of atmospheric turbulence in the planetary boundary layer (PBL), or at higher altitudes in e.g. the troposphere —referred to as *clear-air turbulence*.

3.2.6 Atmospheric corrections to HLOS wind retrieval

According to the studies performed by Dabas et al. [2008], the LOS winds in the Rayleigh channel requires primarily to be corrected for atmospheric pressure and temperature effects due to the Rayleigh-Brillouin effect and must be considered as a source of systematic errors in wind retrievals. Atmospheric pressure and temperature creates individual thermal movement of molecules due to the *Brownian motion*[40]. Since the measurement instrument does not measure these atmospheric quantities, it requires *a priori* knowledge on the actual ambient pressure and temperature inside the geolocated atmospheric sensing volume of the wind measurement. The Aeolus product processors utilizes pressure and temperature data from the ECMWF IFS model to correct for the Rayleigh-Brillouin effect. These necessary data are stored in the auxiliary meteorological `AUX_MET` data.

3.2.7 Aeolus wind products

The Input/Output Data Definition (`IODD`)[41] technical note of ESA provides a description of the definition of the input and output of the Aeolus wind products. According to the `IODD`, the L2B/2C products contain profiles of the horizontal wind component at the observation scale —derived from meteorologically-weighted averages of the L1B measurement data. Moreover, it contains information about the error estimates and validity of the wind observation and are geolocated —date, time and position. The operational L2C product is

[38] The *Convective Available Potential Energy* [J kg^{-1}] —or in short CAPE —of a certain reference air parcel is a meteorological measure to quantify the amount of upward buoyant force per unit volume of a rising air parcel due to temperature gradients between the parcel and its environment, [see e.g. Holton, 2012; Wallace and Hobbs, 2006].

[39] The *Brunt-Väisälä frequency* is in meteorology and oceanography a measure of the static stability of an fluid parcel —i.e. the higher the frequency, the greater the ambient stability [see e.g. Holton, 2012; Wallace and Hobbs, 2006]. This measure is named after the English meteorologist Sir David Brunt (1886 - 1995) and the Finnish meteorologist Vilho Väisälä (1899 - 1969).

[40] Brownian motion - also known as *pedesis* - is the random motion of particles in a fluid (liquid or gas) due to their collisions with other fast-moving molecules. This motion is named after Robert Brown (1773 - 1858), a Scottish botanist and palaeobotanist.

[41] The `IODD` is documented in the technical note `AE-IF-ECMWF-L2BP-001` of ESA.

product/data set	**content**	**remarks**
Level 0	Raw instrument and housekeeping data	Includes unprocessed data about the *attitude and orbit control system* of the satellite, and quality control parameters.
Level 1A	Geolocated and unprocessed observational data	Includes processed housekeeping data.
Level 1B	Geolocated and fully calibrated observational processed data	Preliminary (H)LOS wind observations based on e.g. atmospheric instrument corrections, processed calibration and quality control parameters.
Level 2A	Supplementary geophysical products	Geophysical products such as cloud and aerosol information, e.g. backscatter-to-extinction ratio or the optical depth.
Level 2B	Consolidated HLOS wind observations for the Mie and Rayleigh channel	External atmospheric state variables as pressure and temperature are used to perform corrections for the Rayleigh-Brillouin effect.
Level 2C	Super-set of the Level 2B product containing the assimilated wind observations	Vector-wind profiles derived from NWP assimilation processes using the Level 2B product.

Table 2: Aeolus wind products. More information: see e.g. `AE-IF-ECMWF-L2BP-001`. For this validation research —the Level 2B (L2B) observational data is utilized.

a superset of the L2B product in which the HLOS wind observations are assimilated in the NWP model of the ECMWF IFS. A short descriptive overview of these products is listed in Tab. 2.

3.2.8 Mission requirements

The IODD also provides the mission requirements for the HLOS wind observations. These requirements are summarized in Tab. 3.

	unit	**PBL**	**troposphere**	**stratosphere**
vertical domain	[km]	0 - 2	2 - 16	16 - 20 (30)
vertical resolution	[km]	0.5	1.0	2.0 - 5.0
horizontal domain			global	
horizontal resolution	[km]		3 - 90	
number of profiles	[hour^{-1}]		$\geq$100	
measurement error	[ms^{-1}]	1.0	2.0 - 3.0	3.0 - 5.0
systematic error	[ms^{-1}]	0.7	0.7	0.7
measurement range	[ms^{-1}]		$\pm$ 100 (150)	
nominal lifetime	[year]		3	

Table 3: Aeolus HLOS observation requirements for the planetary boundary layer (PBL), troposphere and stratosphere. Note that the horizontal resolution is based on the integration length L_{int} [Sec. 3.2.3]. More information can be found in the *System Requirements Document* (AE-RS-ESA-SY-001) of ESA.

4 Mode-S EHS aircraft-derived meteorological data

Together with temperature —atmospheric wind information is essential when assimilated in a NWP model. The current GOS of the WMO receives these kind of observations from several *in situ* or remote-sensing based observing systems [see Sec. 2.2]. Also aircraft are able to contribute to this observing system as an additional meteorological sensor.

Commercial aircraft are equipped with meteorological sensors such as a pitot tube and a barometric static port[42] for flight operations and flight monitoring. For this purpose, an aircraft measures e.g. the atmospheric pressure and temperature —next to its speed and position —during all flight phases.

4.1 ICAO Mode-S EHS data

A novel type of aircraft-derived meteorological observational data is the mode-selective (Mode-S) enhanced surveillance (EHS)-derived data, which has been standardized by the *International Civil Aviation Organization*[43]. Mode-S is a surveillance radar process which allows selective tracking and interrogating aircraft-derived observational data from on-board systems such as aircraft identity, heading, air speed and position (Fig. 14). This essential information are primarily used for air traffic control services.

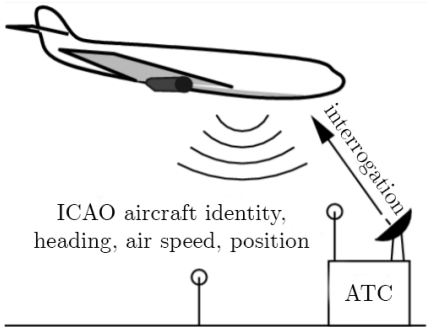

Figure 14: Aircraft-derived Mode-S EHS data such as aircraft identity, heading, air speed and position can be received by interrogation of the surveillance radar of the air traffic control (ATC). *Source:* adapted from de Jong et al. [2018].

The Royal Dutch Meteorological Institute (KNMI) started to research the utilization of these aircraft-derived meteorological Mode-S EHS data in 2008 on request of the *Air Traffic Control The Netherlands* for air traffic management purposes. de Haan and Stoffelen [2012] used Mode-S EHS data to assess the impact for nowcasting and short-range forecasts up to 2-3 hours and is found to be beneficial.

[42]The pitot tube measures the *stagnation pressure* while the static port measures the *static pressure*. Both pressures determine the air pressure gradient, i.e. the difference between the two pressures —resulting in the *dynamic pressure*. The dynamic pressure is used by air data instruments of the aircraft to determine the airspeed and pressure altitude of the aircraft.

[43]The International Civil Aviation Organization (ICAO) is an international agency of the United Nations, specialized in the civil aviation industry and is responsible for e.g. standardization, aviation law and airworthiness of aircraft. See `www.icao.int`.

4.1.1 Accuracy and resolution

Mode-S EHS data is a quality controlled proven meteorological representative data set at high resolution. Studies demonstrated the quality and quantity of these data —in comparison to global NWP model forecast results from the ECMWF IFS —and depicted that the data set is nearly unbiased [see e.g. de Haan, 2014] after applying necessary corrections as discussed by [de Haan, 2011, 2013]. Moreover, de Haan [2016] demonstrated that the observation error of the Mode-S EHS wind in the zonal and meridional direction is estimated to be less than 1.4 ± 0.1 ms^{-1} near the surface and approximately 1.1 ± 0.3 ms^{-1} at a geopotential height of 500 hPa.

For the temporal resolution —the surveillance radar has an interrogation frequency of once every 4 to 20 seconds. Consequently, wind observations are observed at the same rates —and with a typical cruising speed of 250 ms^{-1} for an aircraft —the spatial resolution of the Mode-S EHS data points is between 1 and 5 km [de Haan, 2016] [Fig. 15b].

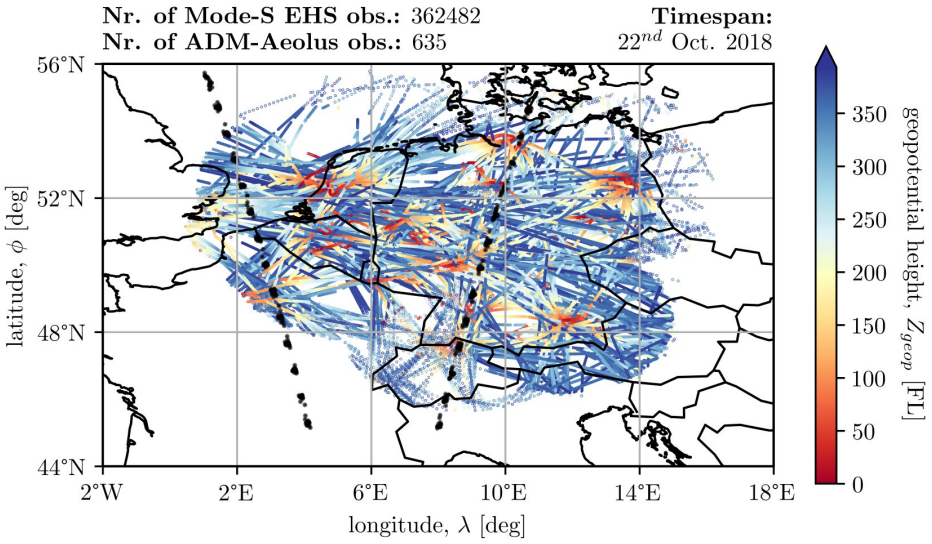

(a) Observations in black indicate the satellite orbit track of Aeolus.

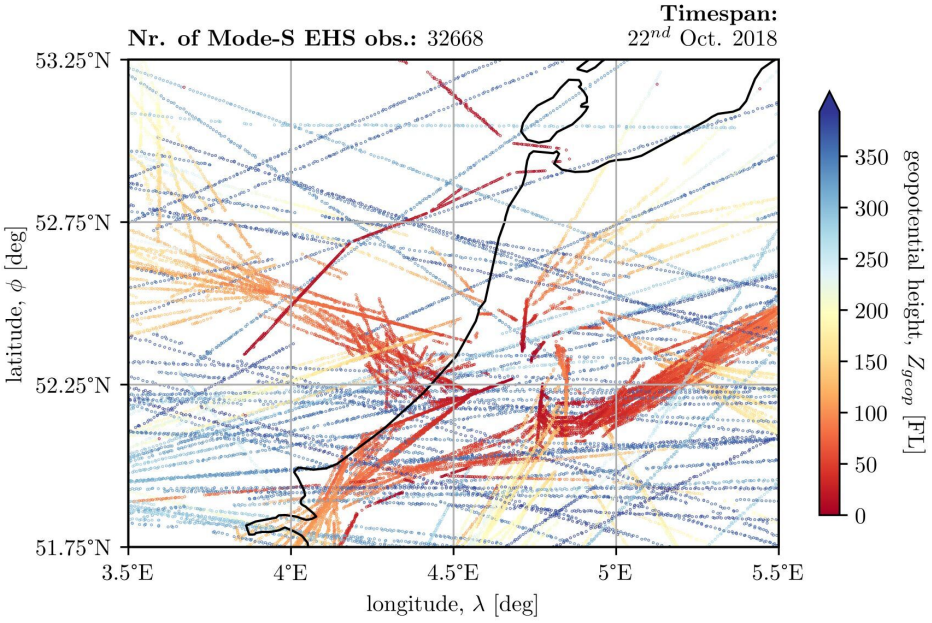

(b) Mode-S EHS data is a quality controlled data set, i.e. some of these data points are *a priori* removed due to quality control requirements —e.g. data points in a turn are removed [see e.g. de Haan, 2011].

Figure 15: Geographical distribution of high-resolution Mode-S EHS observations (a) for the current Mode-S EHS coverage in Europe, and (b) in the vicinity of Amsterdam Airport Schiphol to illustrate the high spatial and temporal resolution. Note that the altitude of the aircraft are expressed in *Flight Level* —calibrated to a reference pressure level of 1013.25 hPa. Conversion from Flight Level (FL) to altitude: FL·100·0.3048 [m].

5 Preprocessing and collocating the data

Merging multiple, independent and uncorrelated observations from e.g. the same geophysical quantity to approximately the same space and time is designated as *collocation* of the observations. This methodology is widely used in validation research to study the correspondence between these observations. The following three independent and uncorrelated data sets are used in this validation research:

- Aeolus L2B product (baseline 2B02[44]),
- ECMWF IFS (CY45R1),
- Mode-S EHS.

Preprocessing the data at first is required before collocating [Sec. 5.1]. As will be discussed in Sec. 5.2, it becomes convenient to perform a conversion of flight levels —used as a vertical reference frame for Mode-S EHS —to atmospheric pressure. Afterwards, data collocation algorithms will be discussed [Sec. 5.3].

5.1 Preprocessing the data

This section will discuss the general preprocessing steps applied to the data sets of Aeolus L2B, Mode-S EHS, and ECMWF IFS respectively.

5.1.1 Creating the first dataframe: `df_Aeolus`

Aeolus L2B baseline 2B02 data is delivered in the *ESA Earth Explorer* binary format[45]. Under ESA contract, the KNMI and the ECMWF developed a conversion tool to convert this format to BUFR format —which is efficient for NWP model data assimilation purposes. Nevertheless, direct use of this format —for validation research in particular —is not possible, in contrast to e.g. the NetCDF[46] or HDF5[47] format. For time being —the KNMI constructed conversion tables to convert the L2B BUFR format to ASCII format. The converted data has been delivered in separate ASCII-files —each file representing approximately one single orbit with a file size in the order of 118 MB. The satellite orbits the Earth with 16 orbits a day, resulting into —on average[48] —16 separate ASCII-files a day and therefore about 1.9 GB of observational data a day.

The disadvantages of ASCII format is its unstructured format —the converted L2B BUFR data is stored as plain text. As the L2B data is reported with use of predefined WMO reference codes [Tab. 4], a Python algorithm has been developed to retrieve the data from the plain ASCII text.

[44] I.e. science and calibration data according to the description of ESA *Aeolus Online data Dissemination System*. This data is only accessible for selected users such as developers and calibration/validation users. See `www.aeolus-ds.eo.esa.int/oads/access/`.

[45] More information, see the *Ground Segment File Format Standard* `PE-TN-ESA-GS-0001` technical note of ESA at `earth.esa.int/documents`.

[46] NetCDF is an abbreviation of *Network Common Data Form*, a data format at which array-oriented data is stored. See `https://www.unidata.ucar.edu/software/netcdf/`

[47] HDF is an acronym for *Hierarchical Data Format*, a data format to store and organize large amounts of data. See `https://www.hdfgroup.org/solutions/hdf5/`

[48] Not all days contained always 16 separate ASCII-files due to e.g. testing activities —as performed by ESA. Recall that Aeolus is an *Earth Explorer* mission, i.e. a demonstration mission.

Atmospheric Laser Doppler Instrument (ALADIN) L2B BUFR data			
WMO code	**parameter**	**unit**	**description**
4001	year	[YYYY]	-
4002	month	[mm]	-
4003	day	[dd]	-
4004	hour	[HH]	-
4005	minute	[MM]	-
4007	seconds	[SS]	-
5069	receiver channel	[-]	Rayleigh or Mie channel.
40036	LIDAR classification type	[-]	Cloudy or clear.
5001	latitude	[deg]	Start, stop and cog.
6001	longitude	[deg]	Start, stop and cog.
4016	time increment	[s]	Start, stop and cog.
7071	height	[m]	Geometric height of observation w.r.t the EGM96 model.
5021	azimuth angle	[deg]	Angle (clockwise from north) of the horizontal projection of the target-to-satellite pointing vector.
7021	elevation angle	[deg]	Elevation of the target-to-satellite pointing vector.
40029	integration length	[m]	Accumulation length of horizontal observations.
40030	horizontal line of sight wind	[m/s]	LOS wind projected on the horizontal as a function of the local elevation angle. Negative when wind blows towards the satellite and positive when wind blows away from satellite.
40031	error estimate	[m/s]	error estimate of the horizontal line-of-sight wind.
25187	confidence flag	[-]	Valid or invalid.
10004	pressure	[Pa]	Interpolated atmospheric pressure from the ECMWF IFS model for the geolocated observation. **Note:** only required for the Rayleigh channel.

Table 4: Retrieved L2B BUFR data utilized to construct `df_Aeolus`. Note that for e.g. latitude and longitude the `start`, `stop` and center of gravity `(cog)` positions are reported, used for ALADIN its averaging principle. In this validation research, only the `cog` values are used.

Once the data is retrieved —organizing and structuring the data is performed such that the data can be accessed for validation research purposes. The *Panda's*[49] Python module is utilized. This module is an open-source *Python Data Analysis Library* and gives rise to construct high-performance structured data sets —designated as *dataframes*. Utilizing the Panda's module, the retrieved Aeolus L2B data are stored in the dataframe (df) `df_Aeolus`. As a first preliminary result, Fig. 16 illustrates a geographical representation of the orbit track of the satellite.

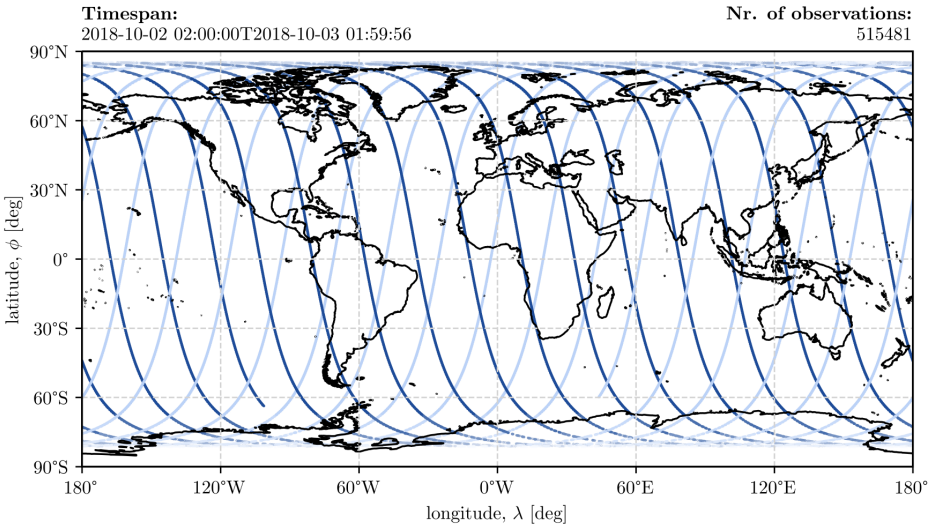

Figure 16: Geographical representation of the Aeolus orbit tracks for one single day. Orbit tracks in dark blue represents the ascending orbit while the descending orbit is colored in light blue.

An important step in preprocessing the data is *quality controlling* the data, which is based on checking the validity of the measurement and the corresponding uncertainty error, designated as the *error estimate*. The latter is based on the SNR response in both channels and accounts for the propagation of errors from the Fabry-Pérot and Fizeau interferometer —assuming *Poisson noise* statistics[50]. The predefined[51] quality control flags applied to `df_Aeolus` are:

- error estimates for the Mie HLOS winds ≥ 3.0 [ms^{-1}] are omitted,
- error estimates for the Rayleigh HLOS winds ≥ 8.0 [ms^{-1}] are omitted,
- HLOS winds with a validity flag of `INVALID` are omitted.

Applying the quality control criteria resulted into a serious reduction in the number of Mie wind observations, while the number of Rayleigh wind observations were more resilient. E.g.,

[49] More information about the *Panda's* Python module: `https://pandas.pydata.org/`.

[50] See the Aeolus Level-2B *Algorithm Theoretical Basis Document* `AE-TN-ECMWF-L2BP-0023` which describes the mathematical description of the Aeolus L2B processor.

[51] These quality control flags are in agreement with ESA and communicated to the teams working on calibration and validation of Aeolus winds.

`AE_OPER_ALD_B_N_2B_20181020T050602_20181020T063638_0002.TXT` —which is an ASCII file representing one orbit of Aeolus data measured on 2018/10/20 between 05:06 and 06:36 UTC —contained 843 observations which reduced to 310 observations. A geographical representation of the geolocated Rayleigh and Mie HLOS wind observations is presented in Fig. 17.

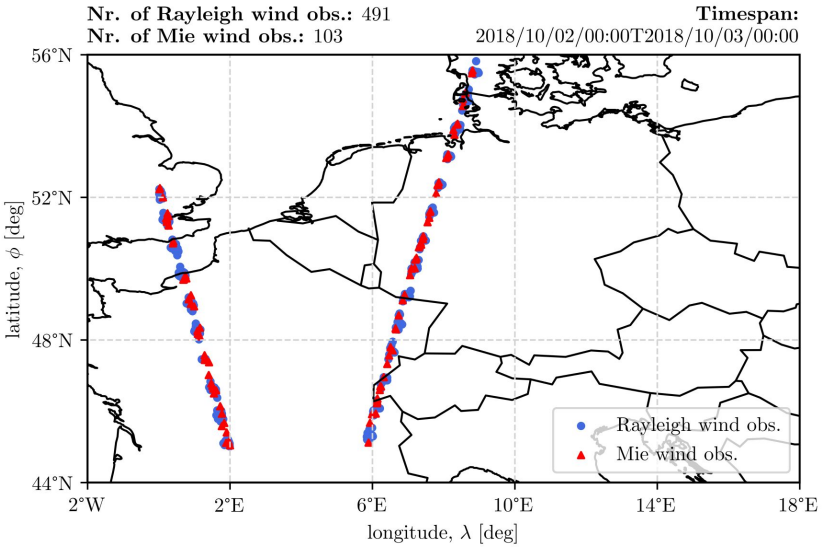

Figure 17: Geolocated HLOS wind observations expressed in [ms^{-1}] at 2018/10/02 after applying the quality control criteria. Illustrated are two orbit phases at which the left track is the ascending orbit while the right track is the descending orbit with geolocated Rayleigh (red) and Mie (blue) wind observations —clustered per wind profile.

To elaborate on the latter figure [Fig. 17], also a cross-section of the descending orbit on the same day is provided [Fig. 18a] with the corresponding error estimates [Fig. 18b].

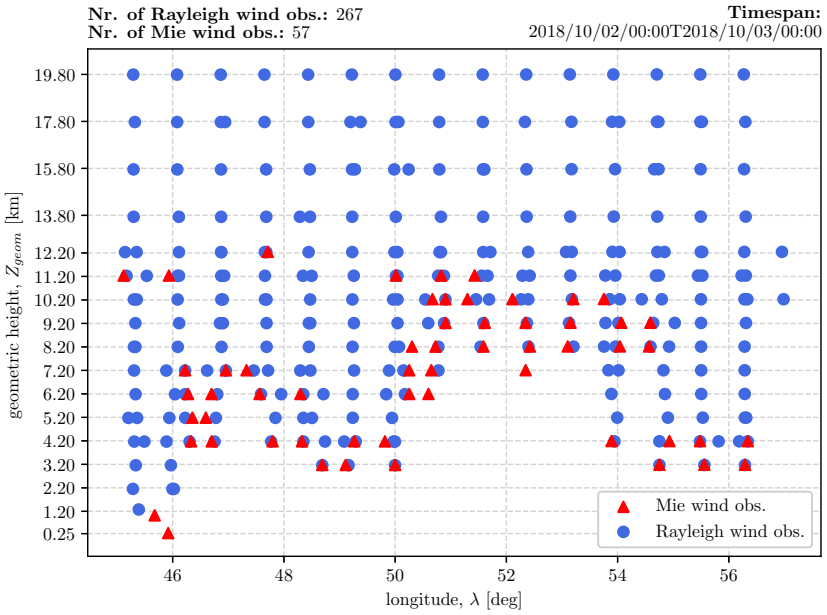

(a) Note that the 355 nm UV laser is not able to penetrate optically thick clouds, resulting into no observations beneath.

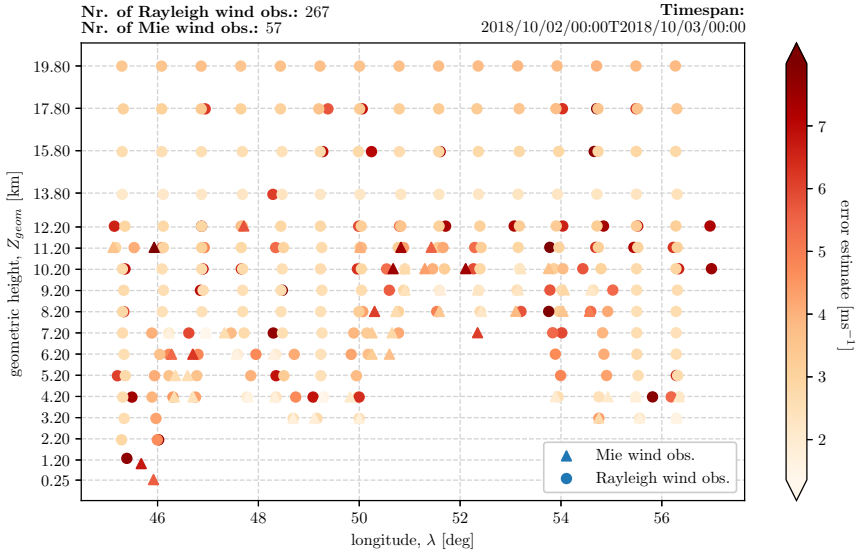

(b) Relative high error estimates near the cloud tops are observed. Possible arguments are related to lower SNR values near these cloud tops or lower SNR values in (strong) convective *casu quo* turbulent situations.

Figure 18: Geolocated HLOS wind observations expressed in [ms^{-1}] at 2018/10/02 after applying the quality control criteria. (a) depicts a cross-section of the descending orbit with (b) the corresponding error estimates, expressed in [ms^{-1}].

As the spatial coverage of the Mode-S EHS data is not globally [Fig. 15a], a Mode-S EHS domain is defined between 45°N to 57°N and 0°E to 17°E. This allows for an additional preprocessing step in which the number of observations per orbit diminished from in the order of ∼30.000 to ∼1.000 observations —a data reduction of about 97%[52]

5.1.2 Creating the second dataframe: `df_ModeS`

The quality controlled[53] aircraft-derived Mode-S EHS data is retrieved internally at the KNMI in separate ASCII-files. The data is distributed and sorted with a time interval of 15 minutes, e.g. `MUAC_20181024_0745.txt` and `MUAC_20181024_0800.txt`, resulting into 96 separate files a day which has in total a size in the order of ∼230 MB. Each separate line within each file represents one single aircraft observation and contains 10 parameters [Tab. 5].

Mode-S EHS ASCII data	
parameter	**unit**
date	[YYYYmmdd]
time	[HHMMSS]
identifier	(unique)
latitude	[deg]
longitude	[deg]
flight level	[100 ft]
wind speed	[kt]
wind direction	[deg]
temperature	[K]
flight phase	[1/-1/0]

Table 5: Retrieved Mode-S EHS data utilized to construct `df_ModeS`, excluding information about the identifier, temperature and flight phase. The flight phase is either ascending (1), descending (-1) or in cruise phase (0)

As the contrast between the number of Mode-S EHS and L2B observations is extreme —preprocessing the Mode-S EHS data is essential to diminish numerical computational timing and memory usage significantly. For each ascending and descending orbit —an *entry time* and an *exit time* is defined when the satellite enters or leaves the predefined Mode-S EHS domain respectively. As the ground velocity V_{ground} of the satellite is in the order of $V_{ground} \approx 7.35$ kms^{-1} —the time to cross the Mode-S EHS domain for the satellite is about 3 minutes. This is only a fraction of a full 24-hour Mode-S EHS data set. Despite the ∼ 3 minutes crossing time —a wide time window of 15 minutes prior the entry time and 15 minutes after the exit time is set to allow for sufficiently Mode-S EHS data for collocation purposes. Therefore approximately 33 minutes of Mode-S EHS data is required to perform collocations per ascending or descending orbit. As the files are stored with an interval of

[52]The order of data reduction is important rather than the actual numbers since they fluctuate due to several reasons, e.g. quality control criteria and the actual number of observations. As aerosols and particles allows for Mie backscattering in the Mie channel —on a clear sky day, few Mie observations are being observed when compared to the abundance of Rayleigh observations.

[53]The data is already preprocessed with necessary corrections such as (a) magnetic to true heading corrections, (b) heading corrections, and (c) airspeed corrections [de Haan, 2011, 2013].

15 minutes —this implies only three Mode-S EHS ASCII-files per ascending or descending orbit rather than 96 files, which is a significant reduction in memory usage.

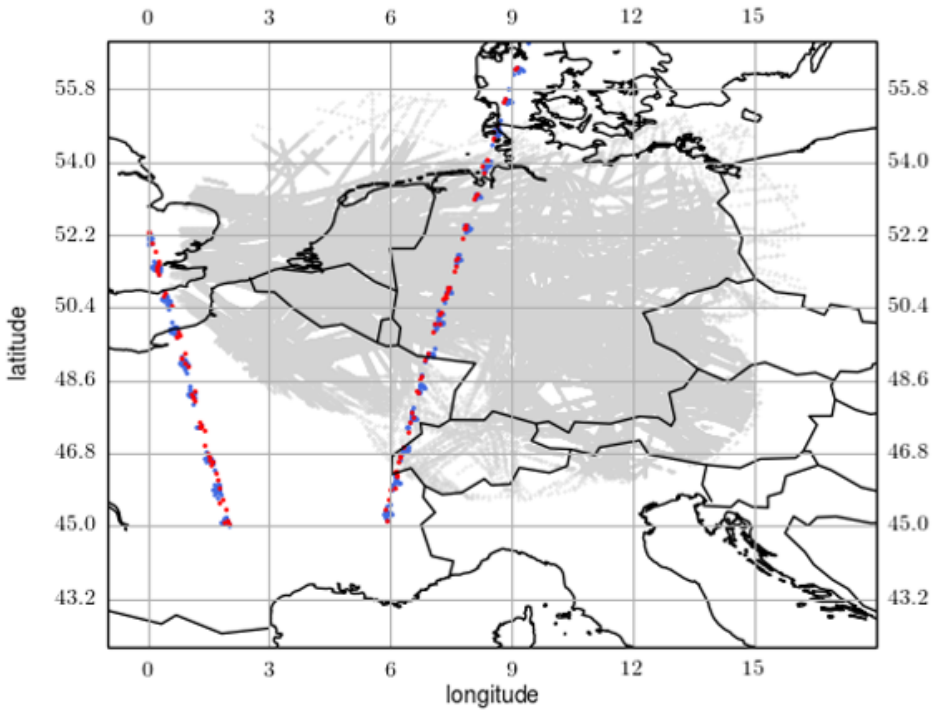

Figure 19: Geographical illustration depicting the contrast between the amount of geolocated Mode-S EHS (grey) and L2B (red) observations. A distinction in the L2B observations is made between HLOS wind observations as measured by the Fabry-Pérot and Fizeau interferometer for the Rayleigh (blue) and Mie (red) channel respectively.

5.1.3 Creating the third dataframe: `df_ECMWF`

The third and final data set to be preprocessed is based on the NWP model of the ECMWF IFS. Initially it was not planned in this validation research to use a third independent data set to validate the L2B wind observations. As elaborated earlier [Sec. 3.2.6], the L2B processor uses *a priori* `AUX_MET` data to correct for the Rayleigh-Brillouin effect. This data set has two major advantages for the validation research:

- **Common vertical reference frame:** Mode-S EHS data is reported in flight levels, i.e. geopotential height Z_{geop}, while L2B is measured w.r.t the geoid, i.e. geometric height Z_{geom}. The former can be converted to atmospheric pressure with use of the *International Standard Atmosphere*[54] model. Since the atmospheric pressure is required to correct the wind observation —as measured by the Fabry-Pérot interferometer in

[54]The International Standard Atmosphere (ISA) is an internationally accepted standard atmosphere model, introduced in 1952 by the ICAO and defined in ICAO Doc. 7488/2. It describes the vertical distribution of atmospheric variables such as pressure, temperature, density and viscosity of the atmosphere in a hypothetical atmospheric model.

the Rayleigh channel —for the Rayleigh-Brillioun effect, the L2B BUFR product includes the atmospheric pressure at the corresponding Z_{geom} of the measurement as well. This information can be used to maintain the same reference frame for both data sets. However —in contrast to the Rayleigh channel —the Mie channel does not require such a correction and therefore the atmospheric pressure at the corresponding Z_{geom} is not reported in the L2B BUFR product[55]. As a result, Mode-S EHS and L2B Mie wind observations are not in the same reference frame. The atmospheric pressure stored in the AUX_MET data can therefore be used to complement for this deficiency.

- **Additional reference data set:** Next to the atmospheric quantity as pressure, the AUX_MET data also provides the u,v-wind velocity components. These wind components can be used to construct the HLOS wind vector and gives rise to a third independent reference data set for validation purposes.

5.1.4 Utilizing the AUX_MET data

The AUX_MET data is distributed as .TAR-files[56]. Unzipping the .TAR-files gives .DBL-files[57]. To access the AUX_MET data, the Common Data Access toolbox (CODA)[58] Python module is utilized. The CODA module is designed to read remote sensing data from Earth observation data files and allows for data formats such as .DBL-files.

Reading the .DBL-files with the CODA module provides off-nadir[59] geolocated information —as date, time and position —and meteorological data. Albeit not required for the L2B BUFR product —the AUX_MET data also includes the ECMWF IFS derived zonal and meridional wind velocity components. These valuable NWP data can be used to construct —in combination with the *a priori* known azimuth angle ψ from the L2B data —the HLOS wind vector $\mathbf{V_{HLOS}}$ [Eq. 14].

The geolocated AUX_MET data is sorted per atmospheric profile —obeying the NWP model of the ECMWF IFS which contains 36.000 vertical profiles with 137 layers per profile. However, the AUX_MET profile numbers are not identical to the ECMWF IFS profile numbers. Moreover, the ECMWF IFS derived AUX_MET data is interpolated to the predicted orbit ground track with geolocations every 3 seconds —i.e. every $\sim$ 20 km along track —according to the Aeolus Level-2B Algorithm Theoretical Basis Document[60] (ATBD). Due to the off-nadir LOS pointing angle of the laser, a range-bin at e.g. 30 km altitude[61] has a misplaced ECMWF IFS derived vertical profile of around 23 km according to the ATBD. However, the NWP model of the ECMWF IFS effectively resolves at a resolution in the

[55] Based on these findings, a proposal is sent to ESA to include the atmospheric pressure information for the Mie channel as well.

[56] TAR is an acronym for *Tape Archive file*, used to merge and store multiple files into one single file. The .TAR-file format is common in Linux operating systems.

[57] DBL is an acronym for *Data Block*, a binary format containing one or multiple data sets.

[58] CODA is designed, developed and maintained by Science [&] Technology Corporation (S[&]T) and primarily funded by ESA. The research and development company S[&]T creates solutions for space, science and defence. More information: http://stcorp.nl/coda/.

[59] I.e. the look angle of ALADIN. Recall that the satellite measures 35° off-nadir on the night side of the Earth.

[60] A document which provides a mathematical description of the Aeolus L2B Processor in ESA its technical note AE-TN-ECMWF-L2BP-0023

[61] Aeolus typically measures up to an altitude of 30 km in the atmosphere, depending on the vertical sampling configurations as described in Sec. 3.2.4.

order of $\sim$ 40 - 80 km and therefore rarely matters as argued by the ATBD. Given that, the geolocation of AUX_MET data is hence not identical to the actual geolocation of the wind observation —required to collocate the AUX_MET and L2B data in order to find the corresponding AUX_MET profile number. Once the profile number is found, an additional step is required in order match the L2B wind observation at a certain geometric height Z_{geom} with the AUX_MET data at approximately the same height. When doing so, the atmospheric pressure —together with the zonal and meridional wind velocity components to construct the HLOS wind vector —can be retrieved.

5.2 Conversion of flight levels into atmospheric pressure

As discussed[62] in Sec. 5.1.3, Mode-S EHS data is reported in flight levels —i.e. pressure altitude which is the height above a standard datum plane for vertical measurement. According to ISA, this standard datum plane is set at 1013.25 hPa. Albeit pressure altitude is reported, the aircraft measures the static pressure which is actually the atmospheric pressure. Hence, once one knows how the measured static pressure is converted to flight levels, it is possible to convert the reported flight levels back to static pressure to get the atmospheric pressure. This section will briefly describe how flight levels can be converted to atmospheric pressure with use of the internationally accepted International Standard Atmosphere (ISA) model as defined by the ICAO.

5.2.1 Derivation for atmospheric pressure

The ISA-model is extensively used in the field of aerospace operations and engineering, and describes the vertical distribution of atmospheric variables such as pressure, temperature, density and viscosity of the atmosphere. The hypothetical atmospheric model assumes a static atmosphere, i.e. that the vertical pressure gradient obeys the hydrostratic balance, which is a relation between the rate of change of pressure with height, z:

$$\frac{\partial p}{\partial z} = -\rho g \tag{15}$$

where p is the pressure, z the height, ρ the air density, and the gravitational acceleration is denoted by g. The *ideal gas law* states that:

$$p = \rho R T \tag{16}$$

with R being the *specific gas constant* for dry air of 287.06 $\text{Jkg}^{-1}\text{K}^{-1}$ and T to denote the temperature. Combining the hydrostatic equation [Eq. 15] with the ideal gas law [Eq. 16] results into a first-order *ordinary-differential equation*:

$$\frac{\partial p}{\partial z} = -\frac{pg}{RT} \tag{17}$$

The troposphere in the ISA-model is defined between $0.0 \leq z < 11.0$ [km] and assumes a constant *environmental lapse rate* Γ, that is:

$$\frac{\partial T}{\partial z} := \Gamma = -6.5°C \quad \text{km}^{-1} \tag{18}$$

[62] Sec. 5.1.3 argued why converting flight levels to atmospheric pressure is beneficial.

Integrating both sides of the latter equation [Eq. 18] —in which the lower limit of integration of the left integrand is a reference temperature T_0 at which the initial condition $T_0 = T(z = z_0)$ is applied with $T_0 \equiv 288.15°K$ according to the ISA-model, while the upper limit of integration is the temperature at a certain height of interest $T(z = z_{atm})$ —gives:

$$\int_{T(z=z_0)}^{T(z=z_{atm})} \partial T = \int_{z=z_0}^{z=z_{atm}} \Gamma \partial z \tag{19}$$

Evaluating both sides of the expression such that an expression for the linearized temperature profile can be expressed as:

$$\therefore \quad T_{atm} = T_0 + \Gamma(z_{atm} - z_0) \quad \text{for } 0.0 \leq z < 11.0 \text{ [km]}. \tag{20}$$

Equation [17] can be expressed in terms of the derived linearized temperature profile. *Separation of variables* of equation [17] and substituting equation [20] for the environmental lapse rate Γ gives:

$$\frac{1}{p}\partial p = -g\frac{1}{R[T_0 + \Gamma(z_{atm} - z_0)]}\partial z \tag{21}$$

Integrating the left integrand of the latter expression —in which the lower limit of integration is a reference pressure p_0 when applying the initial condition $p_0 = p(z = z_0)$ with $p_0 \equiv 1013.25$ hPa, and the upper limit of integration is the pressure at a certain height —provides:

$$\int_{p(z=z_0)}^{p(z=z_{atm})} \frac{1}{p}\partial p = -\frac{g}{R}\int_{z=z_0}^{z=z_{atm}} \frac{1}{T_0 + \Gamma z}\partial z \tag{22}$$

where $T_0 + \Gamma z(z_0) = T_0$ since $z(z_0) = 0$. The gravitational acceleration is assumed to be constant according to the ISA-model with $g \equiv 9.80665$ ms^{-2}. Together with the specific gas constant R, both quantities can be moved outside the integral. Evaluating both sides results into:

$$\ln\left(\frac{p_{atm}}{p_0}\right) = -\frac{g}{R\Gamma}\ln\left(\frac{T_0 + \Gamma z}{T_0}\right) \tag{23}$$

such that an expression for the atmospheric pressure becomes:

$$\therefore \quad p_{atm} \quad = \quad p_0\left[1 + \Gamma\left(\frac{h}{T_0}\right)\right]^{-g/R\Gamma} \qquad \text{for } 0.0 \leq Z_{geom} < 11.0 \text{ [km]}. \tag{24}$$

In contrary to the troposphere —the tropopause of the ISA-model assumes an isothermal layer with a zero lapse-rate, i.e. $\Gamma := \partial T/\partial z \equiv 0$. As a result, equation [24] does not hold for this part of the atmosphere and requires a modification to avoid a trivial expression for p_{atm}.

Reintroducing equation [17], separating the variables, and integrating both sides yields:

$$\int_{p_0(z_0)}^{p(z_{atm})} \partial p = -\int_{z_0}^{z_{atm}} \frac{g}{RT} p \partial z \tag{25}$$

Evaluating both sides:

$$\ln\left(\frac{p(z_{atm})}{p_0(z_0)}\right) \quad = \quad -\frac{g}{RT}(z_{atm} - z_0) \tag{26}$$

This solution is referred to as the *hypsometric equation* and assumes an isothermal layer with a zero lapse-rate. As a result, this equation is therefore convenient for the tropopause of the ISA-model. Solving equation [26] for the atmospheric pressure at a certain height of interest provides:

$$\therefore \quad p(z_{atm}) \quad = \quad p_0(z_0)\exp\left[-\frac{g}{RT}(z_{atm} - z_0)\right] \quad \text{for } Z_{geom} \geq 11.0 \text{ [km]}. \tag{27}$$

in which $z_0 = 11$ km, i.e. the transition from the troposphere to tropopause according[63] to the ISA-model.

5.3 Data collocation algorithm

Collocation is a process in which multiple, independent and uncorrelated observations from e.g. the same (geo)physical quantity are merged to approximately the same geolocation —i.e. approximately at the same date, time and space. In this validation research, the following independent and uncorrelated preprocessed data frames are used to collocate:

- `df_Aeolus`
- `df_ModeS`
- `df_ECMWF`

in which the common geophysical quantity to be collocated is the HLOS wind observation.

5.3.1 Defining the collocation box

The principle of collocation is based on defining a predefined imaginary domain around each L2B observation from `df_Aeolus` and take into account all Mode-S EHS and ECMWF IFS data from `df_ModeS` and `df_ECMWF` respectively inside this domain into account. Once done, the collocated wind observations can be compared.

At first the imaginary domain —hereafter *collocation box* —around each single L2B point has to be defined. The collocation box is spatially spanned in the vertical by a certain height increment *dZ* —above and below each individual geolocated L2B observation point —and horizontally spanned by a certain radius. Temporally the collocation box is spanned by a predefined time increment *dt* to define the collocation time-window. Rather determining the *Euclidean* distances between all Mode-S EHS observations points and the L2B observation points, the great-circle distance is used in order to take the curvature of the Earth into account. This great-circle distance is determined by calculating the *haversine* distance [Fig. 20].

[63] In dynamical meteorology, the transition from troposphere to tropopause is defined as 2PVU rather than a certain height.

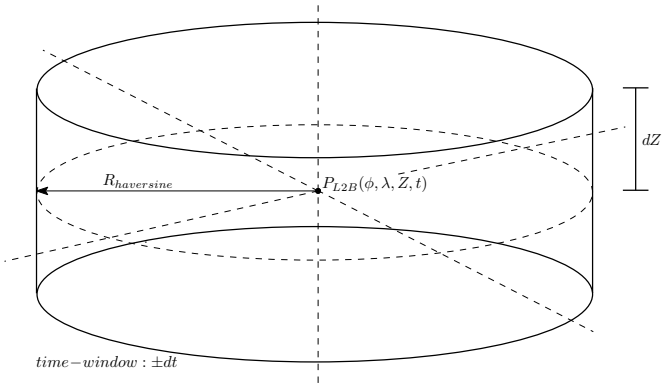

Figure 20: Schematic representation of a four-dimensional collocation box for an arbitrary geolocated L2B observation point $P_{L2B}(\phi, \lambda, Z, t)$ with a haversine radius $R_{haversine}$ and increments dZ and dt for the height and time-window respectively. Note that the height can either be expressed as a geometric or geopotential height.

Assume an arbitrary geolocated L2B observation point $(\phi, \lambda)_{L2B}$ at latitude ϕ and longitude λ. Additionally, denote an arbitrary geolocated Mode-S EHS observation point within the corresponding collocation box of $(\phi, \lambda)_{L2B}$ as $(\phi, \lambda)_{EHS}$. Then for each $(\phi, \lambda)_{EHS}$ within the collocation box the great-circle distance from that point to $(\phi, \lambda)_{L2B}$ is determined by calculating the haversine distance —defined as:

$$d_{hav.} := 2r \arccos(\sqrt{h}) \tag{28}$$

where $r \sim 6371$ km is the radius of the Earth and h is obtained from the latitude ϕ and longitude λ of both points:

$$h = \text{hav}(d\phi) + \cos(\phi_{L2B}) \cdot \cos(\phi_{EHS}) \cdot \text{hav}(d\lambda). \tag{29}$$

The *haversine functions* in the latter expressions are defined as:

$$\text{hav}(d\phi) := \sin^2\left(\frac{d\phi}{2}\right), \quad \text{hav}(d\lambda) := \sin^2\left(\frac{d\lambda}{2}\right) \tag{30}$$

where the increments $d\phi$ and $d\lambda$ are equivalent to $|\phi_{EHS} - \phi_{L2B}|$ and $|\lambda_{EHS} - \lambda_{L2B}|$ respectively. Note that all positions have to be expressed in radians.

5.3.2 Circular collocation box versus rectangular box

Prior to the circular collocated box method, a more simplistic rectangular shaped collocation box was taken, that is:

$$(\phi, \lambda, Z, t)_{L2B} \pm d\phi, \quad (\phi, \lambda, Z, t)_{L2B} \pm d\lambda \tag{31}$$

to span the collocation box spatially in the zonal and meridional direction respectively, and

$$(\phi, \lambda, Z, t)_{L2B} \pm dZ \tag{32}$$

to span the collocation box spatially in the vertical direction.

As long as one is consistent —i.e. the volume for the spanned rectangular collocation box is approximately equal to the volume when using the radius based collocation box —no obvious significant changes are found in the number of collocations or number of Mode-S EHS observations in each collocation box, nor in the statistics [Fig. 21]. Nevertheless, the disadvantage of the rectangular based collocation box is the skewness of the box due to the converging meridians when moving towards the poles[64]. To counteract, a radius-based collocation box resolves this issue.

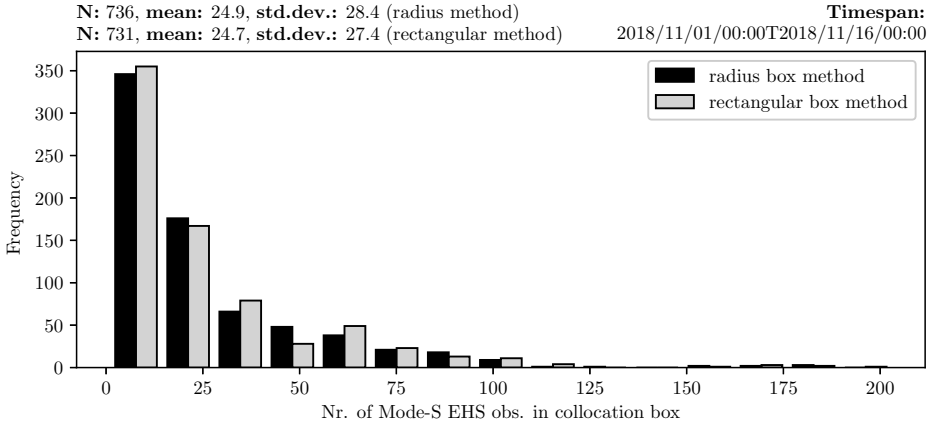

Figure 21: Rectangular box method versus radius based box method. For the rectangular box numerical values of $d\phi, d\lambda = 0.5$ [deg.] are taken, while for the radius-based box a numerical value of $R_{haversine} = 50$ km is taken. Both obey the same numerical value for dZ and dt resulting in approximately an equal volume for both boxes. Collocation runs have been performed over a timespan of about 16 days between 0 - 12 km.

5.3.3 Conversion of the wind observation

In contrary to `df_Aeolus` —`df_ModeS` and `df_ECMWF` do not include the HLOS wind observation directly but indirectly. For `df_ECMWF`, Sec. 5.1.3 demonstrated that the HLOS wind vector can be constructed with the u,v-wind velocity components when utilizing the `AUX_MET` data. Slightly similar approach is applied for `df_ModeS` to construct the HLOS wind vector.

Assume once more an arbitrary geolocated Aeolus L2B observation point $(\phi, \lambda)_{L2B,i}$ with azimuth angle ψ_i. All Mode-S EHS observation points within the corresponding collocation box are converted to the same wind geometry by decomposing the Mode-S EHS wind vector into the zonal and meridional velocity components in order to construct the HLOS wind vector. Denoting averages by the brackets $\langle\rangle$ and the *a priori* known L2B azimuth angle as ψ_i, and by recalling the definition the HLOS wind vector [Eq. 14] —the HLOS wind vector for Mode-S EHS is then obtained by:

$$\therefore \quad \mathbf{V}_{HLOS,ModeS} = -\langle u(x)\rangle \sin\psi_i - \langle v(y)\rangle \cos\psi_i \tag{33}$$

[64]The lower boundary of the Mode-S EHS domain is set at 42°N and a $d\lambda = 1$ equals about 82 km, while the upper boundary of the domain is at 57°N resulting into a $d\lambda = 1$ to be equal to about 60 km.

Albeit taking the arithmetic mean, a more profound averaging method is applied instead which is based on a weighted mean to diminish for so-called *representativeness errors*[65]. As for a first-order estimate in increasing the accuracy in the collocation algorithm, the *inverse-distance weighting* method as weighted mean is applied.

5.3.4 Inverse Distance Weighting spatial interpolation

The *inverse distance weighting* [Shepard, 1968] method is in this study utilized for spatial interpolation of Mode-S EHS observations to a certain L2B observation point. The concept of the IDW method relies on the assumption that observations within a certain search neighborhood closer to a certain reference points gets a higher weight than observations further away. In contrary to the *arithmetic mean* in which all observations have equal weights.

The inverse distance weighting (IDW) interpolation is approximated by:

$$Z^*(\mathbf{u}) \approx \sum_{i=1}^{N} \lambda_i Z(\mathbf{u}_i) \tag{34}$$

where $\mathbf{u}$ is the reference location of the geolocated L2B observation point while $\mathbf{u}_i, i = 1, .., N$ are the geolocated Mode-S EHS observations within a certain search neighborhood for N Mode-S EHS observations within this search domain. This search domain is the collocation box around each single geolocated L2B observation point $\mathbf{u}$. The weights assigned to each $\mathbf{u}_i$ are determined with:

$$\lambda_i = \frac{d_i^{-\zeta}}{\sum_{i=1}^{N} d_i^{-\zeta}} \quad \text{for } i, .., N \tag{35}$$

In order to take the curvature of the Earth into account —the *Haversine distance* is taken for d_i between $\mathbf{u}$ and $\mathbf{u}_i$ rather than taking the common *Euclidian distance*. The exponent ζ is the *distance exponent power* and influences the assigned weights. According to theory, increasing ζ results in increasing the weights for the observations closer to the reference while the weights for the observations further away decreases [see e.g. Diodato and Ceccarelli, 2005]. Note that the sum of the inverse distance weights is unity, that is:

$$\sum_{i=1}^{N} \lambda_i \equiv 1 \tag{36}$$

Any value for the distance exponent power ζ can be chosen in order to tune the IDW interpolator and hence the interpolation results. Note that $\lambda_i \equiv 1 \; \forall i$ when $\zeta = 0$, i.e. all observations are equally weighted with a weight of 1 and the IDW interpolator becomes simply the arithmetic mean.

After the intermezzo elaborating on the IDW method, a redefinition of Eq. 33 —and therefore the algorithm to convert Mode-S EHS wind vectors to HLOS wind vectors —becomes:

[65] Mode-S EHS points further away from $(\phi, \lambda)_{L2B,i}$ represent another part of the atmospheric and hence atmospheric wind conditions than the actual atmosphere at $(\phi, \lambda)_{L2B,i}$. Especially in non-homogeneous situations such as turbulent situations or in frontal zones, this might introduce significant representativeness errors which biases the validation results and can be one of the possible reasons of the occurrence of outliers in e.g. a scatterplot.

- construct for each individual Mode-S EHS observation the HLOS wind vector with use of the u,v-wind velocity components and the *a priori* known azimuth angle ψ_i of $(\phi, \lambda)_{L2B,i}$,
- determine for all Mode-S EHS observation points the haversine distance w.r.t $(\phi, \lambda)_{L2B,i}$,
- apply the IDW method to determine the spatial interpolated HLOS wind vector,

as a result the wind vectors from both data sets are homogenized, i.e. converted into the same measurement geometry.

Recall that any value for the distance exponent power ζ can be chosen as a tuning parameter for the IDW interpolator [Eq. 34]. As an initial guess, a numerical value of $\zeta = 1$ is taken. Several collocation runs have been performed for $\zeta = 0, 1, 2, 5$ and 10 to justify and validate this initial guess. Fig. 22 demonstrates the results of these collocation runs for a small time-window within the complete collocation time span of 2018/10/02 to 2018/10/09. The results demonstrate no significant differences when performing an intercomparison study in terms of the *Pearson's correlation coefficient* ρ and the *root mean squared error*. The former is a measure of linearity between both data sets in which $\rho = 0.924$ for $\zeta = 1$ implies a correspondence of about 92.4%. The root mean squared error is a measure of the variance in the prediction errors between both data sets. Note, formal mathematical definitions of the aforementioned statistical metrics will be given in Sec. 6. Both statistical metrics show a steady behaviour which confirms the initial guess of $\zeta = 1$ to be satisfying.

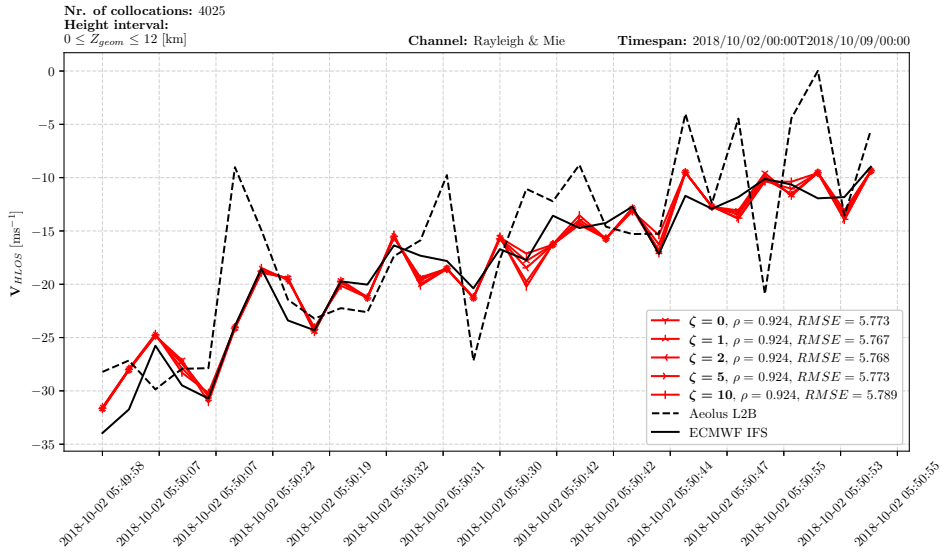

Figure 22: Consecutive collocated HLOS wind results derived from multiple independent collocation runs with different numerical values for the distance exponent power ζ. Collocations have been performed for $\zeta = 0, 1, 2, 5$ and 10. The figure shows the consecutive collocated HLOS winds for ECMWF IFS (black solid line), L2B (black dashed line) and Mode-S EHS (red) for $0 \leq Z_{geom} \leq 12$ km —hence its volatility and therefore not an actual time-series of the evolution of the HLOS wind —for the Rayleigh and Mie channel.

To conclude this section —recall that for $\zeta = 0$ the IDW interpolation simply becomes an arithmetic mean and the results reveal no significant different between the IDW method or the arithmetic mean method. Further research is required. Nevertheless, the IDW method with $\zeta = 1$ is maintained in continuation of this study.

6 Validation results

Before elaborating on the validation research, common and important validation metrics will be briefly discussed [Sec. 6.1]. Furthermore, research is performed in defining parameters to span the collocation box temporally and spatially and will be presented at hereafter [Sec. 6.2]. After that, the collocation results will be presented in detail [Sec. 6.3]. Additionally, a profound study is performed in estimating the wind observation error of the L2B observations using the *triple collocation* method [Stoffelen, 1998] [Sec. 6.4].

6.1 Validation metrics

For data quality control purposes, several statistical validation *metrics* will be introduced. These metrics will be introduced since they will be used extensively in the upcoming sections.

6.1.1 Bias

Assume two independent data sets with equal length N in which one is the reference data set x_{ref} and the other data set is the observed data set x_{obs}, then the *bias* of x_{obs} is defined as the mean difference between these two data sets:

$$bias := \frac{1}{N}\sum_{i=1}^{N}(x_{ref,i} - x_{obs,i}) = \overline{x}_{ref} - \overline{x}_{obs} \tag{37}$$

in which $x_{ref,i}$ represents Mode-S EHS or ECMWF IFS, $x_{obs,i}$ is L2B, and $\overline{()}$ the mean. A negative bias indicates that the observation is overestimating the reference data, while underestimation is denoted by a positive bias. A distinction will be made between the bias in the HLOS wind observations measured in the Rayleigh channel or in the Mie channel.

6.1.2 Standard deviation

Given an arbitrary data set A of length N, then its *standard deviation* is defined as the square root of its *variance*:

$$\sigma_A := \sqrt{\frac{1}{N}\sum_{i=1}^{N}(A_i - \overline{A})^2} \tag{38}$$

Rather determining the standard deviation (or variance) of the data set itself, it is more common in NWP statistical analysis to produce statistics of residuals. I.e., the standard deviation of the L2B data in the distribution of its residuals D_i, where $D_i := x_{ref,i} - x_{obs,i}$. Redefining the previous standard deviation [Eq. 38]:

$$\sigma_{ref-obs} := \sqrt{\frac{1}{N}\sum_{i=1}^{N}(D_i - \overline{D})^2} \tag{39}$$

The latter expression is informative when performing intercomparison studies between data sets —i.e. between Mode-S EHS, L2B and ECMWF IFS. Also for $\sigma_{ref-obs}$ —a distinction will be made between the standard deviation for the Rayleigh and Mie channel.

6.1.3 Median absolute deviation

The *median absolute deviation* is a robust measure of the variability in the data set. It is —in contrast to the standard deviation —more robust since it is less sensitive for e.g. outliers in the data set.

Given an arbitrary data set A of length N, then the median absolute deviation (MAD) is defined as:

$$MAD := median(|A_i - \tilde{A}|) \quad \text{for } i, .., N. \tag{40}$$

where $\tilde{A} = median(A)$. The MAD can be used as a *consistent estimator* $\tilde{\sigma}_A$ for the standard deviation σ_A, that is:

$$\tilde{\sigma}_A = \kappa \cdot MAD \tag{41}$$

where κ is a constant scaling factor and depends on the probability distribution of the data set of interest —for a Gaussian distributed data set, $\kappa \approx 1.4826$. When multiplying the MAD with this scaling factor, the scaled MAD converges in probability to the true standard deviation. A constant scaling factor of $\kappa = 1.4826$ can be taken as it is *a priori* expected that the ECMWF IFS, L2B and Mode-S EHS collocated data sets will demonstrate a Gaussian distribution.

6.1.4 Root mean squared error

To further quantify differences in two data sets, the 'total error' is designated as the *root mean squared error* and can be decomposed into two components:

$$\begin{aligned} RMSE^2 &:= variance + bias^2 \\ &:= \sigma^2 + bias^2. \end{aligned} \tag{42}$$

Depending on the research focus, sometimes it can be more convenient[66] to express the individual components rather than the RMSE.

6.1.5 Pearson's correlation coefficient

A common quality control statistical metric used as a measure of linear dependency between two independent data sets is the *Pearson's correlation coefficient*[67], denoted by the symbol ρ, expressed as:

[66] Especially in calibration and validation studies, one can be more interested in the individual components rather than the full component. The former gives more information about how the total error is composed.

[67] Next to Pearson's correlation coefficient, there are multiple correlation coefficients such as the *Kendalls Tau* and *Spearman's Rank* correlation coefficient. They differ in how they treat outliers in the data set. In contrast to the other coefficients, the Pearson's correlation coefficient assumes *a priori* that both data sets are monotonic and linear. It is expected that the L2B data and Mode-S EHS data obey this criteria which reinforce the decision for the use of the Pearson's correlation coefficient.

$$\rho := \frac{\sum_{i=1}^{N}(x_{ref,i} - \overline{x}_{ref})(y_{obs,i} - \overline{y}_{obs})}{\sqrt{\sum_{i=1}^{N}(x_{ref,i} - \overline{x}_{ref})^2}\sqrt{\sum_{i=1}^{N}(y_{obs,i} - \overline{y}_{obs})^2}}, \quad \rho \in [-1, 1]. \tag{43}$$

The numerator is the *covariance* between the reference and observed data sets, while the denominator is the product of the standard deviation of both data sets. For an exact linear relationship between both data sets, $\rho \equiv 1$ such that:

$$(x_{ref,i} - \overline{x}_{ref}) = \kappa(y_{obs,i} - \overline{y}_{obs}) \quad \forall i, \text{ where } \kappa > 0, \tag{44}$$

and its said that both data sets are *perfectly* positive correlated. In contrary for $\kappa < 0$, the reverse happens. Hence, the numerical value for ρ determines whether two data sets are negative or positive correlated. Negative correlation ($\rho < 0$) implies a negative linear dependency between two data sets. Vice verse, a positive correlation ($\rho > 0$) implies a positive linear dependency.

6.2 Defining the collocation box parameters with Taylor-diagrams

A priori it is not evident which numerical value for the parameters dZ, dt and R has to be chosen for the imaginary collocation box around each geolocated L2B observation point $P_{L2B}(\phi, \lambda, Z, t)$. To diminish arbitrarily chosen parameters, it is worthwhile to postulate that a distinction has to be made between both channels and at different atmospheric layers.

Mode-S EHS data is temporally and spatially significantly more abundant at higher levels in contrast to lower levels in which Mode-S EHS data becomes more clustered near the vicinity of airports [Fig. 23]. Increasing the collocation box spatially and temporally to increase the number of collocations at lower levels increases representation errors.

Since molecules in the atmosphere are more abundant than aerosols and particles, the number of Rayleigh observations is more pronounced than Mie observations. This contrast is depicted in Fig. 24. The same aforementioned argument for increasing the collocation box spatially and temporally can be applied in order to increase the number of Mie observations, but this influences the statistical errors as well. Making a distinction between both channels is therefore worthwhile as well.

In order to simulate different collocation parameters under different conditions, a *Taylor-diagram* is used to analyze the results. On a Taylor-diagram [Taylor, 2001], two data sets are tested for correspondence in terms of statistical metrics such as the Pearson's correlation coefficient, the root mean squared error between the two data sets, and the ratio of the standard deviations of the two data sets. The results are plotted as a single point on a two-dimensional plot and provides a graphical summary of the statistical performance of the corresponding collocation runs. Multiple collocation runs can be performed, resulting into $n + 1$ points on the Taylor-diagram for n collocation runs with different collocation parameters.

First a short introduction about the methodology to construct the Taylor-diagram and the theoretical background of the Taylor-diagram will be given. Afterwards the results of the determined collocation box parameters will be discussed.

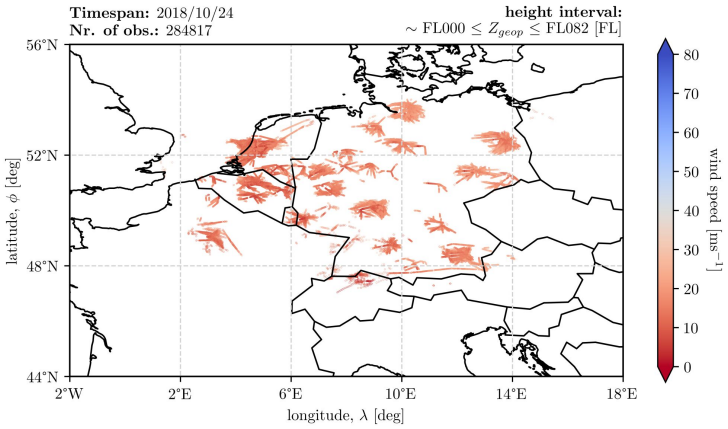

(a)

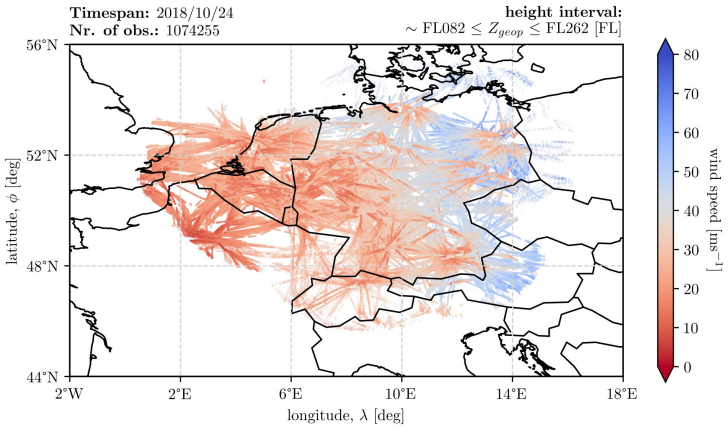

(b)

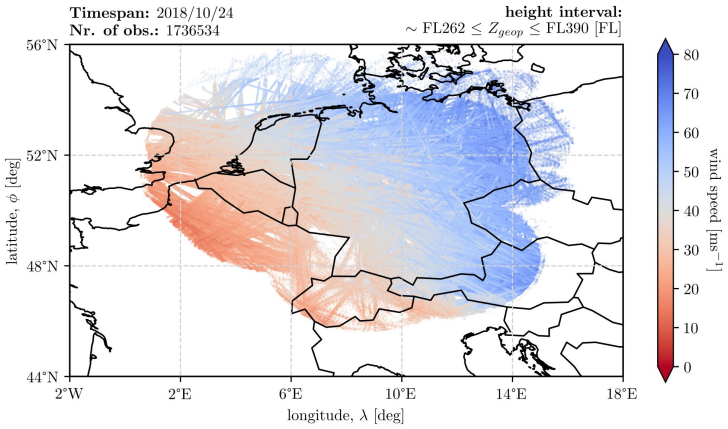

(c)

Figure 23: Geographical illustration of spatial and temporal distributed Mode-S EHS data on a single day between (a) $0.0 \leq Z_{geom} \leq 2.5$ km, (b) $2.5 \leq Z_{geom} \leq 8.0$ km, and (c) $8.0 \leq Z_{geom} \leq 12.0$ km. At lower altitudes the data is more clustered in the vicinity of airports, while at higher altitudes the data is significantly more distributed.

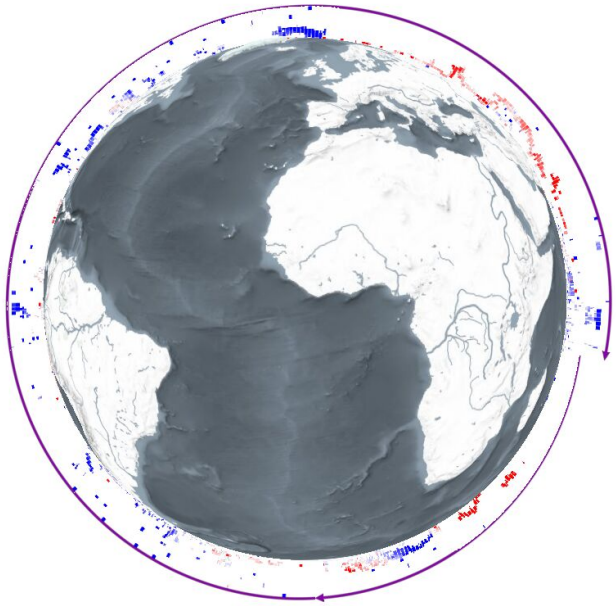

(a) Mie observations due to backscattering of aerosols and particles. As a result, most of the Mie observations are observed in the lower part of the atmosphere *casu quo* in the PBL.

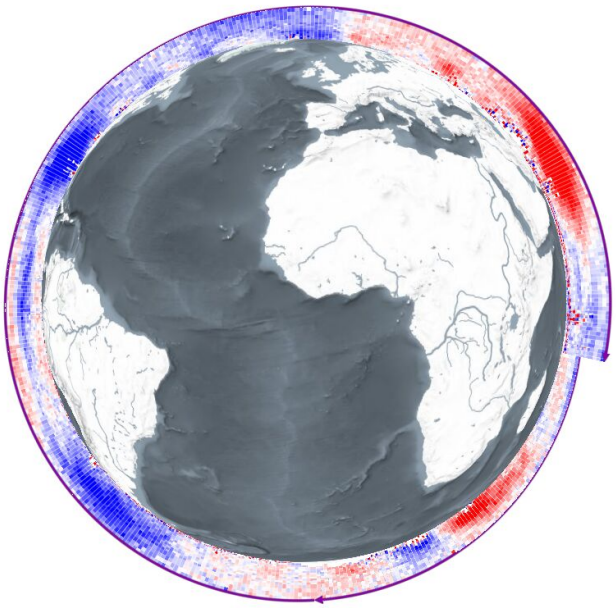

(b) Note the clearly visible sub-tropical easterly jet stream in the northern hemisphere.

Figure 24: Geographical illustration demonstrating the contrast between (a) the sparse number of Mie observations when compared to (b) the abundance of Rayleigh observations for one orbit on 2019/02/18. Observations in red are negative HLOS values while positive values are indicated in blue. Image created with ESA ViRES-tool (info: `https://aeolus.services/`). *Courtesy to:* de Kloe, J., 2019.

6.2.1 Methodology to construct the Taylor-diagram

Encountering for the aforementioned arguments —the atmosphere is discretized in three vertical layers in order to make a rough distinction between the mean[68] atmospheric boundary layer, the free-atmosphere and the upper-atmosphere [Tab. 6]. In each discrete layer, separate collocation runs have been performed with a different combination for the collocation box parameters dZ, dt and R.

atm. layer [km]	**height increment,** dZ **[m]**	**time-window,** dt **[min.]**	**radius,** R **[km]**
$0.0 \leq Z_{geom} < 2.5$	[250, 500, 1000]	[2.5, 5.0, 10.0]	[50, 100, 150]
$2.5 \leq Z_{geom} < 8.0$	[250, 500, 1000]	[2.5, 5.0, 10.0]	[50, 100, 150]
$8.0 \leq Z_{geom} < 12.0$	[250, 500, 1000]	[2.5, 5.0, 10.0]	[50, 100, 150]

Table 6: Predefined numerical values for the collocation parameters per discrete atmospheric layer for both channels used to construct the Taylor-diagram.

This creates 27 individual collocation runs per discrete atmospheric layer and hence 81 runs in total. Furthermore, a distinction is made between the Rayleigh and Mie channel, resulting in a total of 162 individual runs. The collocation time span for each single collocation run is from 2018/09/03 to 2018/12/17. After a computational cost in the order of ~ 7 days in total, all 162 results are stored in separate *HDF5*-files in order to access them on demand and to create the Taylor-diagrams.

6.2.2 Theoretical background of the Taylor-diagram

The Taylor-diagram uses the standard deviation σ, Pearson's correlation coefficient ρ, the bias $\overline{E}$ and the root mean squared difference E. Following Taylor [2001], the root mean squared difference E can be decomposed into two components. The first component is defined as:

$$E' \equiv \sqrt{\frac{1}{N}\sum_{n=1}^{N}[(x_{ref,n} - \overline{x}_{ref}) - (x_{obs,n} - \overline{x}_{obs})]^2} \tag{45}$$

which is the *unbiased* variant of E and referred to as the *centered* root mean squared difference E' (CRMSD). The second component is defined as:

$$\overline{E} = \overline{x}_{ref} - \overline{x}_{obs} \tag{46}$$

and expressed the overall bias. Quadratically addition of these two components yields the full mean squared difference —a similar expression as Eq. 42:

[68] Reanalysis data such as ERA-5 from ECMWF can be used to approximate the climatological boundary layer height for a certain timespan of interest. Nevertheless, this approach is omitted in this study. Since the number of L2B observations in the atmospheric boundary layer is sparse (given that e.g. ALADIN cannot penetrate trough optically thick clouds, or due to reported winds classified as `invalid`) and sorted per predefined range-bin in the vertical in the L2Bp, one does not want to omit valuable observations which where reported slightly above this approximated mean boundary layer.

$$E^2 = E'^2 + \overline{E}^2 \tag{47}$$

The correspondence between two data sets are quantified by statistical metrics such as the correlation coefficient and the root mean squared difference. Nevertheless, according to Taylor [2001] the standard deviation of both data sets are also required for a more complete characterization of the data sets. As a result, the statistical metrics ρ, E', σ_{ref} and σ_{obs} together provides a more profound understanding of the correspondence between two data sets and hence useful to study patterns, variances and the performance of n different collocation runs.

The geometric relation between the aforementioned metrics can be expressed as:

$$\therefore \quad E'^2 \equiv \sigma_{ref}^2 + \sigma_{obs}^2 - 2\sigma_{ref}\sigma_{obs}\rho \tag{48}$$

and can be interpreted in terms of the *law of cosines*:

$$c^2 \equiv a^2 + b^2 - 2ab\cos\phi \tag{49}$$

where $a = \sigma_{ref}, b = \sigma_{obs}$ and $c = E'$ are the lengths of the sides of the hypothetical triangle with ϕ being the angle between a and b [Fig. 25]. With this geometric relationship [48], it is possible to construct a Taylor-diagram which statistically quantifies the degree of similarity between the observed data set x_{obs} and the reference data set x_{ref}. The radial distance from the origin p_{origin} is proportional to the standard deviation σ_{obs}, the centered root mean squared difference E' between both data sets is proportional to the distance from p_{ref} to p_{obs} and expressed in the same units as the standard deviation. The linear dependency between the data sets is expressed by the Pearson's correlation coefficient ρ and is given by the angle between σ_{obs} and σ_{ref}, i.e. the azimuthal position of p_{obs}.

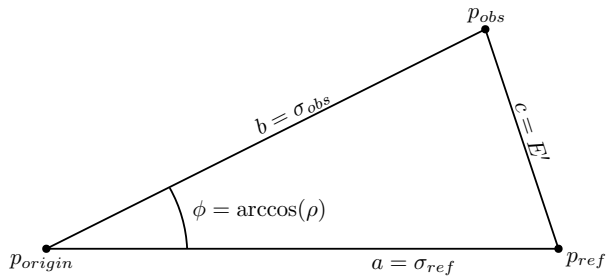

Figure 25: Hypothetical triangle showing the geometric relationship between the statistical metrics ρ, E', σ_{ref} and σ_{obs} described by Eq. 48 and Eq. 49. The performance of n collocation runs compared to a certain reference is quantified by a Taylor-diagram and will plot $n+1$ points and n hypothetical triangles.

6.2.3 Taylor-diagram results

In this section the Taylor-diagrams are used to analyze how each single collocation run, represented as a coloured marker in the Taylor-diagram, performs. Each Taylor-diagram shows 27 collocation runs, representing one of the 27 combinations for dh, dt and R. Since for this study the atmosphere is discretized into three separate layers and the distinction

between the Rayleigh and Mie channel, a total of 6 Taylor-diagrams are produced.

The position of each marker shows how well the corresponding collocation run matches with the reference. The reference σ_{ref} is Mode-S EHS and denoted by the black square in each Taylor-diagram, while σ_{obs} is the standard deviation between L2B and Mode-S EHS [Eq. 39] rather than —as discussed in Sec. 6.1.2 —the standard deviation of the L2B data set it self. Furthermore, the black square is positioned on the x-axis since $\rho \equiv 1$ for the reference data set.

There are 27 individual runs to be compared with the Mode-S EHS as reference. The Taylor-diagram therefore requires a fixed reference with a fixed value for σ_{ref}. According to literature, de Haan [2016] demonstrated an error estimate of the wind component in the order of 1.4 $\pm$ 0.1 ms^{-1} for each single Mode-S EHS observation point. However, $\sigma_{ref} \neq$ 1.4 ms^{-1} since each individual collocation box has N number of Mode-S EHS observation points. Additionally, one single Mode-S EHS observation point is not representative for one single L2B HLOS wind observation as the latter is retrieved with a certain integration length L_{int} [Sec. 3.2.3]. Nevertheless, as for a first order approximate[69] to define σ_{ref}:

$$\sigma_{ref} = \frac{1.4}{\sqrt{N}}, \tag{50}$$

which is the *Square Root n Law*. As a result, a fixed reference with a fixed value for σ_{ref} cannot be achieved and utilizing the Taylor-diagram becomes limited for this specific case. In order to utilize the advantages of constructing Taylor-diagrams, it is decided to set $\sigma_{ref} =$ 1.4 ms^{-1} to fix the reference nevertheless. This decision requires a relaxation about the interpretation of the geometric relationship [Eq. 48] to determine the value for E' —i.e. the CRMSD. Therefore, the actual bias values corrected for the *Square Root n Law* are shown in the legend. The decision to set $\sigma_{ref} = 1.4$ ms^{-1} does not influence the position of the markers w.r.t. the Pearson's correlation coefficient ρ nor the standard deviation σ_{obs}.

As the atmosphere is discretized into 3 layers for both channels —a total of 6 Taylor-diagrams have been constructed, each providing the pattern and variance of the 27 individual collocation runs with different collocation box parameters [Fig. 26, 27]. **Note:** a zoom-in version of two Taylor-diagrams will be provided later on in order to elaborate on the results. The following images provide a general sense of the pattern and variance in the markers.

[69] It can be postulated that a mathematical formulation of a structure function of the velocity field in turbulent flows in the collocation box is required to obtain a statistical description of the developed turbulent flow and hence how the Mode-S EHS wind component error estimate of —according to de Haan [2016] —1.4 $\pm$ 0.1 ms^{-1} for each single Mode-S EHS observation point scales.

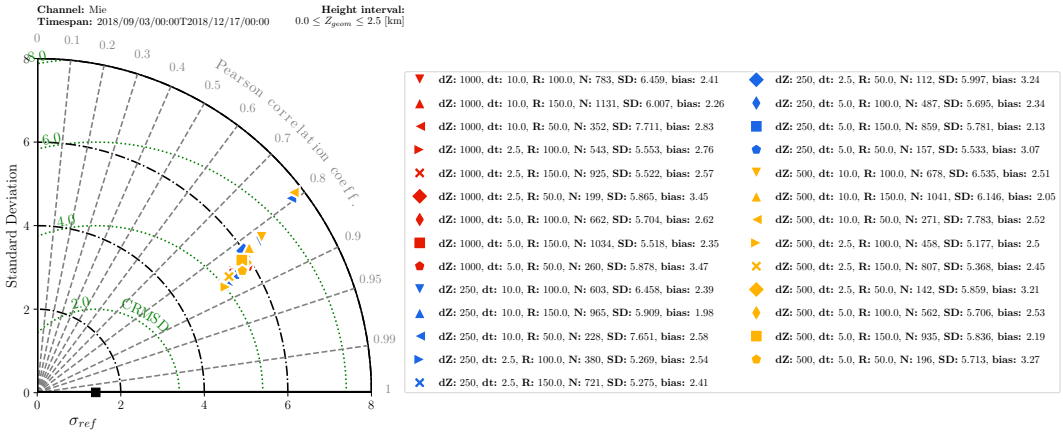

(a)

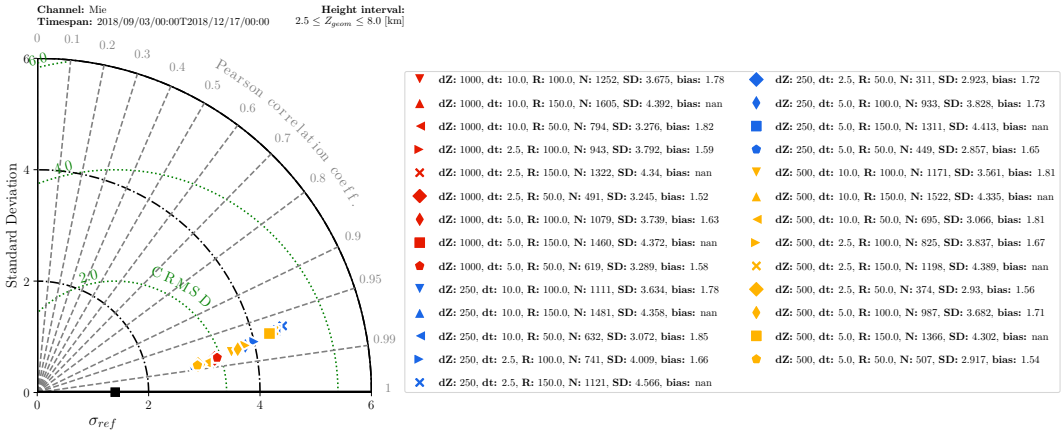

(b)

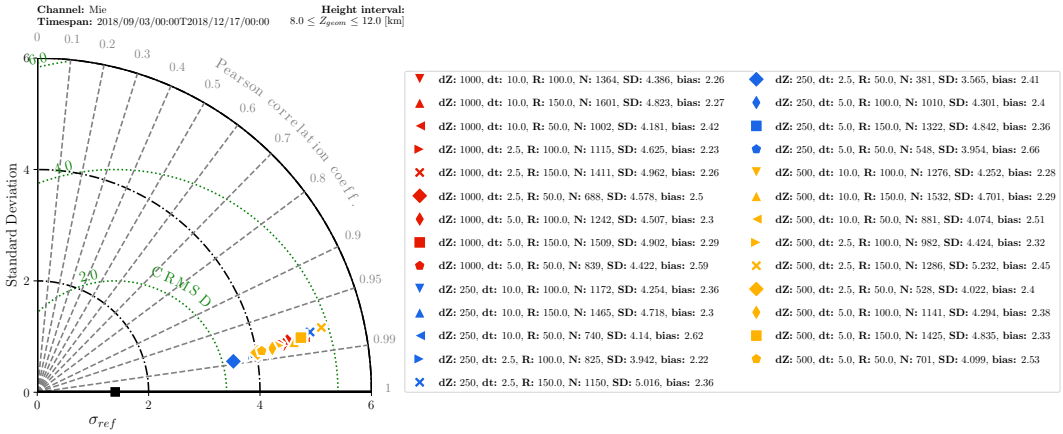

(c)

Figure 26: Taylor-diagram w.r.t to the Mie channel depicting the statistical performance of all 27 individual and independent collocation runs —illustrated as a coloured marker —between (a) $0.0 \leq Z_{geom} \leq 2.5$ km, (b) $2.5 \leq Z_{geom} \leq 8.0$ km, and (c) $8.0 \leq Z_{geom} \leq 12.0$ km. Each run is performed with a unique combination for the numerical values for dZ, dt and R to span the collocation box spatially and temporally. Note that 'SD' in the legend represents σ_{obs}, that is the standard deviation between L2B and Mode-S EHS [Eq. 39] rather than —as discussed in Sec. 6.1.2 —the standard deviation of the L2B data set it self.

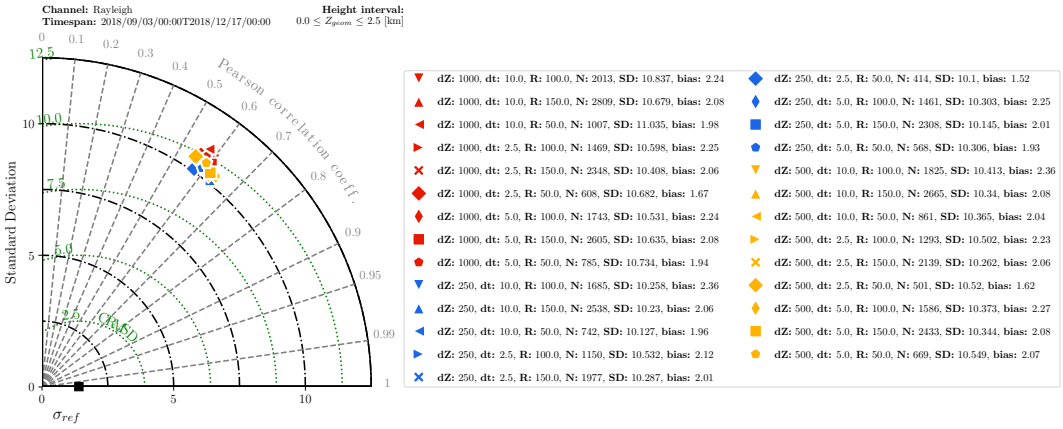

(a)

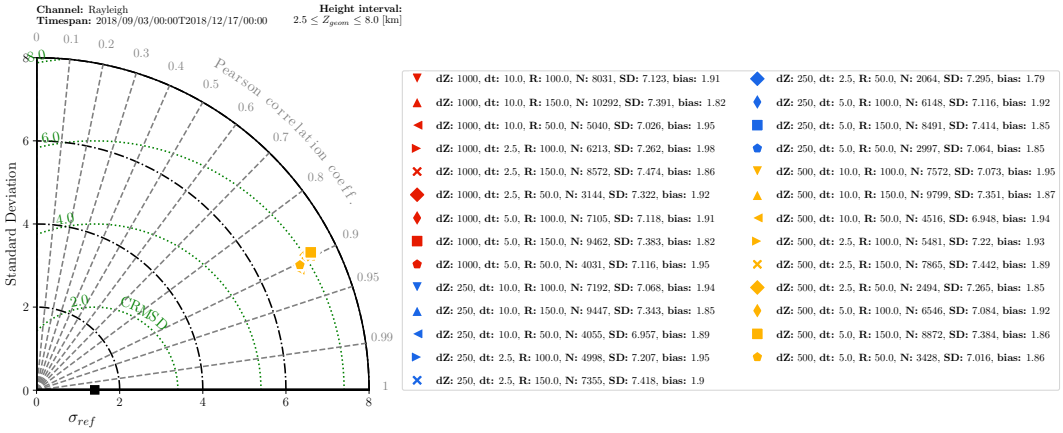

(b)

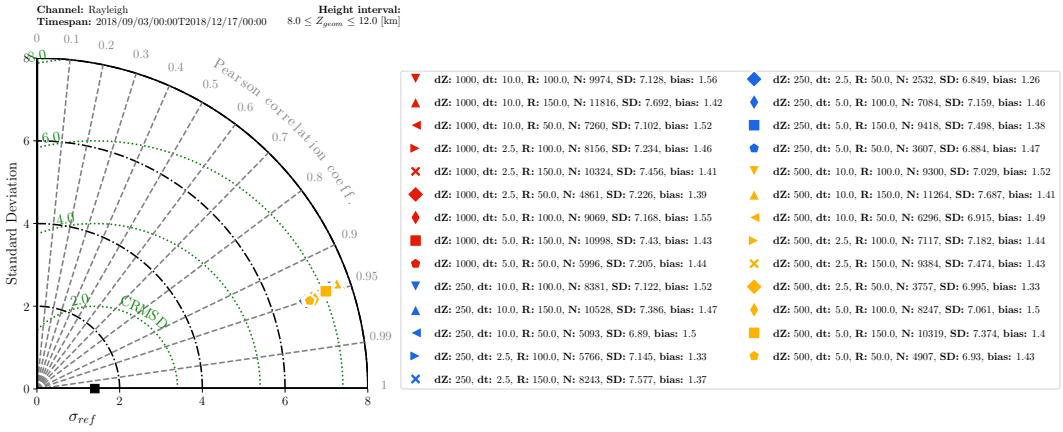

(c)

Figure 27: Taylor-diagram w.r.t to the Rayleigh channel depicting the statistical performance of all 27 individual and independent collocation runs —illustrated as a coloured marker —between (a) $0.0 \leq Z_{geom} \leq 2.5$ km, (b) $2.5 \leq Z_{geom} \leq 8.0$ km, and (c) $8.0 \leq Z_{geom} \leq 12.0$ km. Each run is performed with a unique combination for the numerical values for dZ, dt and R to span the collocation box spatially and temporally. Note that 'SD' in the legend represents σ_{obs}, that is the standard deviation between L2B and Mode-S EHS [Eq. 39] rather than —as discussed in Sec. 6.1.2 —the standard deviation of the L2B data set it self.

The green radial contour lines represents the CRMSD between each collocation run and the reference and is proportional to the radial distance to the black reference square on the x-axis. The RMSD is centered around the reference point, i.e. the CRMSD assumes that Mode-S EHS is unbiased. The black radial contour lines denotes lines of equal values for the standard deviation while on the radial axis the Pearson's correlation coefficient ρ is depicted.

According to Taylor [2001], the position of each marker in the Taylor-diagram quantifies how closely the collocation run matches the reference. The disadvantage of this statement in the case of this validation study is that it does not take into account for *statistical significance*. Therefore the number of collocations N is provided in the legend as well.

Note that the Taylor-diagrams for both channels demonstrate a significant higher variability in the L2B data set —expresses as the standard deviation σ_{obs}, that is the standard deviation between L2B and Mode-S EHS [Eq. 39] —when compared to the fixed Mode-S EHS reference of $\sigma_{ref} = 1.4$ ms^{-1}. One of the reasons is due to quality control criteria which allows for Mie HLOS wind observations with an error estimate up to 3 ms^{-1} and Rayleigh HLOS wind observations with an error estimate up to 8 ms^{-1} [Sec. 5.1.1].

To determine the 'best'[70] collocation run out of 27 individual runs for each 6 constructed Taylor-diagrams, the method of deduction and trade-offs[71] is used rather than simply picking the marker closest to the black reference square σ_{ref} in stead. Since it is hard to see exactly the patterns of the markers, a zoom-in of the Taylor-diagram for both channels for $0.0 \leq Z_{geom} \leq 2.5$ is provided to support the upcoming conclusions [Fig. 28].

[70] At least to reduce the arbitrary *a priori* chosen collocation parameters for the collocation box.

[71] Without doubt, proper scientific methods are available to quantify the best run. At the time of interpreting and analyzing the Taylor-diagrams, the method of deduction and trade-offs was at the time being satisfying nevertheless —especially since all markers are relatively very clustered.

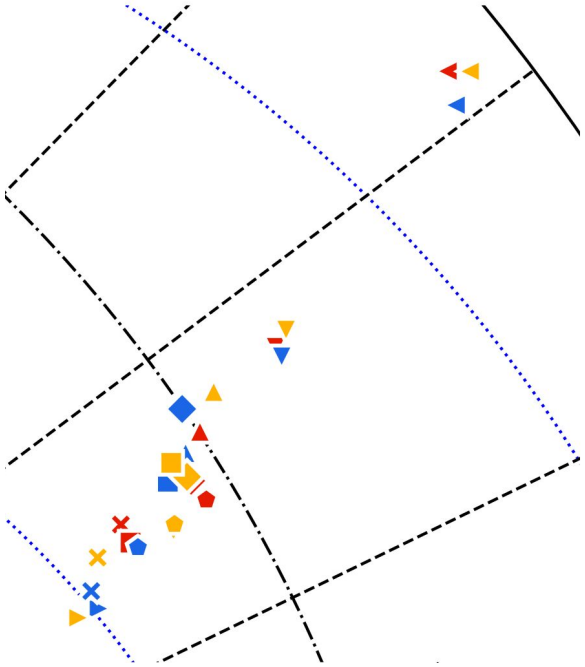

(a)

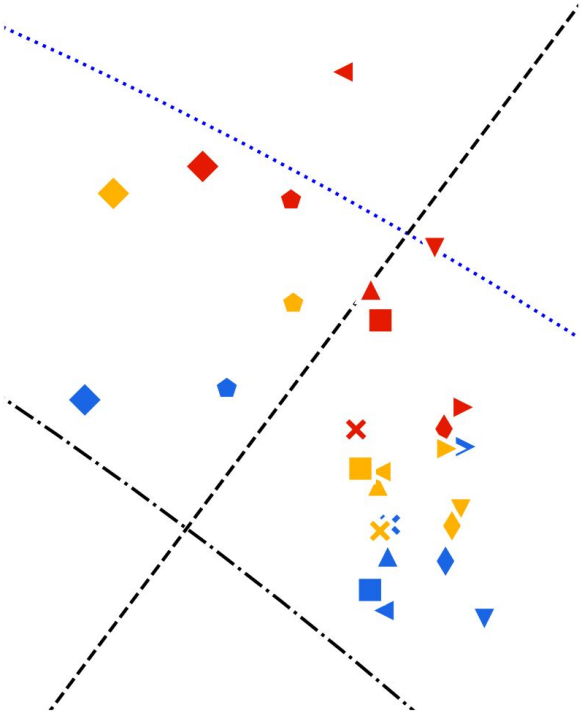

(b)

Figure 28: Zoom-in of (a) Fig. 26a, and (b) Fig. 27a.

To conclude this subsection, it is postulated that different collocation parameters for the collocation box are desired at different atmospheric layers. This statement can be underlined by the research findings based on the constructed Taylor-diagrams:

- between $0.0 \leq Z_{geom} \leq 12.0$ [km] the Taylor-diagrams for both channels reveal a pronounced distinction in the patterns of the markers and therefore the sensitivity in the results of how once defines the collocation box for each collocation run.

  Collocation runs w.r.t. the Rayleigh channel depicts markers to be clustered [Fig. 27]. Clustering of the markers indicates a lower sensitivity in the results for each collocation run and hence a higher robustness for variations in defining the collocation box.

  Collocation runs w.r.t. the Mie channel demonstrates a pronounced sensitivity in the results for each collocation run when noting that the markers are more widespread from each other [Fig. 26]. This illustrates a weakening of robustness for variations in defining the collocation box.

- clustered markers with the same symbols [Fig. 28a] implies that the results of the collocation run is significantly dependent on the numerical value of the radius R and collocation time-window dt. The results are less sensitive in how one defines the height increment dZ of the collocation box.

- clustered markers with the same colours [Fig. 28b] implies that the results of the collocation run is significantly dependent on the numerical value of the height increment dZ of the collocation box, but to a lesser extent in the numerical values for R and dt.

Furthermore:

- between $2.5 \leq Z_{geom} \leq 12.0$ [km] the Taylor-diagrams demonstrate a significant smaller radius for the collocation box for the Mie channel when compared to the radius values for the Rayleigh channel. This statement is in line when compared with the probability density function (PDF) plot of L_{int} [Fig. 8] as discussed in Sec. 3.2.3 —illustrating larger integration length L_{int} values for the Rayleigh channel when compared to L_{int} values for the Mie channel.

  Conversely, between $0.0 \leq Z_{geom} \leq 2.5$ [km] both channels require a large radius for the collocation box —in the order of 150 km —which is the result of more clustered Mode-S EHS data in the vicinity of airports at lower altitudes [see Fig. 23a] and therefore requiring a larger search area to collocate.

- in terms of collocation time-window, between $0.0 \leq Z_{geom} \leq 2.5$ [km] and $8.0 \leq Z_{geom} \leq 12.0$ [km] the collocation time-window dt for the Mie channel is shorter in contrast to the collocation time-window for the Rayleigh channel. As the Mie channel receives backscattering of aerosols and clouds, which can be accompanied by convective and turbulent processes resulting into highly fluctuating wind velocities, the collocation box for the Mie channel requires to be small in order to decrease representativeness errors. In contrast to the Rayleigh channel which receives backscattering of atmospheric molecules in clear skies, which is usually accompanied with not such

convective and turbulent processes[72], therefore allowing for longer collocation time-windows.

The final results are summarized and presented in a table [Tab. 7]. These results are used to define the collocation box per discrete atmospheric layer and per channel as discussed before.

atm. layer [km]	**Mie channel**	**Rayleigh channel**
$0.0 \leq Z_{geom} < 2.5$	dZ = 500, dt = 5.0, R = 150	dZ = 250, dt = 10.0, R = 150
$2.5 \leq Z_{geom} < 8.0$	dZ = 500, dt = 5.0, R = 50	dZ = 1000, dt = 5.0, R = 100
$8.0 \leq Z_{geom} < 12.0$	dZ = 500, dt = 2.5, R = 50	dZ = 500, dt = 10.0, R = 100

Table 7: Defined numerical values for the collocation parameters per discrete atmospheric layer per channel with use of Taylor-diagrams.

6.3 Collocation results

After discussing a method to determine the collocation box parameters with use of the Taylor-diagram —this section will discuss the collocation results briefly.

6.3.1 Time series plot

A time series plot is constructed to get a general impression of the collocation results of the three preprocessed data sets [Fig. 29, 30]. The time series plot ranges for the complete time span in which the collocation is performed —from 2018-09-03[73] to 2018-12-15. Furthermore, the results of the Taylor-diagrams are used in the collocation algorithm to define the collocation box per discrete atmospheric layer for either the Mie or Rayleigh channel [see Tab. 7].

In terms of statistics, the mean collocated HLOS wind observation for the *observed* Mode-S EHS data (O_1) for the Mie channel[74] is 2.853 ms^{-1}, which is almost equivalent when compared to the *background* ECMWF IFS numerical model (B), which has a mean value of 2.860 ms^{-1}. Performing the same analysis w.r.t to the Rayleigh channel gives a mean of 0.919 ms^{-1} for Mode-S EHS and 0.893 ms^{-1} for ECMWF IFS, depicting again an almost perfect agreement.

Applying the *observed* - *background* ($O - B$) bias statistics (pronounced as 'observed minus background') —the value of ($O_1 - B$) demonstrates an almost zero bias of 0.023 ms^{-1} [purple shaded area in Fig. 31] —i.e. Mode-S EHS data is almost unbiased compared to ECMWF IFS. Moreover, the results are in accordance with the results found by [see e.g. de Haan, 2014], in which the quality of Mode-S is studied.

Performing ($O - B$) statistics for L2B as the other observed data set (O_2), the bias of ($O_2 - B$) for the Mie channel [black dash-dot line in Fig. 31] is in the order of 2.061 ms^{-1}.

[72] This statement is not true in the case of e.g. *clear air turbulence*.

[73] Shortly after launch at 22 August 2018 —approximately at the beginning of September 2018 Aeolus started to downlink its observational data.

[74] Despite the different wind retrieval principle for the aircraft-derived Mode-S EHS data, a distinction between the Rayleigh and Mie channel is maintained.

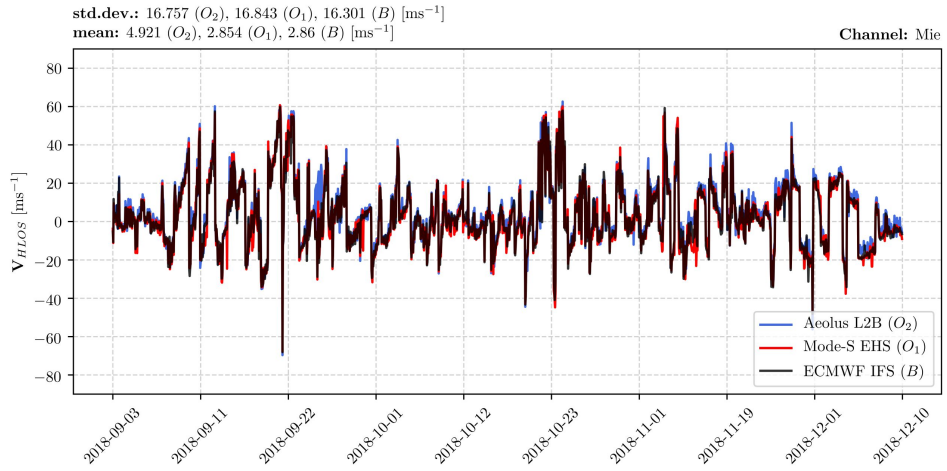

(a) Note the small variance, expressed as the standard deviation, in the Mie channel.

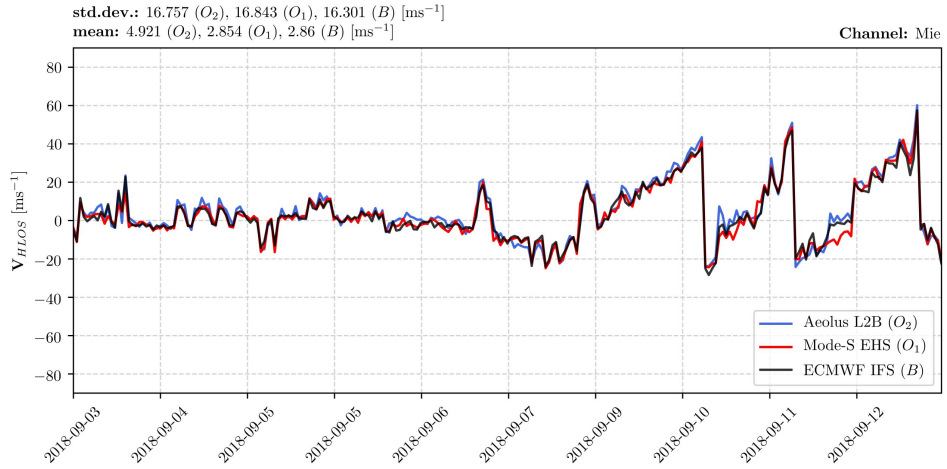

(b) Zoom-in of figure (a). The sharp drops at the end of the time series plot is the effect of changing orbit phase of Aeolus. Clearly depicted by this plot is the positive bias as the blue O_2-line is on average shifted slightly above the O_1-line and B-line.

Figure 29: Time series plot of consecutive collocated HLOS wind observation results for the Mie channel. Note that the plot is a rough plot since it is a plot of consecutive collocated HLOS wind observation results without being sorted per e.g. discrete height intervals. This clarifies the volatility of the time series plot and hence not the volatility of the actual HLOS wind observations nor the volatility of the atmosphere.

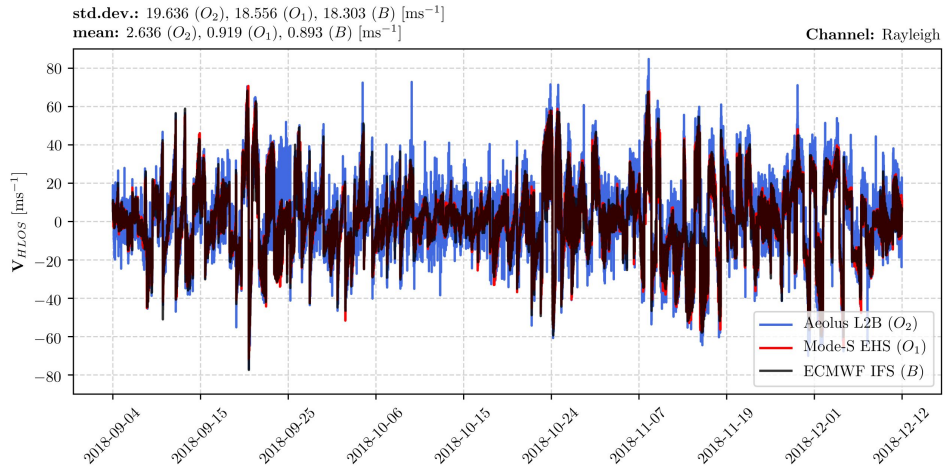

(a) Note the significant higher variance is the data set when compared to the Mie channel.

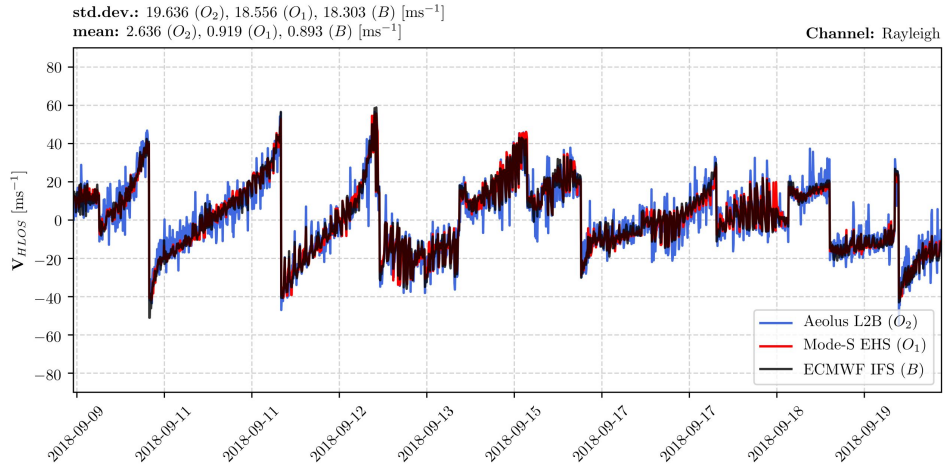

(b) Zoom-in of figure (a). The sharp drops are the effect of changing orbit phase of Aeolus. Note that when taking 2018-10-11 as day of interest, at the beginning of that day during the ascending orbit phase the instrument measured negative HLOS wind values, in contrary to the positive HLOS wind values at the end of the same day during its descending orbit phase. Following the definition of the HLOS wind vector [see e.g. Fig. 13], this does not indicate a reversal in the atmospheric wind direction but a westward wind.

Figure 30: Time series plot of consecutive collocated HLOS wind observation results for the Rayleigh channel.

For the Rayleigh channel [red dash-dot line in Fig. 31], the bias of $(O_2 - B)$ shows to be 1.742 ms^{-1}. The $(O - B)$ statistics thus demonstrates a higher bias for the Mie channel in comparison to the Rayleigh channel when comparing L2B with ECMWF IFS. When L2B is compared to Mode-S EHS, similar validation results are found as expected and demonstrates $(O_2 - O_1)$ to be 2.066 ms^{-1} for the Mie channel [black solid line in Fig. 31], and 1.669 ms^{-1} for the Rayleigh channel [red solid line in Fig. 31].

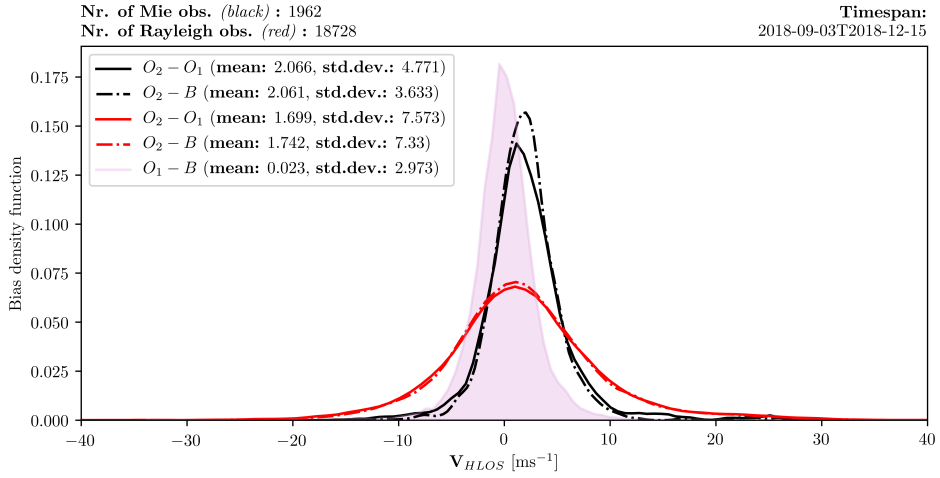

Figure 31: Probability density function of the overall bias for the two *observed* data sets Mode-S EHS (O_1), L2B (O_2) and the *background* ECMWF IFS (B). Clearly noticeable is the systematic bias in (O_2) as it is shifted from the 0 ms^{-1} center position.

In terms of variance in the data set, the time series plot for the Rayleigh channel illustrates a significant higher variance —expressed as the standard deviation —than the Mie channel. One of the reasons is due to quality control criteria which allows for Mie HLOS wind observations with an error estimate up to 3 ms^{-1} and Rayleigh HLOS wind observations with an error estimate up to 8 ms^{-1} [Sec. 5.1.1].

6.3.2 Scatter density plot

Scatter plots are constructed in order to illustrates the linearity and variance between between L2B and Mode-S EHS. Collocation is performed from 2018-09-03 to 2018-12-15. Note that the results of the Taylor-diagrams are used in the collocation algorithm to define for either the Mie or Rayleigh channel the collocation box per discrete atmospheric layer, that is between $0.0 \leq Z_{geom} < 2.5$ [km], $2.5 \leq Z_{geom} < 8.0$ [km] and $8.0 \leq Z_{geom} < 12.0$ [km] [see Tab. 7]. As the scatter density plots are the results for $0.0 \leq Z_{geom} < 12.0$ [km], one cannot compare the Taylor-diagram results directly with the scatter density plots.

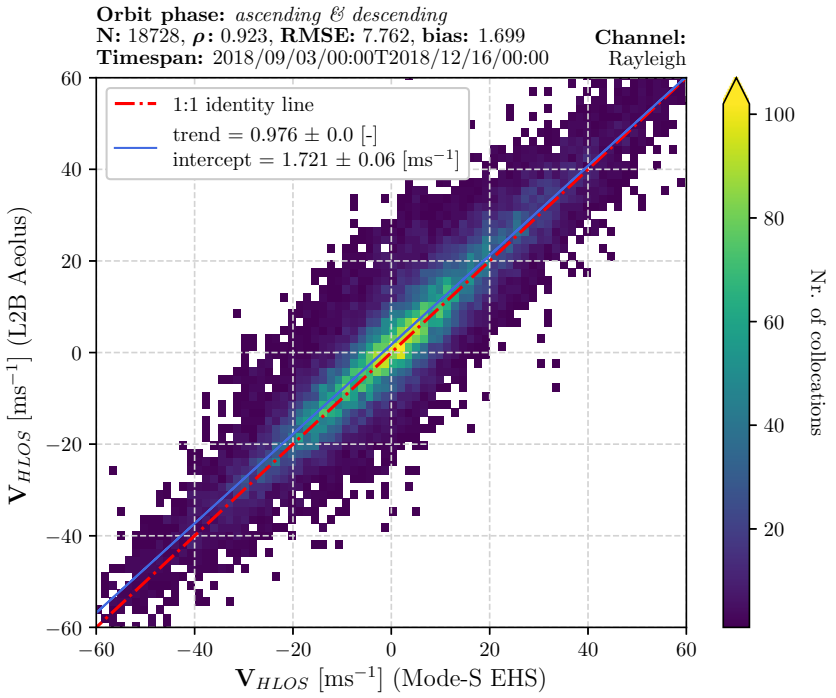

(a)

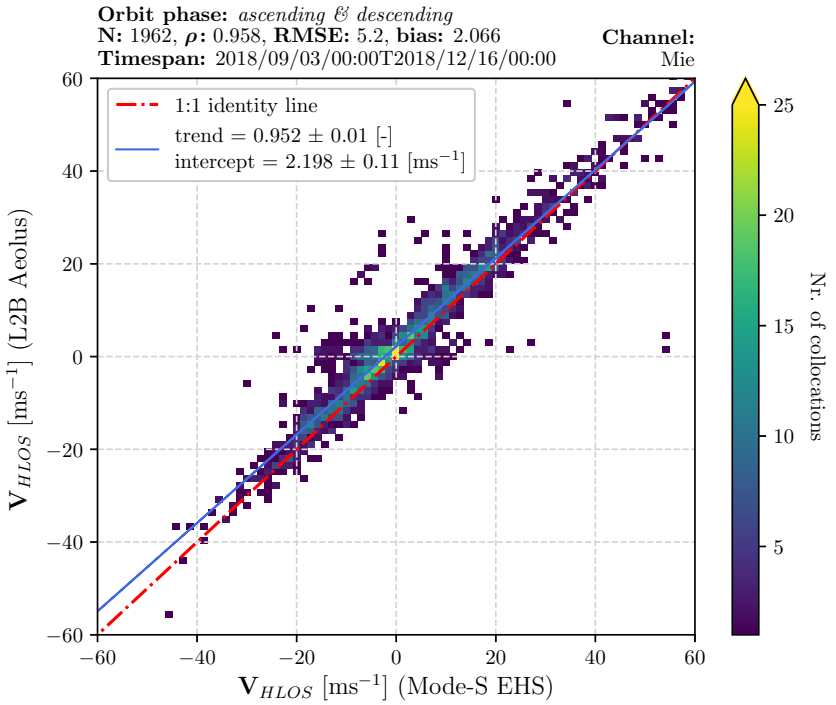

(b)

Figure 32: Scatter density plot for (a) the Rayleigh channel, and (b) the Mie channel.

Both scatter plots demonstrate a high positive linear relationship as depicted by the Pearson's correlation coefficient with $\rho = 0.923$ for the Rayleigh channel and $\rho = 0.958$ for the Mie channel. Making a distinction between both channels —$(O_2 - O_1)$ statistics reveals a systematic bias of 1.699 ms^{-1} and 2.066 ms^{-1} for the Rayleigh and Mie channel respectively, demonstrated by the off-set of the linear regression trend line w.r.t to the 1:1 line.

As air molecules are more abundant than aerosols or particles, significant more Rayleigh observations are obtained than Mie observations —hence the significant ratio in amount of collocations (N) in the scatter plot. A second argument is based on the applied quality control criteria. As Mie observations are only abundant in the lower part of the atmosphere —given that Mode-S EHS data becomes more clustered in the lower part of the atmosphere in the vicinity of airports —this provides a third argument for the ratio.

The RMSE for the Rayleigh channel is 7.762 ms^{-1} —significantly higher when compared to the 5.2 ms^{-1} for the Mie channel. This is the result of the higher variance in the data —noticeable in the spread in the Rayleigh scatter plot [Fig. 32a].

Returning to the analysis elaborating on the systematic bias —scatter plots per channel per orbit phase reveal a significant higher systematic bias during the descending orbit when compared to the ascending orbit. The cause can be e.g. orbital mechanics or thermal control of the satellite related, but is still under investigation by ESA and industry at the time of writing.

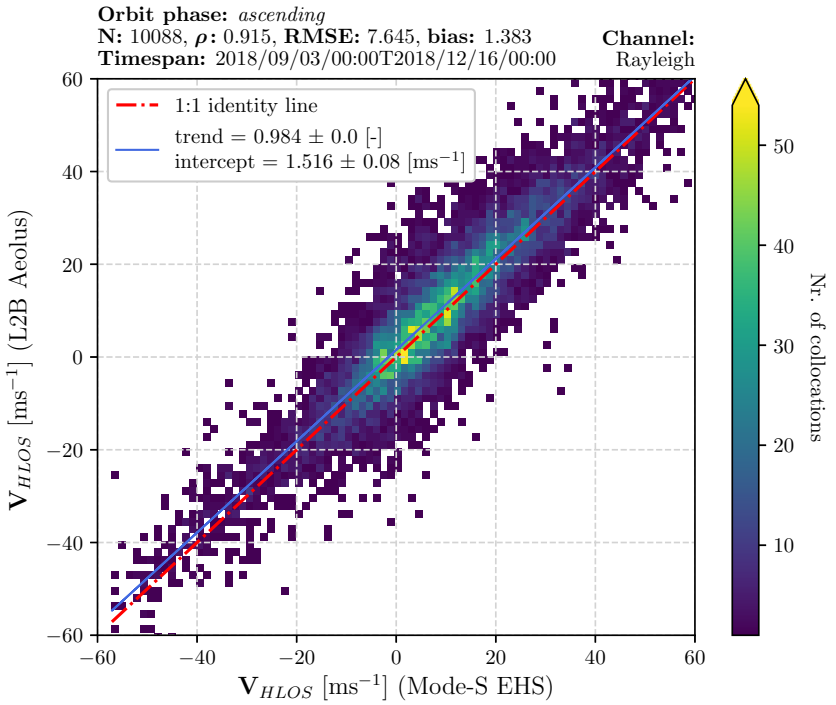

(a)

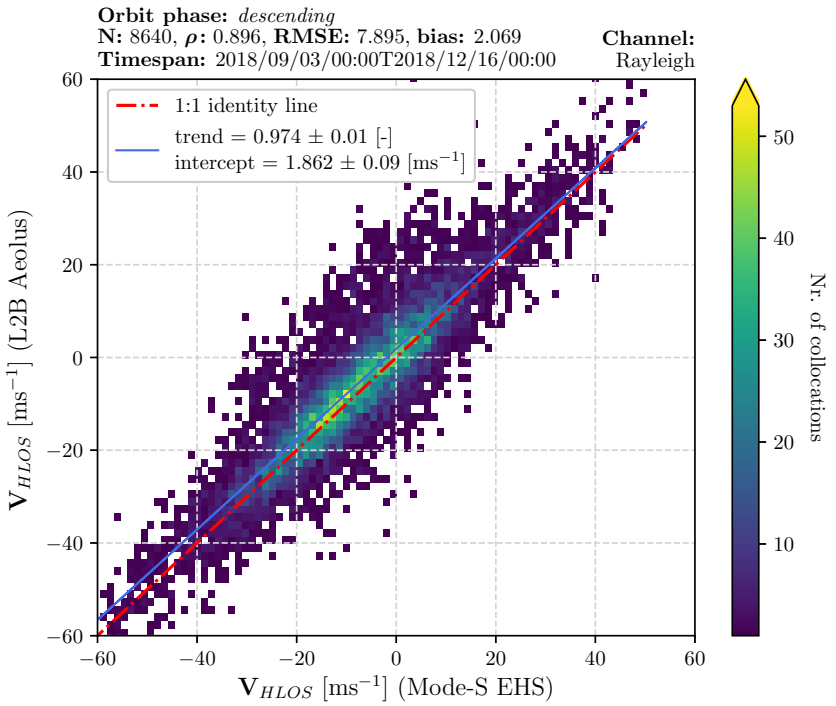

(b)

Figure 33: Scatter density plot for the Rayleigh channel during (a) the ascending orbit, and (b) during the descending orbit.

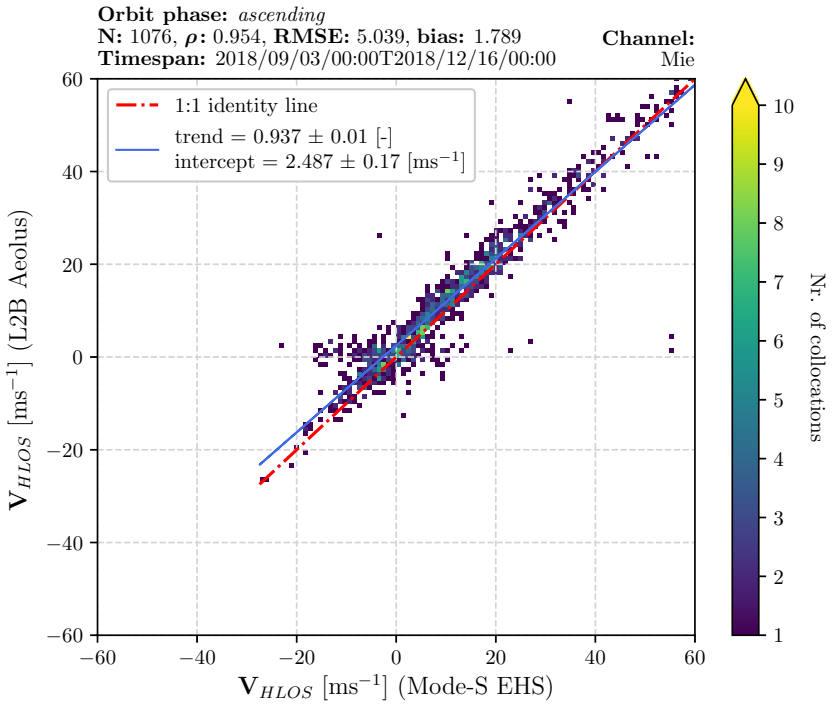

(a) The satellite measured on average positive HLOS wind values in the ascending orbit phases. Sign convection of HLOS geometry [Fig. 13] reveals a mean eastward wind direction during the collocation period.

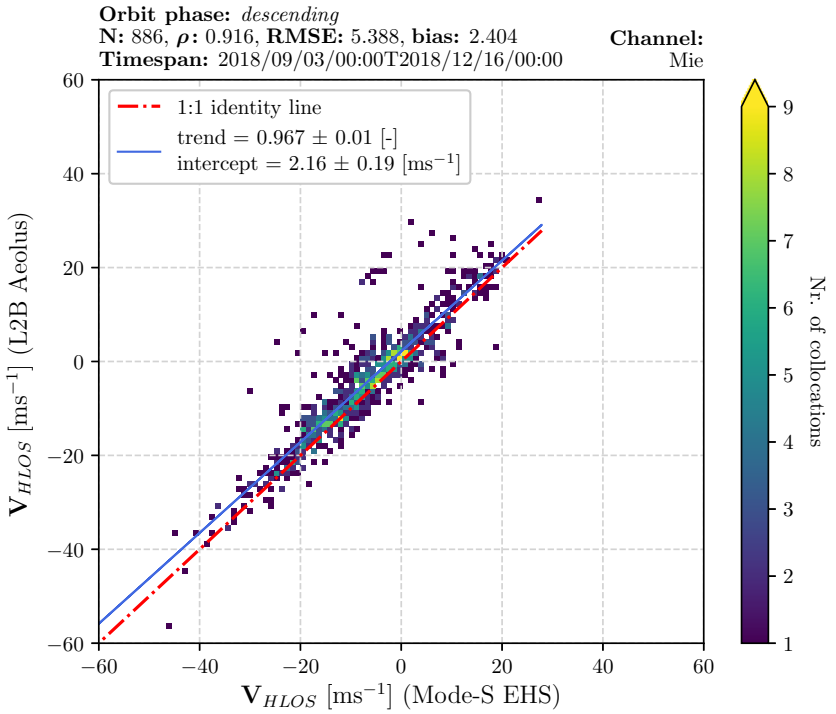

(b) Sign convection of HLOS geometry still reveals a mean eastward wind direction —i.e. no reversal of the wind.

Figure 34: Scatter density plot for the Mie channel during (a) the ascending orbit, and (b) during the descending orbit.

In terms of cross-checking the validation results —Geiß [2019] demonstrated similar results[75] during the *Living Planet Symposium* of ESA in Milan (Italy) in May 2019 when performing case studies for the validation of Aeolus wind observations with radar wind profilers over Germany.

6.3.3 Bias evolution over time

Further evaluation of the bias demonstrates a *bias drift*, i.e. an evolution in the bias as time progresses. Both channels depicts an increase in the bias evolution when plotting *box plots*[76][Fig. 35, 36], at which each single box plot represents a weekly sample. Note that the second quartile of each box plot —the green horizontal bar in each box plot —represents the median, not the mean.

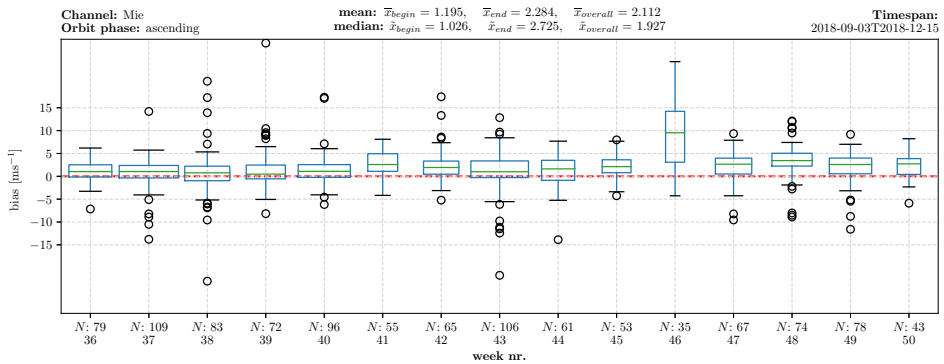

(a)

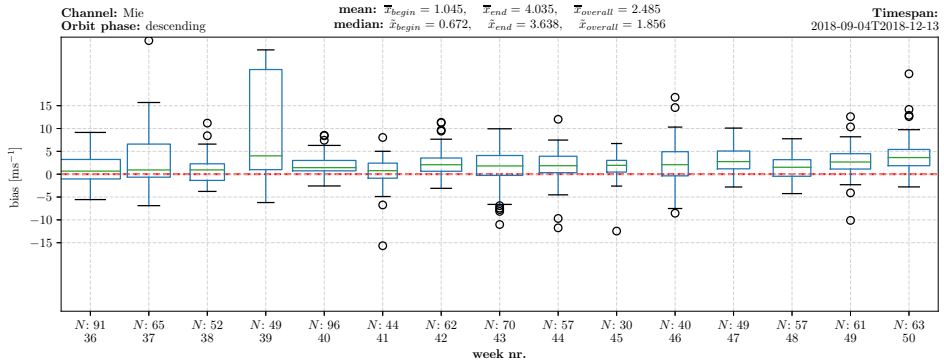

(b)

Figure 35: Box-plot of the bias [ms^{-1}] evolution for the Mie channel during (a) the ascending orbit, and (b) during the descending orbit. Sample size is denoted by N, i.e. the number of collocations.

[75] Time of writing of this statement is 2018/06/15.

[76] A box plot is a descriptive statistical method to depict graphically a sampled numerical data set based on their *quartiles*. The vertical line passing through each box represents the variability outside the upper quartile (= upper end of the box, i.e. 75^{th} percentile) and lower quartile (= lower end of the box, i.e. 25^{th} percentile), while the median (i.e. 50^{th} percentile) is depicted by the horizontal green bar in the middle of the box. The upper and lower cap of the vertical line represents the largest and smallest value respectively of the sampled data set, while outliers are indicated by individual small open circles.

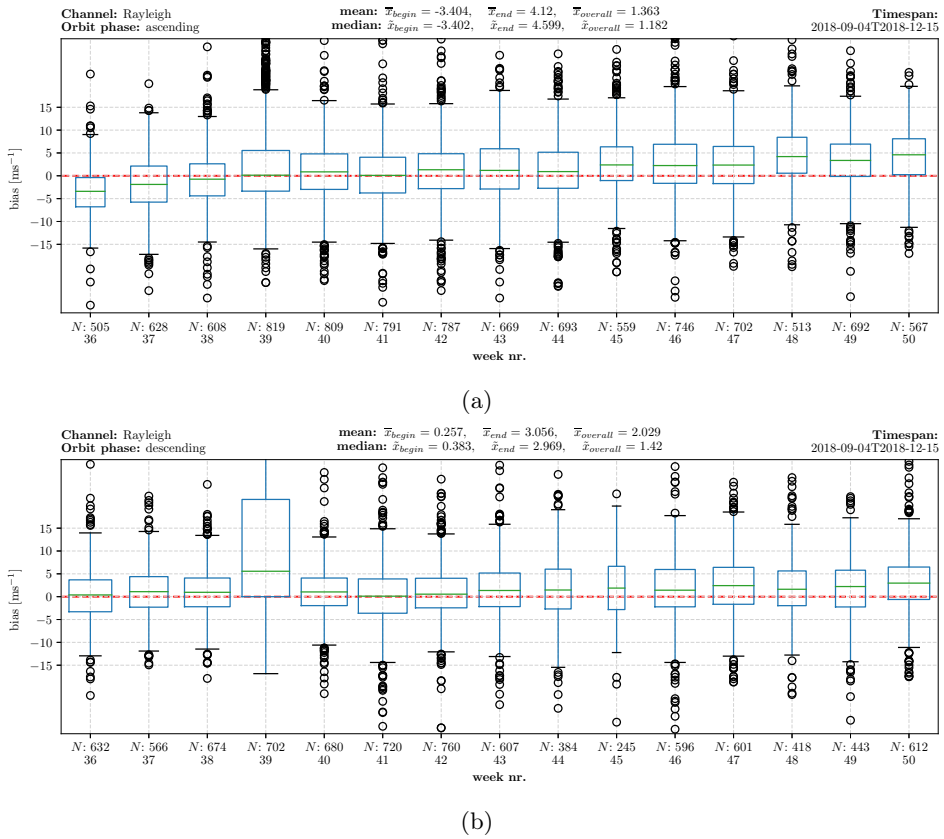

Figure 36: Box-plot of the bias [ms^{-1}] evolution for the Rayleigh channel during (a) the ascending orbit, and (b) during the descending orbit. Sample size is denoted by N, i.e. the number of collocations..

Both channels demonstrate —again —a higher bias during the descending phase when compared to the ascending phase. During the ascending phase for the Mie channel —the bias in the first collocation week ($\overline{x}_{begin}$) is in the order of 1.195 ms^{-1} and 2.284 ms^{-1} in the final collocation week ($\overline{x}_{end}$), with an overall mean bias ($\overline{x}_{overall}$) of 1.789 ms^{-1}. When compared to the descending orbit —values of $\overline{x}_{begin} = 1.045$ ms^{-1}, $\overline{x}_{end} = 4.035$ ms^{-1} and $\overline{x}_{overall} = 2.404$ ms^{-1} are found. Similar results are found for the Rayleigh channel —demonstrating a higher bias during the descending orbit in contrast to the ascending orbit. The exact cause is at the time of writing still under investigation by ESA and industry.

6.3.4 Vertical profiles

As the satellite measures wind profiles of the horizontal wind, it is informative to construct vertical ($O_2 - O_1$) statistics as well. As aircraft operations are limited[77] to an altitude of about 12 km —vertical profiles up to 12 km will be demonstrated.

[77] Novel aircraft such as the B787 and A350 are capable to operate above this altitude. Nevertheless, most current aircraft do not operate above 12 km frequently.

The mean L2B HLOS wind $\langle \mathbf{V} \rangle_{HLOS}$ for the Mie and Rayleigh channel [Fig. 37, 38 resp.] both illustrate an agreement in terms of correlation w.r.t. to Mode-S and ECMWF IFS. This agreement is in accordance with the Pearson's correlation coefficient ρ which —for both channels —increases with increasing height. The correlation coefficient near the PBL ($\sim 0 \leq Z_{geom} \leq 2.5$ km)[78] is smaller, probably due to increased atmospheric turbulence in the boundary layer.

Despite the agreement in terms of correlation —performing $(O_2 - O_1)$ statistics illustrates the aforementioned systematic bias to be in the order of about 2 ms^{-1} for both channels as both vertical profiles are systematic shifted towards the right w.r.t to Mode-S EHS and ECMWF IFS.

The bias spike in the Mie channel near e.g. $Z_{geom} = 3.5$ km ($Z_{geop} \approx 657$ hPa) and near e.g. $Z_{geom} = 6.5$ km ($Z_{geop} \approx 440$ hPa) for the Rayleigh channel is the result of significant outliers[79] in the data set —in particular due to the occurrence of so-called *hot-pixels*[80] in the ACCD [Sec. 3.2.1].

In terms of the variance —the standard deviation for the Mie channel [middle panel of Fig. 37] fluctuates significantly, while a steady profile is noted for the Rayleigh channel [middle panel of Fig. 38]. The magnitude of the standard deviation for both channels is in agreement with the *a priori* known estimated error —as reported by the L2B BUFR product —and indicates a higher variance in the Rayleigh channel when compared to the relative low variance in the Mie channel [blue envelope of Fig. 37, 38]. This was noticeable in the aforementioned scatter plot as well —the spread in the Rayleigh scatter plot [Fig. 32a] in contrast to a narrow-spread in the Mie scatter plot [Fig. 32b]. Also plotted are vertical profiles for the MAD —used as a *consistent estimator* for the standard deviation σ [Sec. 6.1.3], i.e. MAD $:= \kappa\sigma$ with $\kappa \approx 1.4826$ as a constant scaling factor to approximate the standard deviation. The advantage of using the MAD is its robustness for e.g. outliers, i.e. less sensitive for abrupt variances in the data set.

[78] Note that the height of the PBL is not fixed but on average near these values.

[79] Formal proof of the origin of the occurrence of outliers is —at this moment —beyond the scope of the validation research. Further specific in-depth knowledge is required to study the origin of outliers. Origins can be e.g. systematic, instrumental or meteorological related.

[80] Hot-pixels are *dark-currents* in the ACCD [Sec. 3.2.1] which do not perform correctly and are able to bias the measurements significantly. The disadvantage of these hot-pixels is their randomness in occurrence —they appear and disappear without a clear systematic behaviour or cycle. It is hard to predict or even correct for them and is still —time of writing this sentence: 19/06/2019 —being investigated by ESA and its partners.

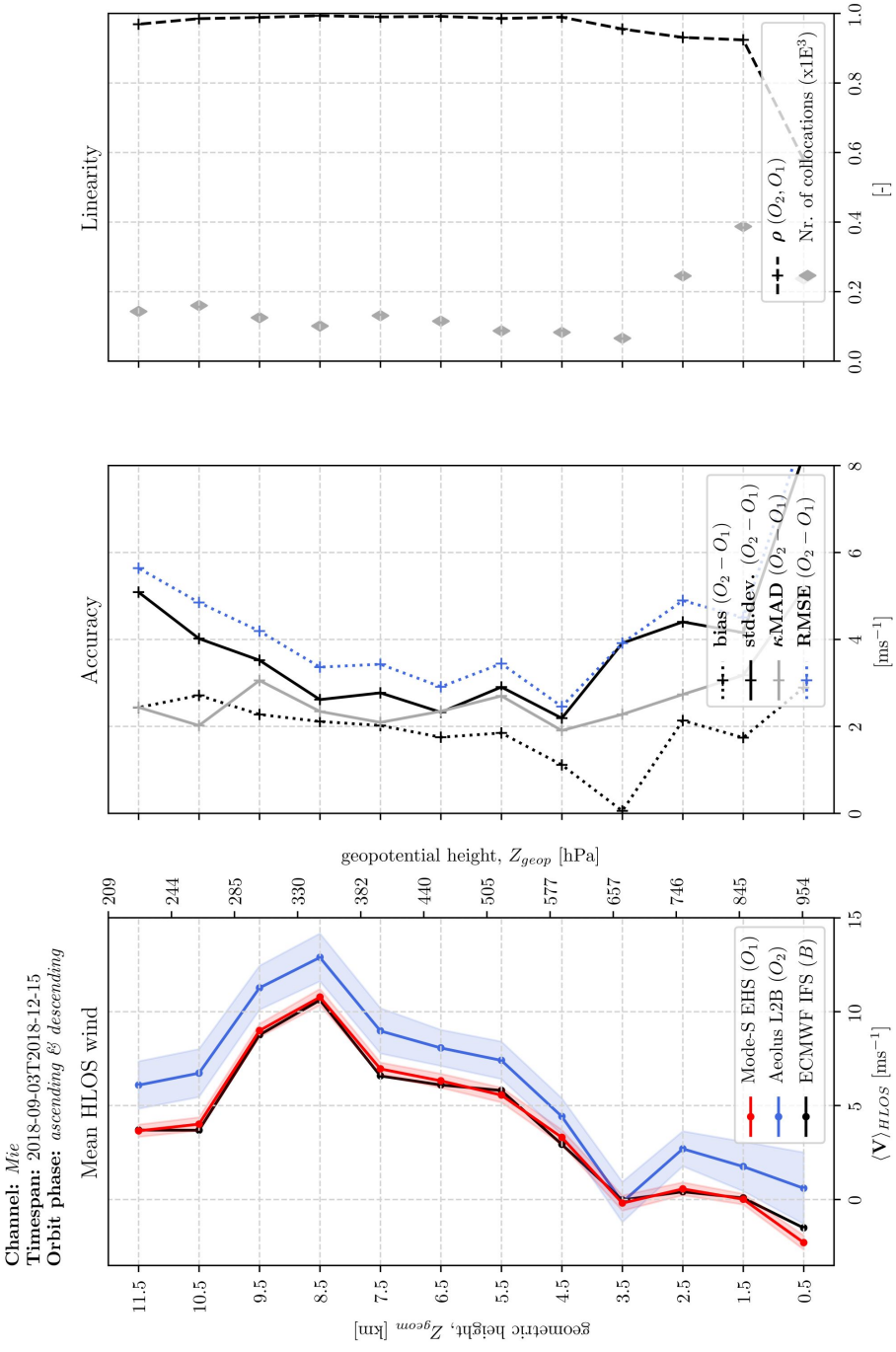

Figure 37: Vertical profiles of the collocation results for the Mie channel. Left panel depicts the mean HLOS wind observation for L2B (blue), Mode-S EHS (red) and ECMWF IFS (black). $(O_2 - O_1)$ statistics are shown in the middle panel, while the right panel illustrates the Pearson's correlation coefficient together with the number of collocations. The red shaded area in the left panel for Mode-S EHS represents the estimated error with use of the *Square Root n Law*, i.e. $1.4/\sqrt{N}$ in which 1.4 ms^{-1} is the *a priori* known standard error for one single Mode-S EHS observation [de Haan, 2016] while N is the number of Mode-S EHS observations per collocation box. The blue shaded area represents the error estimates as reported in the BUFR file.

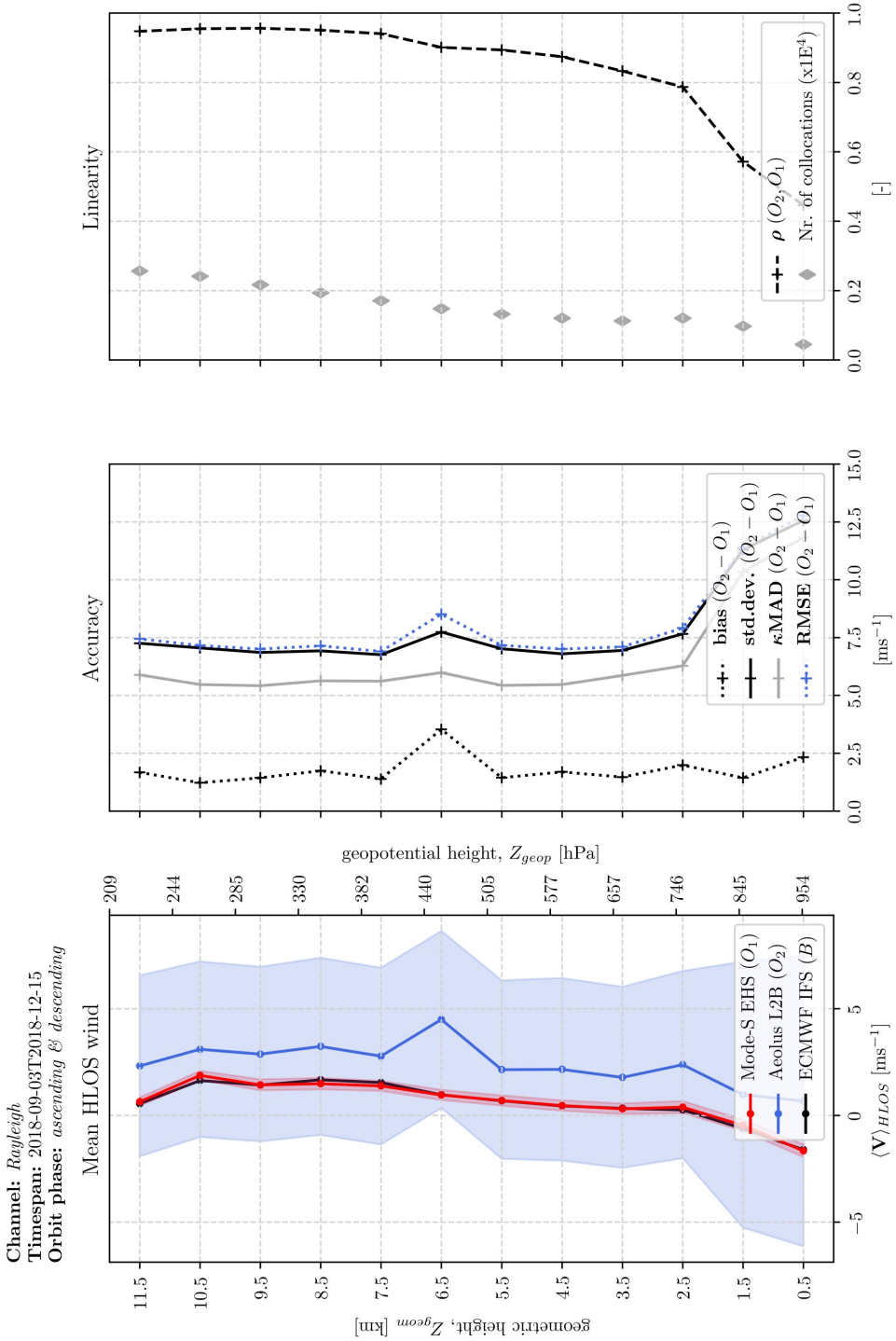

Figure 38: Vertical profiles of the collocation results for the Rayleigh channel. Left panel depicts the mean HLOS wind observation for L2B (blue), Mode-S EHS (red) and ECMWF IFS (black). $(O_2 - O_1)$ statistics are shown in the middle panel, while the right panel illustrates the Pearson's correlation coefficient together with the number of collocations. The red shaded area in the left panel for Mode-S EHS represents the estimated error with use of the *Square Root n Law*, i.e. $1.4/\sqrt{N}$ in which 1.4 ms^{-1} is the *a priori* known standard error for one single Mode-S EHS observation [de Haan, 2016] while N is the number of Mode-S EHS observations per collocation box. The blue shaded area represents the error estimates as reported in the BUFR file.

Same vertical profiles are constructed when making a distinction between the orbit phase —indicating the bias to be systematically higher during the descending orbit phase for both channels [Fig. 39 - 42].

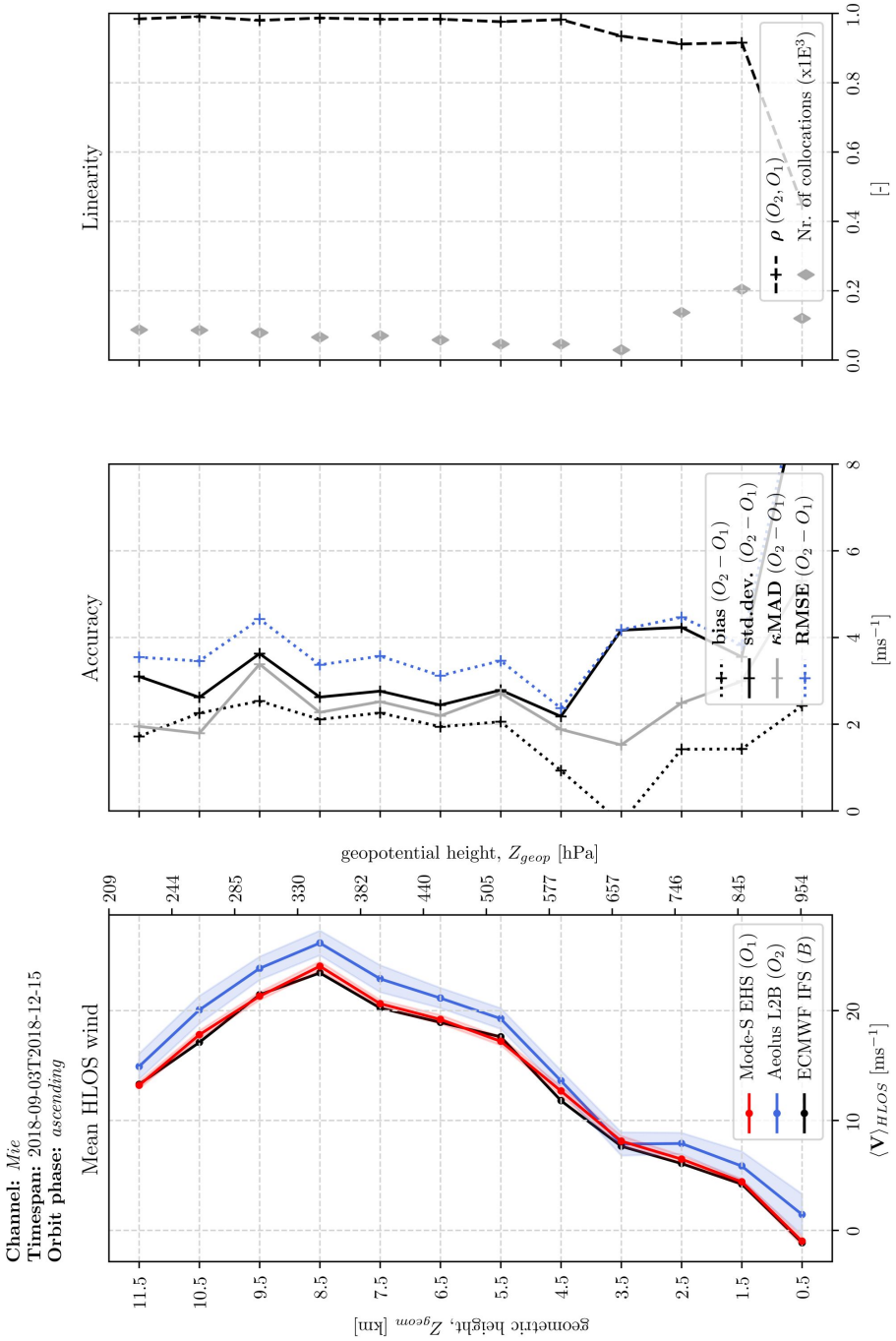

Figure 39: Vertical profiles of the collocation results for the Mie channel during the ascending orbit.

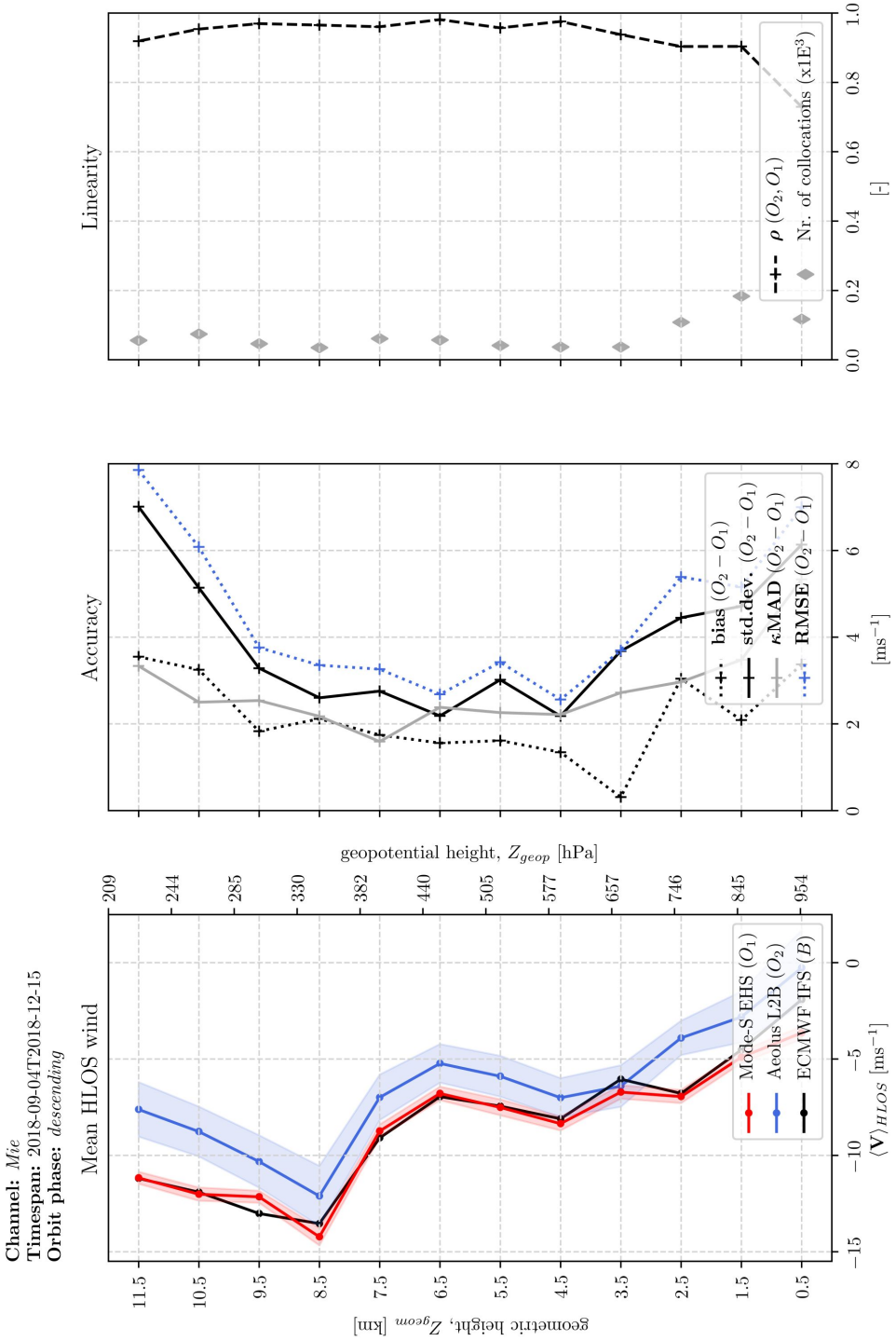

Figure 40: Vertical profiles of the collocation results for the Mie channel during the descending orbit.

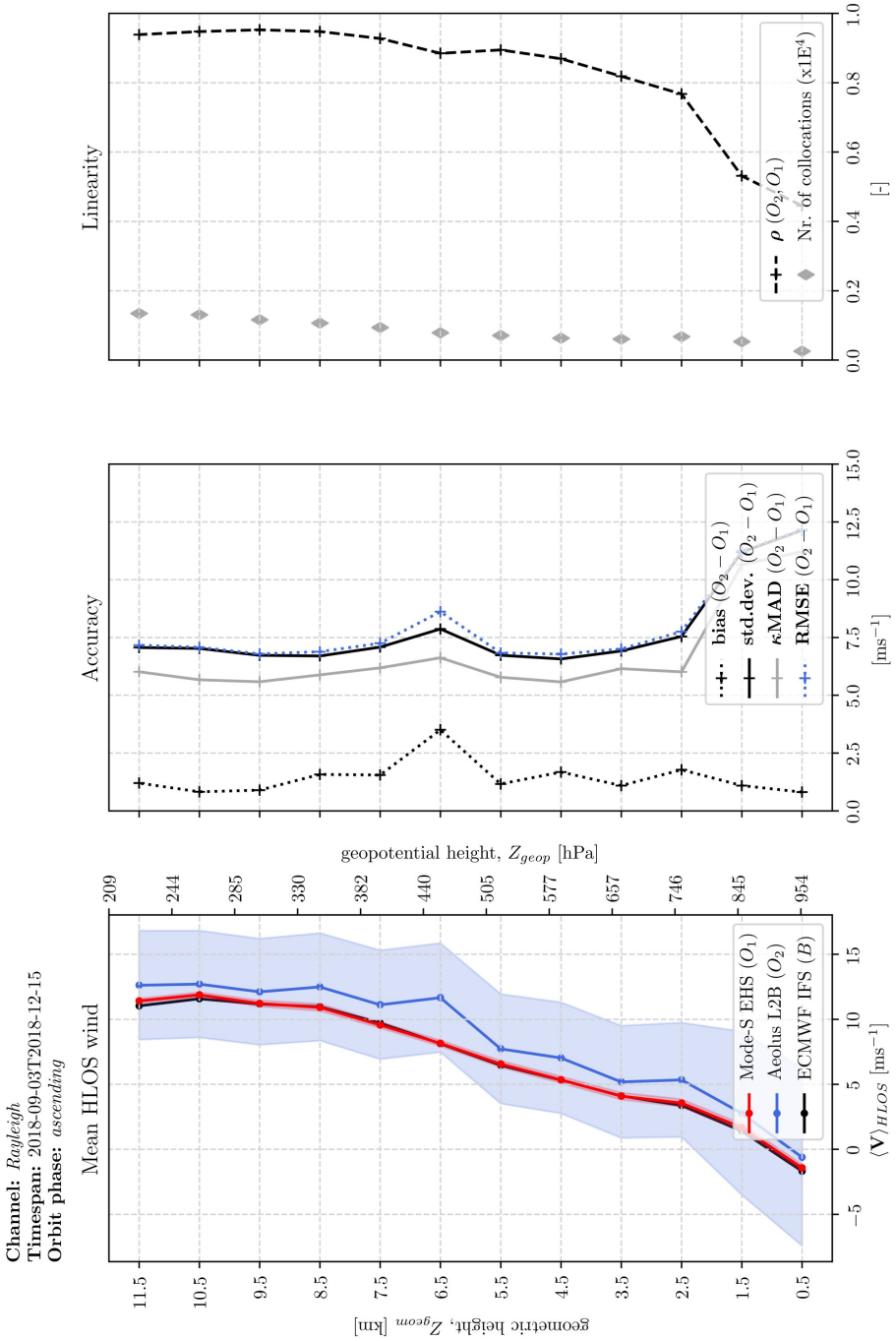

Figure 41: Vertical profiles of the collocation results for the Rayleigh channel during the ascending orbit.

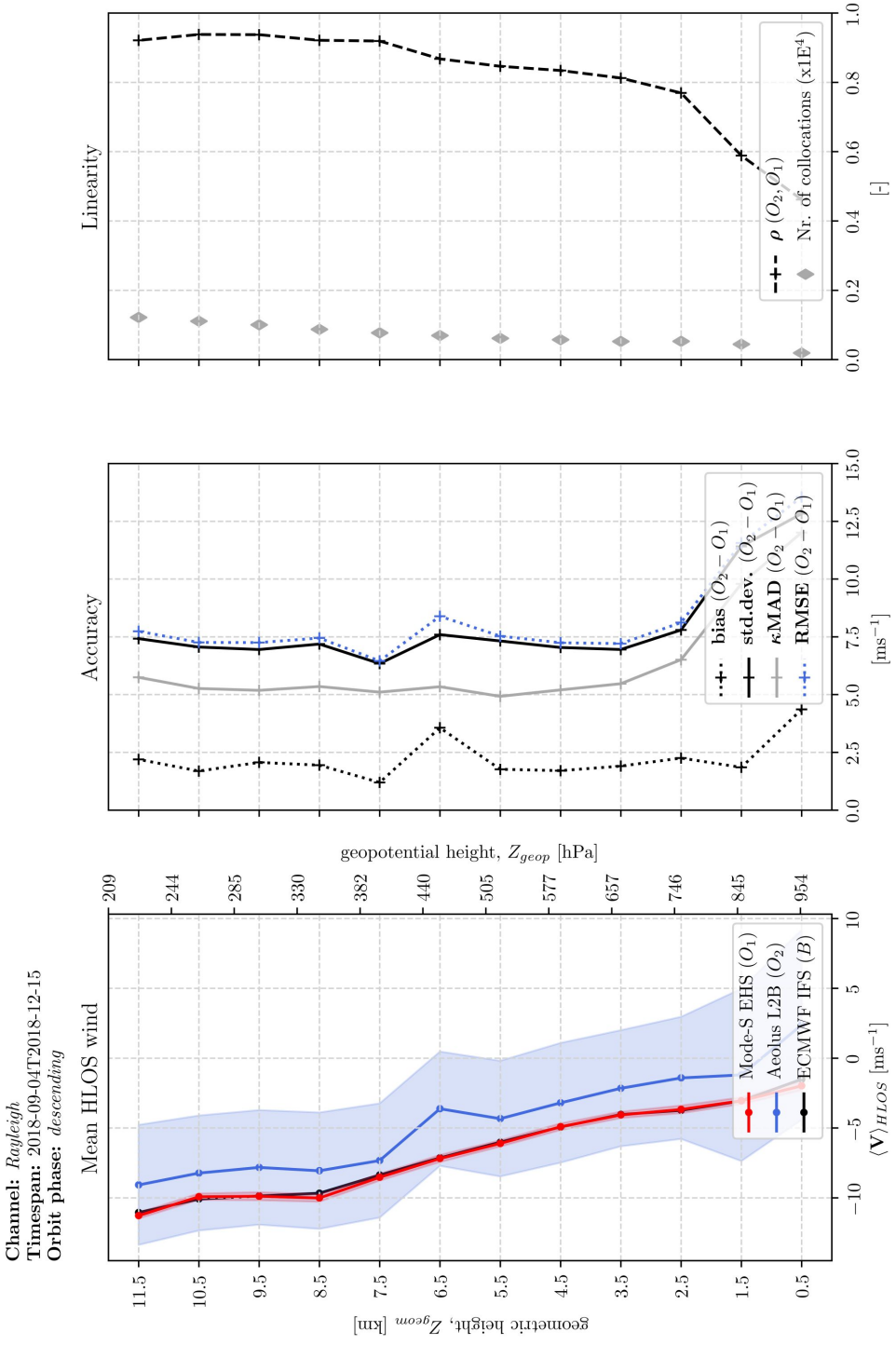

Figure 42: Vertical profiles of the collocation results for the Rayleigh channel during the descending orbit.

6.4 Estimating wind observation errors using the triple collocation method

Information on the accuracy of HLOS wind observations is essential to assess the applicability of e.g. data assimilation in NWPs or in climatological studies. Gathering accurate information about the accuracy of the observations is in general difficult since the 'truth' is unknown. A certain reference is therefore required which functions as an equivalent of the HLOS wind observations. In this validation study —the reference equivalent is the Mode-S EHS aircraft-derived data. Nevertheless, the challenge of this methodology is that the reference equivalent also includes the (unknown) model error which complicates the comparison studies.

By applying the *triple-collocation* method [Stoffelen, 1998; Stoffelen and Vogelzang, 2012] on three independent and uncorrelated collocated data sets, the three absolute error variances and linear intercalibration coefficients for these data sets can be obtained. This method has only been applied to a few studies extensively such as in scatterometer wind studies in which validation research is performed by comparing scatterometer winds with collocated winds measured by ocean buoys and measured by the ECMWF IFS model. According to Stoffelen and Vogelzang [2012], one of the reasons that the triple collocation method is not yet used frequently may be the fact that three independent and collocated data sets are required —which is in practise often hard to establish. Since in this validation study thee independent, uncorrelated and collocated systems are used —L2B, Mode-S EHS and ECMWF IFS —the method of triple collocation can be applied in principle.

In this section the triple collocation derived observation error for the L2B HLOS wind observations will be discussed. After a brief theoretical background of this method, the results will be demonstrated.

6.4.1 Theoretical background of the triple collocation method

In order to obtain the absolute error variances and the linear intercalibration coefficients using the triple-collocation method, three independent and uncorrelated collocated observations are required. Following Stoffelen and Vogelzang [2012], these observations are each described by the following error model:

$$x_i = \alpha_i t + \beta_i + \varepsilon_i \quad \forall t \in \mathbb{R}\ ,\ i = 0, 1, 2. \tag{51}$$

where x_i represents a collocated measurement for system i, t is the common geophysical quantity, α_i represents a calibration scaling coefficient and is designated as the *trend coefficient* while the calibration bias coefficient β_i is the *bias coefficient*. The random error of system i is denoted by ε_i. The latter requires to have zero average. Furthermore, the random errors of system i requires to be uncorrelated to each other —i.e. to the common geophysical quantity t and to the calibration coefficients α_i, β_i.

Denoting averages by the brackets $\langle\rangle$, forming the *first-order moments*:

$$M_i := \langle x_i \rangle = \alpha_i \langle t \rangle + \beta_i + \langle \epsilon_i \rangle \tag{52}$$

Recall that the random error of system ε_i has zero mean —implying that $\langle \varepsilon_i \rangle \equiv 0$ —such that redefinition of the first-order moments becomes

$$M_i := \langle x_i \rangle = \alpha_i \langle t \rangle + \beta_i \tag{53}$$

and an expression for the bias can be expressed as:

$$\beta_i = M_i - \alpha_i \langle t \rangle \quad \text{where } \beta_0 \equiv 0 \tag{54}$$

Without loss of generality, system 0 is designated as the reference (or 'truth') system —obeying a perfect linear and unbiased relationship. This implies that the trend coefficient $\alpha_0 \equiv 1$ and the bias coefficient $\beta_0 \equiv 0$, such that the latter expression for system 0 [Eq. 54] reduces to:

$$M_0 = \langle t \rangle. \tag{55}$$

In the study of the triple-collocation method, explicit expressions for trend coefficients, bias coefficients and error variances are to be found. The first set of explicit bias coefficients is found by substitution of Eq. 55 into Eq. 54:

$$\therefore \quad \beta_i = M_i - \alpha_i M_0 \tag{56}$$

Explicit expressions for the error variance can be determined by defining the *second-order moments*:

$$M_{i,j} := \langle x_i x_j \rangle \quad \text{for } i, j = 0, 1, 2 \tag{57}$$

Multiplying the error model x_i with x_j, averaging the results and applying elementary algebra while assuming mutually uncorrelated parameters in Eq. 51 —the second-order moments becomes:

$$M_{i,j} = \alpha_i \alpha_j \langle t^2 \rangle + [\alpha_i \beta_j + \alpha_j \beta_i] \alpha_j \langle t \rangle + \beta_i \beta_j + \langle \varepsilon_i \varepsilon_j \rangle = \langle x_i x_j \rangle. \tag{58}$$

The expression for the bias [Eq. 54] can be substituted into the latter expression. After doing so and rearranging the terms, this yields:

$$M_{i,j} = \alpha_i \alpha_j \langle t^2 \rangle - \alpha_i \alpha_j M_0^2 + M_i M_j + \langle \varepsilon_i \varepsilon_j \rangle \tag{59}$$

Introducing the *co-variance* matrix as:

$$C_{i,j} := M_{i,j} - M_i M_j, \tag{60}$$

and the *common variance* τ^2 of the three collocated systems as:

$$\tau^2 := \langle t^2 \rangle - M_0^2, \tag{61}$$

then the set of equations for the second-order moments [Eq. 58] can be simplified to covariance equations:

$$C_{i,j} = \alpha_i \alpha_j \tau^2 + \langle \varepsilon_i \varepsilon_j \rangle = \alpha_i \alpha_j \tau^2 + \delta_{i,j} \sigma_i^2, \tag{62}$$

where $\delta_{i,j}$ is the generalized *Kronecker*[81] *delta*. The Kronecker delta is defined as:

[81] Named after the German mathematician Leopold Kronecker (1823 - 1891), who contributed in the field of number theory, algebra and logic.

$$\delta_{i,j} \equiv \begin{cases} 1, & \text{if } i = j \\ 0, & \text{if } i \neq j. \end{cases} \tag{63}$$

The co-variance matrix is symmetric about the diagonal, i.e. $C_{i,j} = C_{j,i}$, and the error variances are found by the entries on the diagonal. Hence, solving for the diagonal co-variance equations gives explicit expressions for these error variances:

$$\therefore \quad \sigma_i^2 = C_{i,i} - \alpha_i^2 \tau^2, \tag{64}$$

The final set of explicit expressions are the expressions for the trend coefficients α_i which can be found by the off-diagonal equations:

$$\therefore \quad \alpha_0 \equiv 0, \ \alpha_1 = \frac{C_{1,2}}{C_{0,2}}, \ \alpha_2 = \frac{C_{1,2}}{C_{0,1}} \tag{65}$$

To conclude and recap this theory, the triple-collocation method will provide an algorithm to obtain the absolute error variances σ_i^2, the linear intercalibrated trend coefficients α_i and bias coefficients β_i for three independent and uncorrelated collocated observing system. With this method, it is possible to estimate the observation error of the L2B HLOS wind observations and verify the $(O - B)$ statistics.

6.4.2 Results with triple collocation method

Together with the argument that Mode-S EHS is used as the primary reference —previous validation results demonstrated the bias of Mode-S EHS to be in the order of 0.023 ms^{-1} when compared to the ECMWF IFS [Sec. 6.3.1]. Mode-S EHS is therefore set as the reference system x_0, while $\alpha_{1,2}$ and $\beta_{1,2}$ are reserved for the L2B and ECMWF IFS collocated data set. The order is not important.

The intercalibration coefficients retrieved with the triple collocation method for the Mie and Rayleigh channel as a function of the geometric height Z_{geom} are illustrated in Fig. 43 and Fig. 44 respectively. The trend coefficients α_i for the Mode-S EHS data as reference system are by definition $\alpha_0 \equiv 1$ and $\beta_0 \equiv 0$. The trend coefficients displays the scaling of the data w.r.t to the reference, while the bias coefficients provide information on the mean difference w.r.t. to the reference.

- **Mie trend coefficients [upper panel of Fig. 43]:** between $\sim 0.0 \leq Z_{geom} \leq 4.5$ [km] the coefficients for L2B and ECMWF IFS initially underestimates and later overestimates the reference —that is Mode-S EHS with $\alpha \equiv 1$. For $\sim Z_{geom} \geq 4.5$ [km], both trend coefficient lines settle to values of 1.001 and 0.976 for L2B and ECMWF IFS respectively. This indicates that both collocated data sets demonstrate a strong linear relationship w.r.t Mode-S EHS.
- **Mie bias coefficients [lower panel of Fig. 43]:** the bias coefficients for ECMWF IFS approximates the reference very accurate with a mean bias of 0.0881 ms^{-1} —indicating the ECMWF IFS model to be nearly unbiased when assuming the Mode-S

to be the truth. The systematic bias in L2B is also proven by the results of the triple collocation method —providing a mean bias value of 1.839 ms^{-1}. This is in accordance with previous validation results. Moreover, the turquoise dash-dot line represents the $(O_2 - O_1)$ statistics line —i.e. when L2B is compared with Mode-S EHS explicitly. The triple collocated L2B bias line approximates this $(O_2 - O_1)$-line very accurately —confirming the $(O_2 - O_1)$ statistics results. The spike near $Z_{geom} \sim 3.5$ [km] might be the affect of the occurrence of hot-pixels. This needs further research.

Similar triple collocation results are found when performing the same analysis for the Rayleigh channel [Fig. 44]. Following the same methodology:

- **Rayleigh trend coefficients [upper panel of Fig. 44]:** the trend coefficient line settles for $\sim Z_{geom} \geq 4.5$ [km] with values of 1.005 and 0.991 for L2B and ECMWF IFS respectively —indicating once again a very strong linear relationship w.r.t. Mode-S EHS.
- **Rayleigh bias coefficients [lower panel of Fig. 44]:** also in the Rayleigh channel —ECMWF IFS approximates the Mode-S EHS reference very accurately with an average bias in the order of 1.685 ms^{-1}. The systematic bias is confirmed by the triple collocation results —demonstrating a mean bias of about 1.685 ms^{-1}. The triple collocated L2B bias line seems to underestimate the $(O_2 - O_1)$-line as it is beneath the turquoise line.

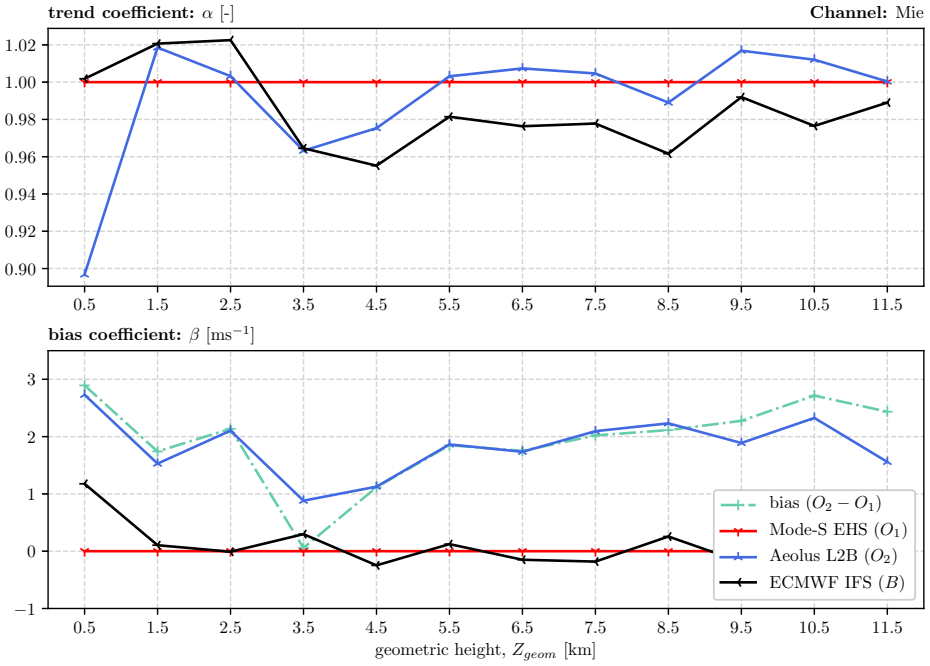

Figure 43: Triple collocation derived intercalibration coefficients results for (upper) the trend (α_i), and (lower) the bias (β_i, ms^{-1}) for the Mie channel. Mode-S EHS (red) is set as the 'truth' reference system, such that $x_i := x_0$ with $\alpha_0 \equiv 1$ [-] and $\beta_0 \equiv 0$ [ms^{-1}].

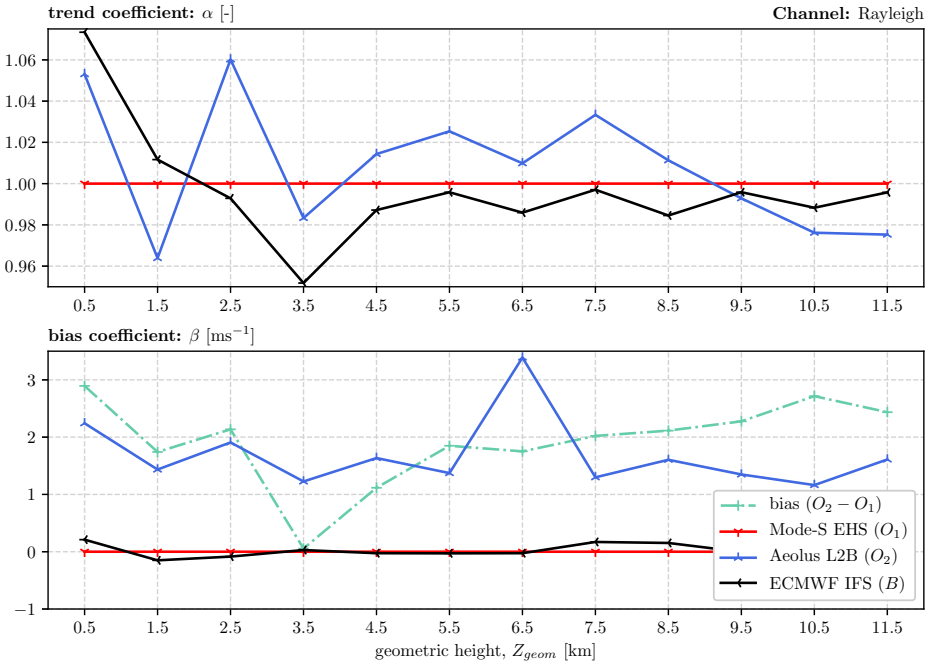

Figure 44: Triple collocation derived intercalibration coefficients results for (upper) the trend (α_i), and (lower) the bias (β_i, ms^{-1}) for the Rayleigh channel. Mode-S EHS (red) is set as the 'truth' reference system, such that $x_i := x_0$ with $\alpha_0 \equiv 1$ [-] and $\beta_0 \equiv 0$ [ms^{-1}].

After discussing the linear intercalibration coefficients α_i, β_i —recall that by applying the triple collocation method [Stoffelen, 1998; Stoffelen and Vogelzang, 2012] the three absolute error variances [Eq. 64] for the three corresponding data sets can be obtained as well [Fig. 45, 46].

- **Mie absolute error variance:** the vertical profile of the triple collocated derived absolute error variances σ_i^2 for L2B (O_2) is shifted to the right w.r.t the error variances as reported in the L2B BUFR product [middle panel of Fig. 45]. This might reveal an underestimation of the estimated HLOS wind observation error —as obtained with the triple collocation method —in the L2B BUFR product. The absolute error variance for Mode-S EHS (O_1) is on average of the order of ~ 1.5 ms^{-1} for $\sim Z_{geom} \geq 3.5$ [km], which is unexpected given that the error estimate of averaged Mode-S EHS data is significantly smaller than the value of 1.5 ms^{-1} when applying the *Square Root n Law* [Eq. 50] as reported in de Haan [2016].
- **Rayleigh absolute error variance:** an underestimation of the estimated HLOS wind observation error in the L2B BUFR product is also noted in the Rayleigh channel [middle panel of Fig. 46]. In contrast to the Mie channel —the error variance for (O_1) is on average of the order of ~ 2.3 ms^{-1} for $0.0 \leq Z_{geom} \leq 12.0$ [km]. This value is significantly higher than the aforementioned error variance for the Mie channel. This requires further research. Nevertheless, the absolute error variance for (B) is of the same order as for the Mie channel —demonstrating on average a value of approximately 1.5 ms^{-1} along the vertical profile.

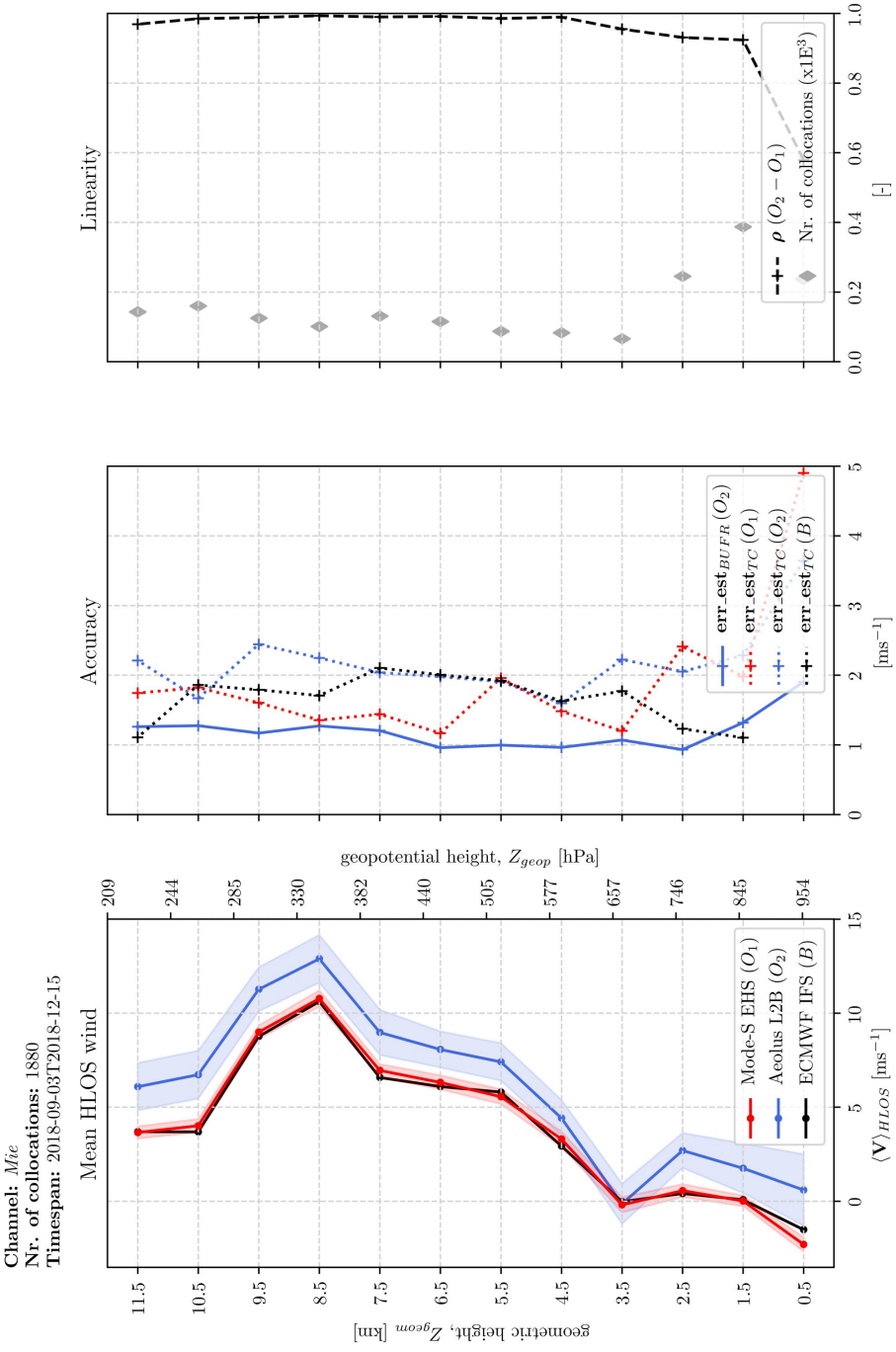

Figure 45: Same vertical profile plots for the Mie channel as Fig. 37, except for the middle figure which demonstrates vertical profiles of triple collocated derived error estimates σ_i^2 [Eq. 64] for the collocated ECMWF IFS data set (black), Mode-S EHS (red) and L2B (blue). Note that the absolute error variance is abbreviated as *'err_est'* and that no distinction is made between the orbit phase. The subscript $()_{BUFR}$ in the center panel refers to the error estimate as provided by the BUFR file, while the subscript $()_{TC}$ refers to the triple collocated method result.

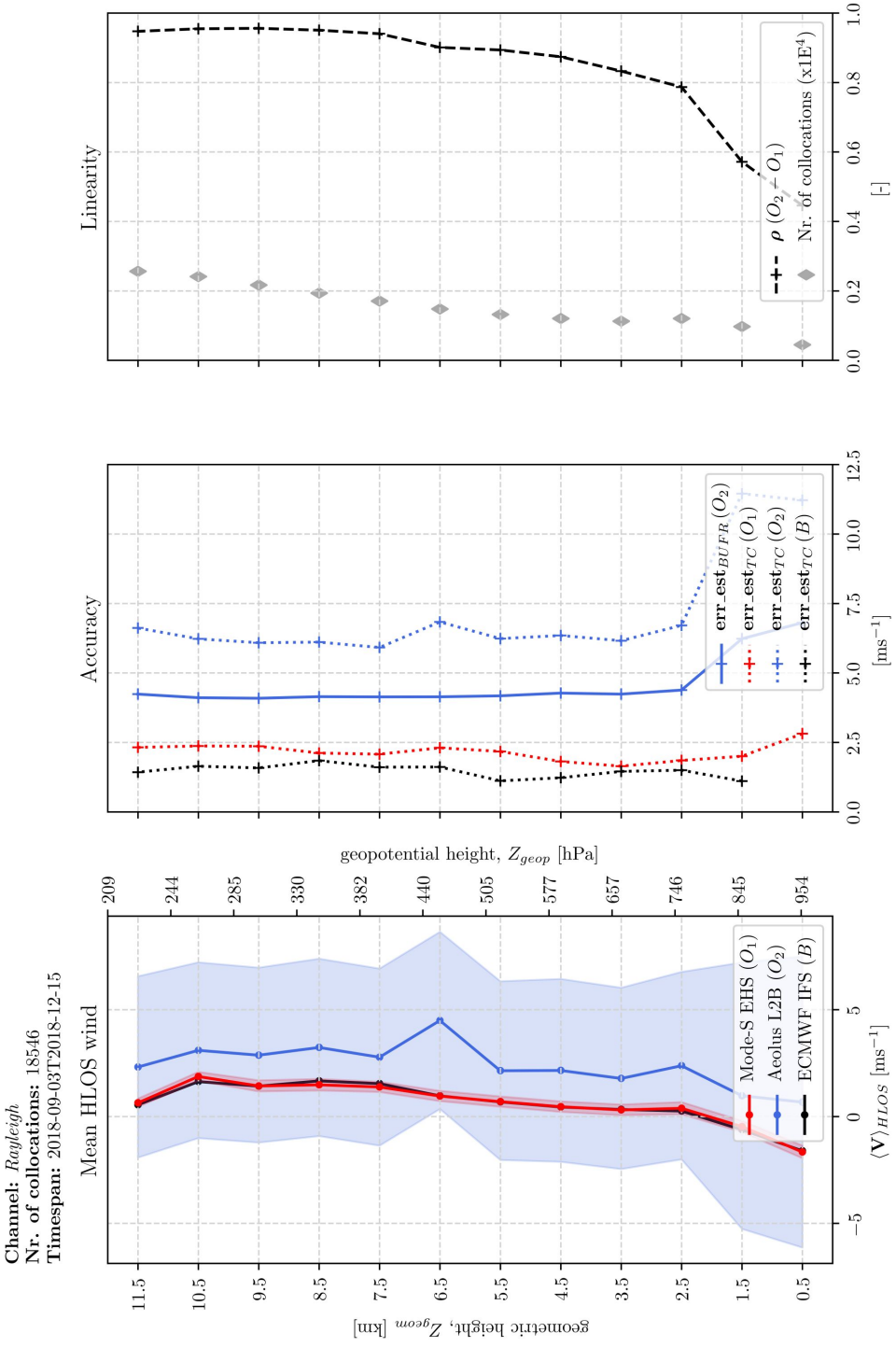

Figure 46: Same vertical profile plots for the Rayleigh channel as Fig. 38, except for the middle figure which demonstrates vertical profiles of triple collocated derived error estimates σ_i^2 [Eq. 64] for the collocated ECMWF IFS data set (black), Mode-S EHS (red) and L2B (blue). Note that the absolute error variance is abbreviated as *'err_ est'* and that no distinction is made between the orbit phase. The subscript $()_{BUFR}$ in the center panel refers to the error estimate as provided by the BUFR file, while the subscript $()_{TC}$ refers to the triple collocated method result.

7 Discussion

After discussing the validation results, this section will shortly discuss the discrepancies and provide some notes regarding the performed validation methodology and the corresponding results.

- the quantity and quality of the L2B wind observations depends upon various factors —e.g. air density for the Rayleigh-Brillouin backscattering and the optical depth of aerosols and clouds for the Mie backscattering. This significantly influences the quantity and quality of collocations as well.

- Before collocating —the L2B data has been preprocessed with predefined quality control flags. Mie HLOS wind observations with an error estimate of ≥ 3.0 [ms^{-1}], Rayleigh HLOS wind observations with an error estimate of ≥ 8.0 [ms^{-1}] and HLOS wind observations flagged as `INVALID` are removed from the data set. This influences the quantity and quality of the validation results. It is important that other CAL/VAL researches use the same quality control flags for valid intercomparison of validation results.

- Albeit the vertical wind component of the full LOS wind vector is neglected, this assumption may not always be valid when $3 \leq L_{int} \leq 7$ km —i.e. when the integration length is not $\gg$ the vertical averaging length [see Sec. 3.2.5]. No additional quality control flag in the preprocessing algorithm is introduced which verifies this statement. However, the *probability density function* plot of L_{int} [Fig. 8] demonstrated no statistical significance for the case in which $3 \leq L_{int} \leq 7$ km.

- A first-order estimate has been applied to increase the accuracy in the collocation algorithm by utilizing the inverse distance weighting spatial interpolation. This interpolation technique is suitable for point observations. Albeit L2B observations are reported as a single geolocated observation —i.e. a point observation —the wind retrieval of this observation is based on N accumulated measurements along a certain integration length L_{int} —i.e. the sampling length. For this reason, it can be argued whether the inverse distance weighting spatial interpolation technique is applicable in such a case. However, the L2B BUFR product reports the `start`, `end` and `center of gravity` position of each observation along L_{int}. For this validation research, the `center of gravity` position is taken and therefore each observation basically becomes still a point measurement —despite that the observation is based on a certain L_{int}.

- the timespan in which collocations have been performed runs from 2018/09/03 to 2018/12/16, which is statistically significant to perform validation research. However, in the mean time the L2B data has been affected by e.g. the appearance of hot-pixels in the ACCD, decreasing energy level in the UV laser of ALADIN, executed tunings or calibrations by ESA and a varying bias over time. This makes it difficult to interpret the validation results when e.g. meteorological or other physical arguments are assumed to be not the cause.

- It is arguable whether the method of Taylor-diagram was the best choice in determining the collocation parameters for the collocation box since —according to Taylor [2001] —the method requires a fixed reference with a fixed value for σ_{ref}. Due to

the applied *Square Root n Law* in the collocation algorithm as a first order approximate, a fixed reference cannot be achieved and utilizing the Taylor-diagram became limited for this validation study. In order to utilize the advantages of constructing Taylor-diagrams, it is decided to fix the reference nevertheless [see Sec. 6.2.3]. This decision required a relaxation to determine the values for the CRMSD. Nevertheless, the markers in the Taylor-diagram w.r.t the Pearson's correlation coefficient ρ and the standard deviation σ_{obs} of L2B remained positioned correctly and the constructed Taylor-diagram became still a powerful tool to determine the parameters for the collocation box.

One single Mode-S EHS observation point is not representative for one single L2B HLOS wind observation since the latter is based on a certain integration length L_{int} [Sec. 3.2.3]. It is therefore arguable whether the *Square Root n Law* as a first order approximate for σ_{ref} [Eq. 50] is accurate enough to decrease the representativeness errors for Mode-S EHS observations within the collocation box with this method. It can be postulated that a mathematical formulation of a structure function of the velocity field in turbulent flows in the collocation box is required to obtain a statistical description of the developed turbulent flow and hence how the Mode-S EHS wind component error estimate of —according to de Haan [2016] —1.4 ± 0.1 ms^{-1} for each single Mode-S EHS observation point scales. Further research is required.

To conclude —albeit it is recommended to assign different collocation box parameters to Mie and Rayleigh observations, it is not recommended to use the Taylor-diagram for the aforementioned reasons.

- According to Stoffelen and Vogelzang [2012], the triple collocation method has only been used a few times. Next to the argument that three collocated data sets are required which in practise is usually hard to establish —the method is considered to be too difficult for practical applications by scientific community. This statement can be underlined after performing this method with L2B, Mode-S and ECMWF IFS. The interpretation —and thus practical application —is challenging and requires additional research.

As mentioned before, the quantity and quality of the L2B wind observations depends upon various factors. To elaborate more on this subject, the Aeolus wind observations include errors of several sources, e.g.

- **Instrument errors:** misalignment of ALADIN, imperfections in the Fabry-Pérot and Fizeau interferometer for the Rayleigh and Mie channel respectively, the degradation in the energy level of the laser of ALADIN, or e.g. the occurrence of hot-pixel in the ACCD.
- **Orbit related errors:** thermal variability due to the dawn-dusk orbit resulting into harmonic biases —harmonic biases due to *Delta-v* manoeuvres to correct for the degradation of the orbit altitude or for orbit drifting.
- **Processing errors**: processing errors in the Level 0 and Level 1A data [Tab. 2] in e.g the calibration of the *attitude and orbit control system* of the satellite, calibration and signal processing errors, or quality control.

- **Level 2B processing errors** e.g. processing errors due to e.g. calibration, signal processing or quality control.

Without loss of generality, these sources will bias the retrieved wind observations and thus the validation research.

8 Conclusion

In this research —performed in collaboration with the Royal Dutch Meteorological Institute and the Institute for Marine and Atmospheric research Utrecht from Utrecht University —geolocated *L2B (baseline 2B02)* wind observations retrieved with the novel Earth observation satellite *Aeolus* of the European Space Agency —have been validated with meteorological representative aircraft-derived data, together with Numerical Weather Prediction (NWP) model data from the European Centre for Medium-Range Weather Forecasts (ECMWF) Integrated Forecast System (IFS). These aircraft-derived data are independent mode-selective (Mode-S) enhanced surveillance (EHS) aircraft-derived data at high spatial and temporal resolution —referred to as *Mode-S EHS* data. The main conclusions of this validation research will be elaborated by recalling the main research question [Sec. 1.2]:

What is the quality of the wind observations as measured by ESA its novel Earth observation satellite Aeolus when compared with Mode-S EHS aircraft-derived wind observations?

- Mode-S EHS data is a quality controlled proven meteorological representative data set at high resolution. Studies demonstrated the quality and quantity of these aircraft-derived data in comparison to global NWP forecast results from the ECMWF IFS and illustrated that the data set is nearly unbiased [see e.g. de Haan, 2014] —after applying necessary corrections as discussed by [de Haan, 2013]. This statement can be underlined when performing $(O_1 - B)$ statistics in which O_1 is the *observed* Mode-S EHS collocated data set and B is the *background* ECMWF IFS collocated data set, used for Aeolus data processing —demonstrating $(O_1 - B) = 0.023$ ms^{-1}. This value is nearly zero —further confirming that the Mode-S EHS data set is indeed nearly unbiased when compared to ECMWF IFS data. This statement reinforced the value of using Mode-S EHS data as reference to validate with L2B data.

- When performing $(O - B)$ statistics with the *observed* L2B collocated data set (O_2) —the statistics demonstrate a mean $(O_2 - B) = 2.061$ ms^{-1} for the Mie channel and for the Rayleigh a mean $(O_2 - B) = 1.743$ ms^{-1}. These values are mean values over the 3.5 months validation period —2018/09/03 till 2018/12/15. This indicates that collocations performed in the Mie channel are higher biased in comparison to the collocation wind observations as measured in the Rayleigh channel. These results are in agreement with other Aeolus CAL/VAL teams, such as Geiß [2019].

- When performing performing $(O_2 - O_1)$ statistics —i.e. comparing L2B with Mode-S EHS —similar validation results for the bias can be demonstrated. For the Mie channel —a numerical value of 2.066 ms^{-1} is found while a value of 1.669 ms^{-1} is found for the Rayleigh channel. Whether L2B is compared to ECMWF IFS or Mode-S EHS, both show similar validation results and therefore consistency.

- In continuation to the bias analysis —$(O_2 - O_1)$ validation results demonstrates that the bias is systematically significantly higher in the descending orbit when compared to the ascending orbit. This statement holds for both channels. Validation results demonstrate the bias to be 1.789 ms^{-1} during the ascending orbit, while a significant higher value of 2.404 ms^{-1} is found during the descending orbit. The same applies for the Rayleigh channel —depicting values of 1.383 ms^{-1} and 2.069 ms^{-1} respectively.

- Using the triple collocation method —when Mode-S EHS is set as the reference —the trend coefficients for the Mie and Rayleigh channels both demonstrates —on average —a very strong linear relationship with respect to Mode-S EHS with values of 1.001 and 1.005 for the Mie and Rayleigh channel respectively. For the bias coefficients —the triple collocated results confirms the aforementioned systematic bias in the Mie and Rayleigh channel with values of 1.839 ms^{-1} and 1.685 ms^{-1} respectively. For the absolute error variance for both channels —the triple collocated derived absolute error variances for L2B is shifted to the right w.r.t the error variances as reported in the L2B BUFR product. This might reveal an underestimation of the estimated HLOS wind observation error in the L2B BUFR product. Further research is required.

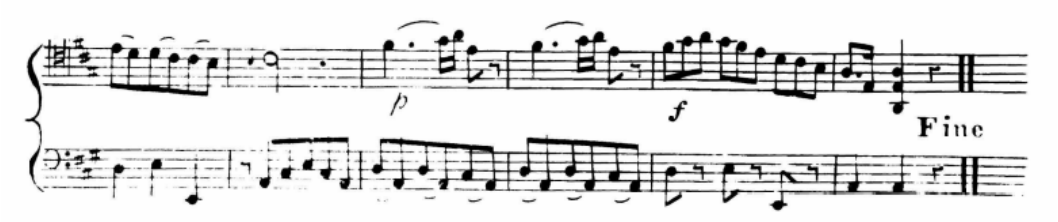

9 Epilogue

It is convenient to remind the reader that Aeolus is a unique Earth observation mission. For the first time it is possible to measure winds from space using the lidar technology based on the Doppler principle. Working with raw data from such a novel mission is —how ironic —a *turbulent* process. Despite comprehensive and intensive preparations before launch[82], one can expect peculiar features showing up in the real data. Aeolus is no exception and so this happened.

The Aeolus wind data used in this research study should be considered as processed, but remains raw data nevertheless. The retrieved wind observations are not yet well-calibrated —show drifting biases over time in both the Mie and Rayleigh channel and sudden much enhanced biases due to hot-pixels emerging on the ACCD receiver at random time instants.

According to dr.ir. G.J. Marseille — *"The tools developed during this internship are very valuable for characterizing the errors in the measured winds. Good error characterization is of crucial importance for optimal use of the wind observations in NWP through data assimilation. Scatter density plots against a well-calibrated observing system (or NWP model) as presented in section 6.3.2 immediate show potential issues, such as biases, for instance as a function of wind speed or orbit phase (descending versus ascending)".*

The triple collocation method is a well established technique for estimating error characteristics for systems with stable error characteristics over time, e.g. Mode-S EHS and NWP models. The latter systems were used in this study in addition to Aeolus winds as a third system. As mentioned earlier, error characteristics for Aeolus winds are not stable at all at this stage of the mission. The triple collocation method has not been developed to estimate error characteristics which change over time nor when the quality of the observations are dependent on e.g. aerosol and cloud density or an accumulation length to scale from measurement to observation level. Application of the triple collocation method provides first indications of the error characteristics of Aeolus, Mode-S EHS and ECMWF IFS nevertheless, but does not provide the complete answer.

A first reprocessing of the first 10 months of Aeolus data is foreseen in the autumn of 2019. This includes correction for hot-pixels and much improved calibration —expected to result into wind retrievals with minimal biases and of sufficient quality when being assimi-

[82]The mission was initially approved in 1999 for a launch in 2007 but postponed to August 22^{th} of 2018 due to technical issues.

lated in a NWP model.

As already mentioned in the acknowledgement —I am dr.ir. G.J. Marseille, dr.ir. A. Stoffelen and dr. J. de Kloe very grateful for involving me in the calibration and validation team of ESA and industry on a very serious and professional way. Additionally, I highly appreciate that dr.ir. G.J. Marseille, dr.ir. A. Stoffelen and dr. J. de Kloe involved my validation results by discussing them among other scientists such as during the *Calibration and Validation Workshop - March 2019* at ESRIN in Rome (Italy), *ESA Living Planet Symposium - May 2019* in Milan (Italy) or during a telepresentation at the *Lidar Working Group*. It was definitely an honor to work on such an extraordinary fascinating, important and novel Earth observation satellite of ESA: the *Atmospheric Dynamics Mission - Aeolus*.

References

M.L. Chanin, A. Garnier, A. Hauchecorne, and J. Porteneuve. A Doppler lidar for measuring winds in the middle atmosphere. *Geophys. Res. Lett.*, **16**(11):pp.1273–1276, 1989. doi: 10.1029/GL016i011p01273.

P. Courtier, P. Gauthier, and F. Rabier. Study of preparation for the use of Doppler wind lidar information in meteorological assimilation systems. *Q.J.R. Meteorol. Soc*, **132**(619): pp.1927–1947, 2006. doi: 10.1256/qj.05.83.

B. Cushman-Roisin and J.-M Beckers. *Introduction to geophysical fluid dynamics.*, volume 101 of *International Geophysics Series*. Elsevier Science Publishing Co. Inc., second edition, 2011.

A. Dabas, M-L. Denneulin, P. Flamant, C. Loth, A. Garnier, and A. Dolfi-Bouteyre. Correcting winds measured with a Rayleigh Doppler lidar from pressure and temperature effects. *Tellus A*, **60**(2):pp.206–215, 2008. doi: 10.1111/j.1600-0870.2007.00284.x.

S. de Haan. High-resolution wind and temperature observations from aircraft tracked by Mode-S air traffic control radar. *Journal of Geophysical Research*, **116**(D10), 2011. doi: 10.1029/2010JD015264.

S. de Haan. An improved correction method for high quality wind and temperature observations derived from Mode-S EHS. *KNMI Technical Report TR-338*, pages pp.1–80, 2013.

S. de Haan. Availability and quality of Mode-S MRAR (BDS4.4) in the MUAC area - A first study. *KNMI, Intern rapport (IR 2014-01)*, pages pp.1–24, 2014.

S. de Haan. Estimates of Mode-S EHS aircraft-derived wind observation errors using triple collocation. *Atmos. Meas. Tech.*, **9**(8):pp.4141–4150, 2016. doi: 10.5194/amt-9-4141-2016.

S. de Haan and S. Stoffelen. Assimilation of high-resolution Mode-S wind and temperature observations in a regional NWP model for nowcasting applications. *Weather and Forecasting*, **27**(4):pp.918–937, 2012. doi: 10.1175/WAF-D-11-00088.1.

P. de Jong, S. Haan, J. Sondij, M. Koutek, A. Hoekstra, and J. Bokhorst. Operational use of aircraft-derived data for meteorology and other applications. *Conferance WMO CIMO Technical Conference on Meteorological and Environmental Instruments and Methods of Observation, Amsterdam*, 2018.

N. Diodato and M. Ceccarelli. Interpolation processes using multivariate geostatistics for mapping of climatological precipitation mean in the Sannio Mountains (southern Italy). *Earth Surface Processes and Landforms*, **30**(3):pp.259–268, 2005. doi: 10.1002/esp.1126.

European Space Agency (ESA). *The Changing Earth.*, volume European Space Agency SP-1304 of *European Space Agency Publications Division*. Elsevier Science Publishing Co Inc, fifth edition, 2006.

European Space Agency (ESA). *ADM-Aeolus Mission Requirements Document.*, volume AE-RP-ESA-SY-001. Mission Science Division, 2016.

A. Garnier and M.L. Chanin. Description of a Doppler Rayleigh LIDAR for measuring winds in the middle atmosphere. *Appl. Phys. B*, **55**(1):pp.35–40, 1992. doi: 10.1007/BF00348610.

A. Geiß. Methodology and case studies for the validation of Aeolus observations by means of radar wind profilers. 2019.

R.J. Graham, S.R. Anderson, and M.J. Bader. The relative utility of current observation system to global-scale NWP forecasts. *Quart. J. Roy. Meteor. Soc.*, **126**(568):pp.2435–2460, 2006. doi: 10.1002/qj.49712656805.

J.R. Holton. *An introduction to dynamic meteorology.*, volume 88 of *International Geophysics Series*. Elsevier Science Publishing Co. Inc., fifth edition, 2012.

A. Horanyi, M. Cardinali, C. Rennie, and L. Isaksen. The assimilation of horizontal line-of-sight wind information into the ECMWF data assimilation forecasting system. Part I: The assessment of wind impact. *Q.J.R. Meteorol. Soc*, **141**(689):pp.1233–1243, 2006. doi: 10.1002/qj.2551.

A. Horanyi, L. Isaksen, M. Renni, S. Abdalla, and D. Tan. Impact of Aeolus Continuous Mode Operation on Numerical Weather Prediction. *European Space Agency Report AE-TNECMWF-Impact-Study-005*, 2013.

H. Langland and N. Maue. Uncertainty in operational atmospheric analysis (presentation slides). *Fifth WMO Workshop on Observing System Impact in NWP, May 2012, Sedona, Arizona*, 2012.

A.C. Lorenc, R.J. Graham, MacPherson B. Dharssi, I., N.B. Ingleby, and R.W. Lunnon. Preparation for the use of Doppler wind lidar information in meteorological assimilation systems. *European Space Agency Contract Rep.*, (3454), 1992.

O. Lux, C. Lemmerz, F. Weiler, U. Marksteiner, B. Witschas, S. Rahm, A. Schäfler, and O. Reitebuch. Airborne wind lidar observations over the North Atlantic in 2016. *Atmospheric Measurement Techniques*, **11**(6):pp.3297–3322, 2018. doi: 10.5194/amt-11-3297-2018.

G.-J. Marseille and A. Stoffelen. Simulation of wind profiles from a space-borne Doppler wind lidar. *Q.J.R. Meteorol. Soc*, **129**(594):pp.3079–3098, 2003. doi: 10.1256/qj.02.96.

G.-J. Marseille, A. Stoffelen, F. Bouttier, D. Vasiljevic, S. de Haan, and S. Cardinali. ADM-Aeolus Doppler wind lidar Observing System Simulation Experiment. *Q.J.R. Meteorol. Soc*, **132**(619):pp.1927–1947, 2006. doi: 10.1256/qj.05.83.

G.-J. Marseille, A. Stoffelen, H. Schyberg, H. Körnich, and L. Megner. VHAMP - Vertical and Horizontal Aeolus Measurement Positioning - Executive summary. *European Space Agency Report AE-ES-VHAMP_v1.0*, pages pp.1–26, 2013.

J.A. McKay. Assessment of a multibeam Fizeau wedge interferometer for Doppler wind lidar. *Appl. Opt.*, **41**(9):pp.1760–1767, 2002. doi: 10.1364/AO.41.001760.

D. Shepard. A two-dimensional interpolation function for irregularly spaced data. *ACM* , pages pp.517—524, 1968. doi: 10.1145/800186.810616.

A. Stoffelen. Toward the true near-surface wind speed: error modeling and calibration using triple collocation. *Journal of Geophysical Research*, **103**(C4):pp.7755–7766, 1998. doi: 10.1029/97JC03180.

A. Stoffelen and J. Vogelzang. Triple collocation. *EUMETSAT Document NWPSAF-KN-TR-021*, pages pp.1–24, 2012.

A. Stoffelen, J. Pailleux, E. Källén, J.M Vaughan, L. Isaksen, P. Flamant, W. Wergen, E. Andersson, H. Schyberg, A. Culoma, R. Meynart, M. Endemann, and P. Ingmann. The Atmospheric Dynamics Mission for global wind field measurement. *Bulletin of the American Meteorological Society*, **86**(1):pp.73–87, 2005. doi: 10.1175/BAMS-86-1-73.

D. Tan, E. Andersson, A. Dabas, P. Poli, A. Stoffelen, J. de Kloe, and D. Huber. ADM-Aeolus Level-2B/2C Processor - Input/Output Data Definitions Interface Control Document. 2009, ECMWF, METEO-FRANCE, KNMI and DLR, AE-IF-ECMWF-L2BP-001.

D.G.H. Tan, E. Andersson, J. de Kloe, G.-J. Marseille, A. Stoffelen, P. Poli, M-L. Denneulin, A. Dabas, D. Huber, O. Reitebuch, P. Flamant, O. Le Rille, and H. Nett. The ADM-Aeolus wind retrieval algorithms. *Tellus A*, **60**(2):pp.191–205, 2007. doi: 10.1111/j.1600-0870.2007.00285.x.

K.E. Taylor. Summarizing multiple aspects of model performance in a single diagram. *Journal of Geophysical Research*, **106**(D7):pp.7183–7192, 2001. doi: 10.1029/2000JD900719.

A.J. van Delden. *Atmospheric Dynamics (lecture notes)*. September 4^{th} 2017 edition, 2017. Available at `http://www.staff.science.uu.nl/~delde102/AtmosphericDynamics.html`.

J.M. Wallace and P.V. Hobbs. *Atmospheric science.*, volume 92 of *International Geophysics Series*. Elsevier Science Publishing Co. Inc., second edition, 2006.

H. Wernli, S. Dirren, M.A. Liniger, and M. Zillig. Dynamical aspects of the life cycle of the winter storm 'Lothar' (24-26 December 1999). *Quart. J. Roy. Meteor. Soc.*, 128: pp.405–429, 2002. doi: 10.1256/003590002321042036.

World Meteorological Organization (WMO). *Guide to the Global Observing System.*, volume 488 of *European Space Agency Publications Division*. WMO, 2010 edition, 2013.